Photoexcitation at Titania Surfaces

Daniel Thomas Payne

Thesis submitted for the Degree of Doctor of Philosophy
of the University College London.

Supervised by
Prof. Geoff Thornton

2017

I, Daniel Thomas Payne, confirm that the work presented in this thesis is my own. Where information has been derived from other sources, I confirm that this has been indicated in the thesis.

Abstract

This thesis employs energy- & time-resolved photoemission spectroscopy to examine two surfaces of titanium dioxide (TiO_2) single crystals. Both surfaces investigated, the rutile TiO_2(110) and anatase TiO_2(101) surfaces, are pertinent to future energy research.

Resonant two-photon photoexcitation at the reduced rutile TiO_2(110) surface is found to involve the Ti 3d band gap states and energy levels of t_{2g} or e_g symmetry in the conduction band. The unoccupied state is determined to be centred $\sim$2.7 eV above the Fermi level (E_F), with a lifetime of less than 15 fs. Adsorption of bridging hydroxyls (OH_b) is shown to enhance the intensity of the observed resonance. The signal intensity reaches a maximum under a monolayer of water, which is attributed to partial dissociation of adsorbed water.

Electron bombardment of the anatase TiO_2(101) surface is shown to increase the reduction state of the surface in ultra-violet photoemission spectra, which is attributed to the formation of oxygen vacancies. However, these point defects are known to migrate towards the bulk at temperatures above 200 K, restoring a thermally-equilibrated concentration. Bombardment also results in the appearance of new features in the valence band spectral region, which we associate with the 3σ and 1π molecular orbitals of OH_b. Since excess electrons mediate redox reactions at the surface, their greater concentration may increase the potential for these processes to occur at the hydroxylated surface.

Finally, a femtosecond-resolved, extreme ultra-violet photoemission study of the reduced rutile TiO_2(110) surface is presented. Under infra-red photoexcitation, an electron trapping time of $\sim$40 fs is obtained, which coincides with the period of the material's longitudinal phonon mode. Hence, interaction between electrons and this phonon mode is inferred to facilitate polaron formation. An additional, slow decay component, observed only under ultra-violet irradiation, is assigned

to electron-hole recombination on the pico- to nanosecond timescale. The unexpectedly slow recovery of the Ti 3d band gap states population is attributed to trap-assisted recombination processes.

“There are things known and there are things unknown, and in between are the doors of perception.”

Aldous Huxley

Acknowledgements

I wish to express my gratitude for the guidance and insight provided by my supervisor, Prof. Geoff Thornton. Furthermore, I wish to extend my thanks to all members of the Thornton Group. Notably, I would like to thank Dr. Chi Lun Pang and Dr. Yu Zhang for generously sharing their expertise and for their dedication to this project.

I am indebted to my co-supervisor, Prof. Helen Fielding, for her support, investment and encouragement. I also wish to thank Dr. Michael Parkes for the additional help he has provided.

I wish to thank Dr. Cephise Cacho, Dr. Emma Springate and Dr. Richard Chapman, who contributed to the results presented in Chapter 6. Their perseverance and dedication played a vital role in securing the success of this experiment.

I am grateful for the continued love and encouragement provided by my mother, Keri, whose support is unwavering in the face of academic jargon and obscurity. I wish to thank my father, Robin, for engaging my passion for science from a young age and my brother, Lewis, for his perspective-restoring scientific apathy. I dedicate this thesis to my family, in thanks for the support which made it possible.

Finally, I wish to thank the many friends who have made London my home for the past four years, who now know more about TiO_2 than they may have wished.

List of Publications

Non-band-gap photoexcitation of hydroxylated TiO_2

Y. Zhang, D. T. Payne, C. L. Pang, H. H. Fielding and G. Thornton

Journal of Physical Chemistry Letters, vol. 6, no. 17, pp. 3391-3395, 2015

Coverage-dependent two-photon photoexcitation at the H_2O/TiO_2 interface

D. T. Payne, Y. Zhang, C. L. Pang, H. H. Fielding and G. Thornton

Surface Science, vol. 652, pp. 189-194, 2016

Creating excess electrons at the anatase TiO_2(101) surface

D. T. Payne, Y. Zhang, C. L. Pang, H. H. Fielding and G. Thornton

Topics in Catalysis, vol. 2, no. 101, pp. 1-9, 2016

In Preparation:

Study of transient charge transfer on rutile TiO_2 by time-resolved valence band photoemission

Y. Zhang, D. T. Payne, C. L. Pang, C. Cacho, R. Chapman, E. Springate, H. H.

Glossary

1PPE	Single-photon Photoemission Spectroscopy
2PPE	Two-photon Photoemission Spectroscopy
AES	Auger Electron Spectroscopy
BGS	Band-gap States
CW	Continuous Wave
EELS	Electron Energy Loss Spectroscopy
eV	Electron Volt
FWHM	Full-width At Half Maximum
HB	Hydrogen Bond
IR	Infra-red
LCAO	Linear Combination Of Atomic Orbitals
LEED	Low-energy Electron Diffraction
LO	Longitudinal Optical
ML	Monolayer
MO	Molecular Orbital
OPA	Optical Parametric Amplifier
PES	Photoemission Spectroscopy
QMS	Quadrupole Mass Spectroscopy
RAL	Rutherford Appleton Laboratory
RFA	Retarding Field Analysis
SPV	Surface Photovoltage
TR-2PPE	Time-resolved Two-photon Photoemission Spectroscopy
UCL	University College London
UHV	Ultra-high Vacuum
UV	Ultra-violet
UPS	Ultra-violet Photoemission Spectroscopy
XPS	X-ray Photoemission Spectroscopy
XUV	Extreme Ultra-violet

Contents

List of Figures

Chapter 1

Introduction

1.1 Surface Science of Metal Oxides

Motivated by the wealth and diversity of surface-mediated physical and chemical processes, the discipline of surface science has elucidated mechanisms which underpin applications as diverse as catalysis, sensors and optics. Development in our understanding of such phenomena has been expediated by innovations in experimental techniques. The majority of surface studies are made under ultra-high vacuum (UHV) conditions, at pressures of 10^{-10} mbar or better, at ambient or cryogenic temperatures. These conditions permit a high level of experimental control and facilitate fundamental studies at the atomic level.

While such work has deepened our understanding of technologically relevant processes, the experimental conditions required are far removed from those in which these processes operate in industry. Indeed, the extent to which results obtained under UHV conditions may be extrapolated to higher pressures has been a topic of debate. The relative paucity of studies conducted at atmospheric pressures has given rise to the term '*pressure gap*'. Presently, increasing efforts are being made to realise controlled experimental studies under ambient conditions, facilitated by technical advances in photoemission and scanning-probe techniques [1, 2].

Applications arising from the study of surface science include anticorrosion and optical coatings, superconductors, chemical sensors, data-storage materials, elec-

tronic devices and solar cells [3]. Also of key importance is heterogeneous catalysis, including photocatalysis. In photocatalytic systems, the ground state electronic structure is perturbed by an incident photon and the catalytic process is mediated by excited charge carriers. Subsequently, there is great interest in the nature and dynamics of these excitation pathways. This information can be provided by ultra-fast spectroscopic techniques, which first pump and subsequently probe the system as it returns to equilibrium. Combining this information with that obtained from atomically-resolved scanning probe measurements has proven a powerful tool to reveal the mechanisms underlying catalytic processes.

Arguably the largest and most varied class of materials, metal oxides feature in many of the applications previously described. The study of metal oxide surfaces is motivated not only by economic considerations but also as a fundamental testing ground for our comprehension of crystal structures, phase-changes, magnetic and electronic behaviour and bonding [4].

1.2 Titanium Dioxide

Titanium dioxide (TiO_2), also known as titania, surfaces have received the most scientific attention of all metal oxide surfaces. Stoichiometric TiO_2 is an insulator, possessing a band gap of $\sim$3 eV [3], and consequently is transparent to visible light. Upon reduction, TiO_2 becomes an n-type semiconductor due to excess electrons in the crystal lattice and appears blue. Practically, it is required to reduce TiO_2 single crystal samples to induce sufficient conductance to allow scanning probe and photoemission studies to be conducted.

Of the two main TiO_2 polymorphs relevant to industry, rutile and anatase, the former has received the most scientific attention. Indeed, the rutile TiO_2(110) surface has arguably become the prototypical metal oxide surface due to its stability and availability. The appeal of a well characterised system has also attracted attention to this surface, which has been described as a self-promoting effect [3]. Regardless, anatase is believed to be the more catalytically active phase [5] and is therefore preferred in most industrial applications. The majority fraction of the catalytic interface comprises of the (101) crystal surface [6, 7]. Interestingly, both experimental and theoretical works suggest that the minority (001) surface may be more catalytically active [6, 8, 9]. However, the relative catalytic activity of

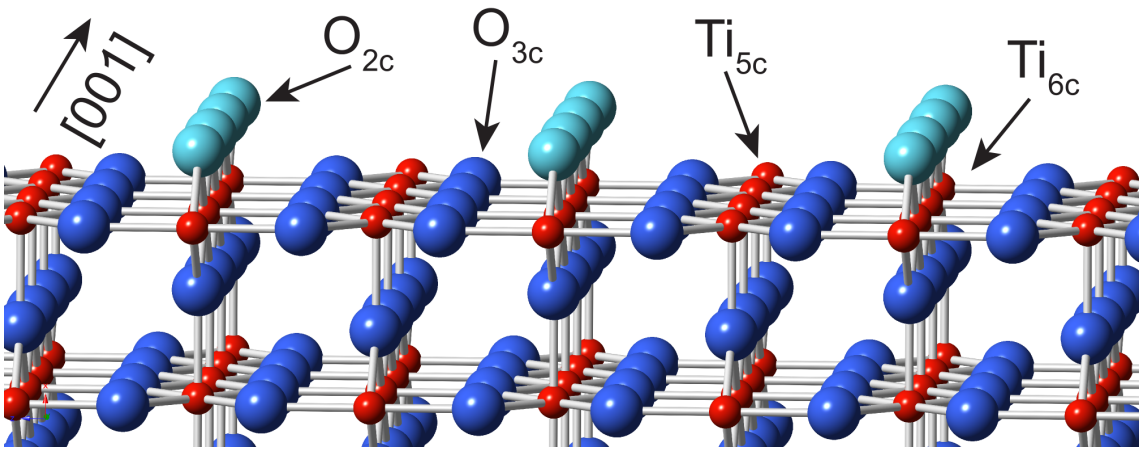

Figure 1.1: Ball and stick model of the rutile $TiO_2(110)(1\times1)$ surface. Five- and six-fold coordinated Ti atoms (Ti_{5c} & Ti_{6c}) are shown in red, three-fold coordinated O atoms in dark-blue and two-fold coordinated, bridging O atoms (O_{2c}) in light-blue.

anatase surfaces remains controversial [10].

Though stoichiometrically identical, the surfaces of anatase and rutile TiO_2 display distinctly different behaviours with respect to chemical reactions. This finding perfectly illustrates the strong and sometimes dominant role that morphology plays in surface chemistry. Also of interest is the differing behaviour of common defects, such as oxygen vacancies, within the crystal lattice. These point defects are coordinatively unsaturated and often function as adsorption sites for molecules, and therefore potentially as active sites for chemical reactions. Many chemical reactions at TiO_2 surfaces are believed to be mediated by excess charge carriers which may be created by chemical reduction or doping. As the catalytic activity of anatase and rutile TiO_2 is known to differ, it follows that the interaction of excess charge carriers with the crystal also changes with polymorph.

The Rutile (110) Surface

The rutile $TiO_2(110)(1\times1)$ surface is arguably the most intensively studied and well characterised metal oxide surface. According to Tasker's rules for the stability of ionic crystal surfaces, the (110) facet is the most stable rutile TiO_2 surface without the need for substantial reconstruction [11]. As the model in Figure 1.1 illustrates, the surface consists of alternating rows of two-fold coordinated, bridging oxygen atoms (O_{2c}) and troughs containing five-fold coordinated titanium atoms (Ti_{5c}), which run in the [001] crystallographic direction [12]. This structure has

been verified by long-range crystallography, scanning probe and photoemission measurements [13–16]. Standard UHV sample preparation techniques such as thermal annealing and ion bombardment may remove bridging O_{2c} atoms, resulting in a typical oxygen vacancy (O_b-vac) coverage of 0.05-0.10 monolayers (ML), where 1 ML is defined as the number of surface unit cells [12]. This reduced surface will be referred to as *r*-TiO_2(110).

Ti ions in the bulk of stoichiometric TiO_2 present a distorted, octahedral arrangement, which lifts the degeneracy of their *d*-orbitals. This splitting results in states with t_{2g}-like and e_g-like symmetry at the bottom and top of the conduction band, respectively [17]. Reduction of rutile TiO_2 induces further splitting due to a Jahn-Teller distortion, creating occupied band-gap states (BGS) of d_{xy} character, centred $\sim$1 eV below the Fermi level (E_F) [3, 18]. The excess electrons originating from these BGS are thought to enable many of the applications of TiO_2 described previously [19]. Scanning probe and photoemission studies have evidenced that O_b-vacs make the dominant contribution to the BGS intensity, with an additional contribution arising from Ti interstitial atoms [13].

Recently, density functional theory (DFT) calculations have indicated that O_b-vacs are shallow donors and do not create occupied BGS [20]. Instead, it is proposed that excess electrons from these donor centres localise as small polarons, in states 1 eV below E_F that are independent of the nature of the original donor defect. The degree of localisation exhibited by these polarons is an active area of research, owing partly to the dependency of electron localisation on the Hubbard correction, U, used in DFT+U calculations [21]. However, scanning probe measurements have shown that small polarons may localise at any Ti lattice site, in a phenomenon referred to as self-trapping, and hop easily between these sites at ambient temperatures [22].

Water Adsorption

Due to its presence in the majority of the applications of TiO_2, the interaction of water with the surfaces of this metal oxide is of great interest. To date, a major aim of single-crystal experiments has been to identify factors which cause water dissociation on the surface. This topic was reviewed extensively in 2002 [23], and has since been summarised [3, 12, 24]. Despite this considerable attention, consensus on the nature of adsorption at the rutile TiO_2(110) surface has not yet

been reached.

The majority of experimental studies evidence molecular adsorption of water on the stoichiometric TiO_2(110) surface [12]. However, dissociative adsorption is possible at surface defects. Water adsorbs dissociatively at O_b-vacs above 170 K, forming two bridging hydroxyls (OH_b) per O_b-vac [12]. The resulting surface, which will be referred to as *h*-TiO_2(110), is still reduced and exhibits BGS [13]. *h*-TiO_2(110) is stable up to about 500 K, above which OH_b recombine and desorb as water. Hence, the desorption of OH_b regenerates O_b-vacs at the surface [12, 25]. Additionally, it has been shown that oxygen vacancies at step edges are also active sites for water dissociation at the TiO_2(110) surface [26].

Temperature-programmed desorption (TPD) measurements display peaks assigned to molecularly adsorbed monolayer, bilayer and multilayer water at 270 K, 175 K and 155 K, respectively [27]. Monolayer water chemisorbs at Ti_{5c} sites, followed by physisorption of bilayer water on top of the O_{2c} rows. Bilayer water forms hydrogen bonds with molecules in the monolayer and in doing so slightly modifies its structure [28].

Although high-resolution electron energy loss measurements support the assignment of a molecular monolayer of water on *r*-TiO_2(110) [27], there is increasing support for a mixed monolayer of water and hydroxyls [29–33]. Water dissociation on the defect-free TiO_2(110) surface has been evidenced by photoemission measurements, where one bridging and terminal hydroxyl (OH_t) pair is created per water molecule. On *r*-TiO_2(110), one dissociation event at an O_b-vac substitutes one in a defect-free region of the surface, such that the total hydroxyl coverage of the mixed monolayer remains the same. The competitive nature of these two dissociation channels leads to a maximum hydroxyl coverage of 0.4 ML, for initial O_b-vac densities of $\leq$0.2 ML [31].

The Anatase (101) Surface

Anatase is a metastable polymorph of TiO_2, converting to the more thermodynamically desirable rutile phase at temperatures around 1000 K for relatively large single crystal samples [34]. Conversely, anatase is more stable than rutile for TiO_2 nanoparticles with diameters $<$10 nm [6], making it of interest to industry where TiO_2 powders are typically employed. Studies of anatase surfaces are consid-

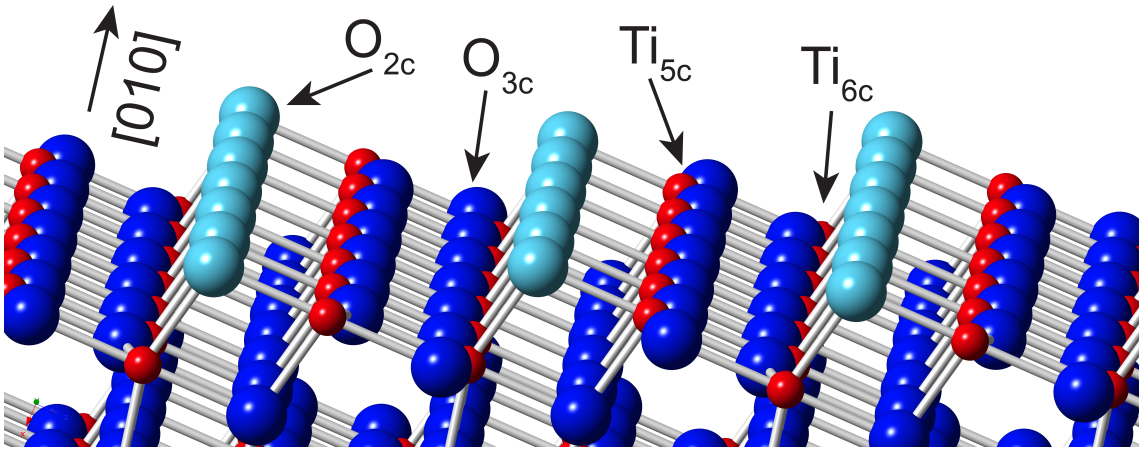

Figure 1.2: Ball and stick model of the anatase $TiO_2(101)(1\times1)$ surface. Five- and six-fold coordinated Ti atoms (Ti_{5c} & Ti_{6c}) are shown in red, three- and four-fold coordinated O atoms in dark-blue and two-fold coordinated, bridging O atoms (O_{2c}) in light-blue.

erably less numerous than those of rutile. The relative paucity of experimental work on anatase surfaces can be attributed to both the difficulty in creating suitably large, high quality artificial crystals and the low availability of natural mineral crystals with sufficiently low levels of contamination. In spite of these challenges, studies of anatase TiO_2 have been published at an increasing rate in recent years. The increased research effort is likely to be aided by works providing solutions to many of the obstacles that arise during the preparation of anatase $TiO_2(101)$ samples [34, 35].

The most stable anatase crystal facet is the (101) surface, which forms over 94% of the surface for macroscopic crystals [6, 7]. The anatase $TiO_2(101)$ surface has previously been investigated by low-energy electron diffraction (LEED) [36] and scanning probe microscopy [22, 34, 37–46] as well as photoemission [1, 47–59], infra-red reflection absorption [39] and near edge X-ray absorption fine structure [53] spectroscopies. The relaxed surface exhibits a non-reconstructed (1×1) bulk termination, as shown by the model in Figure 1.2. The sawtooth corrugation of the surface is composed of five- and six-fold coordinated Ti atoms (Ti_{5c} & Ti_{6c}) and two- and three-fold coordinated O atoms (O_{2c} & O_{3c}).

Similarly to the rutile $TiO_2(110)$ surface, bridging O_{2c} atoms at the anatase (101) surface may be removed during sample preparation or by electron bombardment [37, 44], forming surface O_b-vacs. The creation of O_b-vac leads to a reduced surface and induces Ti 3d BGS $\sim$1 eV below E_F [13, 54, 60, 61], suggesting the formation of polarons at the anatase (101) surface upon O_b-vac creation [38, 49]. In contrast to rutile, excess electrons at the anatase $TiO_2(101)$ surface can only

localise as polarons at defects [22, 38]. Monoatomic-height step edges, which contribute a non-negligible fraction of surface atoms [46], have also been shown to be associated with states in the band gap region [38].

Resonant photoemission measurements evidence a higher concentration of oxygen vacancies at the anatase TiO_2(101) surface than the rutile TiO_2(110) [54]. However, scanning tunnelling microscopy (STM) images reveal a relative absence of point defects at the anatase surface [62]. Subsequently, it has been shown that O_b-vacs at the anatase (101) surface migrate to the sub-surface region at temperatures above 200 K [44]. Hence, a thermally equilibrated coverage of 0.01 ML is achieved for the as-prepared surface at room temperature [44]. O_b-vacs have also been shown to aggregate as sub-surface clusters upon heating above room temperature [37].

Water Adsorption

The adsorption of water on anatase TiO_2(101) has recently been described in two review articles [7, 24]. Calculations have predicted that water dissociates at surface O-vacs, forming two bridging hydroxyls (OH) per vacancy [63]. As with rutile *h*-TiO_2(110), anatase *h*-TiO_2(101) is still reduced and predicted to have associated BGS [63, 64]. Typical sample preparation under UHV conditions results in surfaces possessing very low concentrations of surface O_b-vacs [44]. The relative scarcity of these highly reactive point defects likely explains the consensus that water predominantly adsorbs molecularly on the as-prepared anatase TiO_2(101) surface [8, 24, 59, 62, 63, 65, 66]. Although less reactive than surface O_b-vacs, sub-surface O_b-vacs remain able to influence water adsorption, shifting its desorption to higher temperatures, which suggests stronger binding due to the presence of these defects [65].

TPD measurements of water on anatase TiO_2(101) display peaks at 250 K, 190 K and 160 K [59]. The 250 K peak was assigned to chemisorption of water at Ti_{5c} sites. The second water layer physisorbs at bridging O_{2c} atoms at 190 K, followed by the growth of multilayer water below 160 K. X-ray photoemission measurements indicate that all water layers adsorb molecularly [59] and dynamic simulations support this assignment [66]. However, there is also evidence of a mixed monolayer of water and hydroxyls on anatase TiO_2(101) [58, 67].

1.3 Thesis Structure

The following chapter of this thesis details the theoretical fundamentals of techniques used in this work to study anatase and rutile TiO_2 surfaces. The chapter begins with a brief introduction to the generation of femtosecond laser pulses and their higher harmonics. Theoretical frameworks pertaining to ultra-fast and standard photoemission spectroscopy are introduced. Ancillary techniques of Auger electron spectroscopy and low-energy electron diffraction are also discussed in terms of interpretation of their experimental results rather than an in depth examination of their practical execution.

Chapter 3 describes the experimental apparatus employed to realise the results presented in subsequent chapters. Principally, two UHV chambers optimised for the study of surfaces are detailed, along with the laser systems belonging to each laboratory. A explanation of sample preparation procedures and auxiliary surface sensitive techniques is also provided.

In Chapter 4, a resonance in two-photon photoemission spectra at the reduced, rutile TiO_2(110) surface for photon energies between $\sim$3-4 eV is investigated. The dependence of the spectra on the surface condition and incident photon energy is characterised, allowing assignment of the initial and intermediate states relevant to this resonant photoexcitation process. These results provide insight into photoexcitation processes at the TiO_2(110) surface and the influence of common defects on the surface electronic structure.

Chapter 5 presents a two-photon and ultra-violet photoemission study of the electron-bombarded and water-covered anatase TiO_2(101) surface. This work focuses on the influence of defects and adsorbates on the surface electronic structure. The findings are compared to measurements of the surface as typically prepared under UHV conditions and may provide insight into the reactivity of the surface. A comparison is also drawn with similarly prepared rutile TiO_2(110) surfaces in an effort to explain the increased catalytic activity of anatase over rutile TiO_2.

The experimental work presented in Chapter 6, undertaken at the Artemis facility of the Rutherford Appleton Laboratory, interrogates the dynamics of charge trapping and recombination at the rutile TiO_2(110) surface via femtosecond-resolved, pump-probe photoemission spectroscopy. An infra-red-pumped experiment pro-

vides insight into the trapping time of photoexcited polarons. This result is compared to the dynamics observed under ultra-violet photoexcitation and the possible mechanisms governing the evolution of the excited state populations are discussed.

References

[1] M. J. Jackman, A. G. Thomas, and C. Muryn, "Photoelectron Spectroscopy Study of Stoichiometric and Reduced Anatase TiO_2(101) Surfaces: The Effect of Subsurface Defects on Water Adsorption at Near-Ambient Pressures," *The Journal of Physical Chemistry C*, vol. 119, no. 24, pp. 13682–13690, 2015.

[2] D. E. Starr, S. K. Shaikhutdinov, and H. J. Freund, "Gold supported on oxide surfaces: environmental effects as studied by STM," *Topics in Catalysis*, vol. 36, no. 1-4, pp. 33–41, 2005.

[3] U. Diebold, "The surface science of titanium dioxide," *Surface Science Reports*, vol. 48, no. 5-8, pp. 53–229, 2003.

[4] V. Henrich and P. Cox, *The Surface Science of Metal Oxides*. Cambridge University Press, 1994.

[5] L. Kavan, M. Grätzel, S. E. Gilbert, C. Klemenz, and H. J. Scheel, "Electrochemical and Photoelectrochemical Investigation of Single-Crystal Anatase," *Journal of the American Chemical Society*, vol. 118, no. 28, pp. 6716–6723, 1996.

[6] M. Lazzeri, A. Vittadini, and A. Selloni, "Structure and energetics of stoichiometric TiO_2 anatase surfaces," *Physical Review B*, vol. 63, no. 15, p. 155409, 2001.

[7] F. De Angelis, C. Di Valentin, S. Fantacci, A. Vittadini, and A. Selloni, "Theoretical Studies on Anatase and Less Common TiO_2 Phases: Bulk, Surfaces, and Nanomaterials," *Chemical Reviews*, vol. 114, no. 19, pp. 9708–9753, 2014.

[8] A. Vittadini, A. Selloni, F. P. Rotzinger, and M. Grätzel, "Structure and Energetics of Water Adsorbed at TiO_2 Anatase (101) and (001) Surfaces," *Physical Review Letters*, vol. 81, no. 14, pp. 2954–2957, 1998.

[9] A. Vittadini, M. Casarin, and A. Selloni, "Chemistry of and on TiO_2-anatase surfaces by DFT calculations: a partial review," *Theoretical Chemistry Accounts*, vol. 117, no. 5, pp. 663–671, 2007.

[10] J. Pan, G. Liu, G. Q. M. Lu, and H.-M. Cheng, "On the True Photoreactivity Order of $\{001\}$, $\{010\}$, and $\{101\}$ Facets of Anatase TiO_2 Crystals," *Angewandte Chemie International Edition*, vol. 50, no. 9, pp. 2133–2137, 2011.

[11] P. Tasker, "The stability of ionic crystal surfaces," *Journal of Physics C: Solid State Physics*, vol. 12, no. 22, pp. 4977–4984, 1979.

[12] C. L. Pang, R. Lindsay, and G. Thornton, "Structure of Clean and Adsorbate-Covered Single-Crystal Rutile TiO_2 Surfaces," *Chemical Reviews*, vol. 113, no. 6, pp. 3887–3948, 2013.

[13] C. M. Yim, C. L. Pang, and G. Thornton, "Oxygen Vacancy Origin of the Surface Band-Gap State of TiO_2," *Physical Review Letters*, vol. 104, no. 3, p. 036806, 2010.

[14] G. Cabailh, X. Torrelles, R. Lindsay, O. Bikondoa, I. Joumard, J. Zegenhagen, and G. Thornton, "Geometric structure of $TiO_2(1\times1)$: Achieving experimental consensus," *Physical Review B*, vol. 75, no. 24, p. 241403, 2007.

[15] R. Lindsay, A. Wander, A. Ernst, B. Montanari, G. Thornton, and N. M. Harrison, "Revisiting the Surface Structure of $TiO_2(110)$: A Quantitative low-Energy Electron Diffraction Study," *Physical Review Letters*, vol. 94, no. 24, p. 246102, 2005.

[16] O. Bikondoa, C. L. Pang, R. Ithnin, C. A. Muryn, H. Onishi, and G. Thornton, "Direct visualization of defect-mediated dissociation of water on $TiO_2(110)$," *Nature Materials*, vol. 5, no. 3, pp. 189–192, 2006.

[17] Z. Wang, B. Wen, Q. Hao, L.-M. Liu, C. Zhou, X. Mao, X. Lang, W.-J. Yin, D. Dai, A. Selloni, and X. Yang, "Localized Excitation of Ti^{3+} Ions in the Photoabsorption and Photocatalytic Activity of Reduced Rutile TiO_2," *Journal of the American Chemical Society*, vol. 137, no. 28, pp. 9146–9152, 2015.

[18] C. Di Valentin, G. Pacchioni, and A. Selloni, "Electronic Structure of Defect States in Hydroxylated and Reduced Rutile $TiO_2(110)$ Surfaces," *Physical Review Letters*, vol. 97, no. 16, p. 166803, 2006.

[19] S. Wendt, P. T. Sprunger, E. Lira, G. K. H. Madsen, Z. Li, J. O. Hansen, J. Matthiesen, A. Blekinge-Rasmussen, E. Laegsgaard, B. Hammer, and

F. Besenbacher, "The Role of Interstitial Sites in the Ti3d Defect State in the Band Gap of Titania," *Science*, vol. 320, no. 5884, pp. 1755–1759, 2008.

[20] P. G. Moses, A. Janotti, C. Franchini, G. Kresse, and C. G. Van de Walle, "Donor defects and small polarons on the TiO_2(110) surface," *Journal of Applied Physics*, vol. 119, no. 18, p. 181503, 2016.

[21] S. Chretien and H. Metiu, "Electronic Structure of Partially Reduced Rutile TiO_2(110) Surface: Where Are the Unpaired Electrons Located?," *The Journal of Physical Chemistry C*, vol. 115, no. 11, pp. 4696–4705, 2011.

[22] M. Setvin, C. Franchini, X. Hao, M. Schmid, A. Janotti, M. Kaltak, C. G. Van de Walle, G. Kresse, and U. Diebold, "Direct View at Excess Electrons in TiO_2 Rutile and Anatase," *Physical Review Letters*, vol. 113, no. 8, p. 086402, 2014.

[23] M. Henderson, "The interaction of water with solid surfaces: fundamental aspects revisited," *Surface Science Reports*, vol. 46, no. 1-8, pp. 1–308, 2002.

[24] K. Bourikas, C. Kordulis, and A. Lycourghiotis, "Titanium Dioxide (Anatase and Rutile): Surface Chemistry, Liquid-Solid Interface Chemistry, and Scientific Synthesis of Supported Catalysts," *Chemical Reviews*, vol. 114, no. 19, pp. 9754–9823, 2014.

[25] I. M. Brookes, C. A. Muryn, and G. Thornton, "Imaging Water Dissociation on TiO_2(110)," *Physical Review Letters*, vol. 87, no. 26, p. 266103, 2001.

[26] H. H. Kristoffersen, J. Ø. Hansen, U. Martinez, Y. Y. Wei, J. Matthiesen, R. Streber, R. Bechstein, E. Lægsgaard, F. Besenbacher, B. Hammer, and S. Wendt, "Role of Steps in the Dissociative Adsorption of Water on Rutile TiO_2(110)," *Physical Review Letters*, vol. 110, no. 14, p. 146101, 2013.

[27] M. A. Henderson, "An HREELS and TPD study of water on TiO_2(110): the extent of molecular versus dissociative adsorption," *Surface Science*, vol. 355, no. 1-3, pp. 151–166, 1996.

[28] L.-M. Liu, C. Zhang, G. Thornton, and A. Michaelides, "Structure and dynamics of liquid water on rutile TiO_2(110)," *Physical Review B*, vol. 82, no. 16, p. 161415, 2010.

[29] L. E. Walle, A. Borg, P. Uvdal, and A. Sandell, "Experimental evidence for mixed dissociative and molecular adsorption of water on a rutile TiO_2(110)

surface without oxygen vacancies," *Physical Review B*, vol. 80, no. 23, p. 235436, 2009.

[30] L. E. Walle, A. Borg, P. Uvdal, and A. Sandell, "Probing the influence from residual Ti interstitials on water adsorption on TiO_2(110)," *Physical Review B*, vol. 86, no. 20, p. 205415, 2012.

[31] L. Walle, D. Ragazzon, A. Borg, P. Uvdal, and A. Sandell, "Competing water dissociation channels on rutile TiO_2(110)," *Surface Science*, vol. 621, pp. 77–81, 2014.

[32] L. E. Walle, D. Ragazzon, A. Borg, P. Uvdal, and A. Sandell, "Photoemission studies of water dissociation on rutile TiO_2(110): Aspects on experimental procedures and the influence of steps," *Applied Surface Science*, vol. 303, pp. 245–249, 2014.

[33] D. A. Duncan, F. Allegretti, and D. P. Woodruff, "Water does partially dissociate on the perfect TiO_2(110) surface: A quantitative structure determination," *Physical Review B*, vol. 86, no. 4, p. 045411, 2012.

[34] M. Setvín, B. Daniel, V. Mansfeldova, L. Kavan, P. Scheiber, M. Fidler, M. Schmid, and U. Diebold, "Surface preparation of TiO_2 anatase (101): Pitfalls and how to avoid them," *Surface Science*, vol. 626, pp. 61–67, 2014.

[35] O. Dulub and U. Diebold, "Preparation of a pristine TiO_2 anatase (101) surface by cleaving," *Journal of Physics: Condensed Matter*, vol. 22, no. 8, p. 084014, 2010.

[36] X.-Q. Gong, A. Selloni, O. Dulub, P. Jacobson, and U. Diebold, "Small Au and Pt Clusters at the Anatase TiO_2(101) Surface: Behavior at Terraces, Steps, and Surface Oxygen Vacancies," *Journal of the American Chemical Society*, vol. 130, no. 1, pp. 370–381, 2008.

[37] M. Setvin, M. Schmid, and U. Diebold, "Aggregation and electronically induced migration of oxygen vacancies in TiO_2 anatase," *Physical Review B*, vol. 91, no. 19, p. 195403, 2015.

[38] M. Setvin, X. Hao, B. Daniel, J. Pavelec, Z. Novotny, G. S. Parkinson, M. Schmid, G. Kresse, C. Franchini, and U. Diebold, "Charge Trapping at the Step Edges of TiO_2 Anatase (101)," *Angewandte Chemie International Edition*, vol. 53, no. 18, pp. 4714–4716, 2014.

[39] M. Setvin, M. Buchholz, W. Hou, C. Zhang, B. Stöger, J. Hulva, T. Simschitz, X. Shi, J. Pavelec, G. S. Parkinson, M. Xu, Y. Wang, M. Schmid, C. Wöll,

A. Selloni, and U. Diebold, “A Multitechnique Study of CO Adsorption on the TiO_2 Anatase (101) Surface,” *The Journal of Physical Chemistry C*, vol. 119, no. 36, pp. 21044–21052, 2015.

[40] M. Setvin, U. Aschauer, P. Scheiber, Y. Li, W. Hou, M. Schmid, A. Selloni, and U. Diebold, “Reaction of O_2 with Subsurface Oxygen Vacancies on TiO_2 Anatase (101),” *Science*, vol. 341, no. 6149, pp. 988–991, 2013.

[41] M. Setvin, B. Daniel, U. Aschauer, W. Hou, Y.-F. Li, M. Schmid, A. Selloni, and U. Diebold, “Identification of adsorbed molecules via STM tip manipulation: CO, H_2O, and O_2 on TiO_2 anatase (101),” *Physical Chemistry Chemical Physics*, vol. 16, no. 39, pp. 21524–21530, 2014.

[42] O. Stetsovych, M. Todorović, T. K. Shimizu, C. Moreno, J. W. Ryan, C. P. León, K. Sagisaka, E. Palomares, V. Matolín, D. Fujita, R. Perez, and O. Custance, “Atomic species identification at the (101) anatase surface by simultaneous scanning tunnelling and atomic force microscopy,” *Nature Communications*, vol. 6, no. 101, p. 7265, 2015.

[43] D. C. Grinter, M. Nicotra, and G. Thornton, “Acetic Acid Adsorption on Anatase TiO_2(101),” *The Journal of Physical Chemistry C*, vol. 116, no. 21, pp. 11643–11651, 2012.

[44] P. Scheiber, M. Fidler, O. Dulub, M. Schmid, U. Diebold, W. Hou, U. Aschauer, and A. Selloni, “(Sub)Surface Mobility of Oxygen Vacancies at the TiO_2 Anatase (101) Surface,” *Physical Review Letters*, vol. 109, no. 13, p. 136103, 2012.

[45] Y. He, A. Tilocca, O. Dulub, A. Selloni, and U. Diebold, “Local ordering and electronic signatures of submonolayer water on anatase TiO_2(101),” *Nature Materials*, vol. 8, no. 7, pp. 585–589, 2009.

[46] X.-Q. Gong, A. Selloni, M. Batzill, and U. Diebold, “Steps on anatase TiO_2(101),” *Nature Materials*, vol. 5, no. 8, pp. 665–670, 2006.

[47] P. Reckers, M. Dimamay, J. Klett, S. Trost, K. Zilberberg, T. Riedl, B. A. Parkinson, J. Brötz, W. Jaegermann, and T. Mayer, “Deep and Shallow TiO_2 Gap States on Cleaved Anatase Single Crystal (101) Surfaces, Nanocrystalline Anatase Films, and ALD Titania Ante and Post Annealing,” *The Journal of Physical Chemistry C*, vol. 119, no. 18, pp. 9890–9898, 2015.

[48] T. C. Rödel, F. Fortuna, F. Bertran, M. Gabay, M. J. Rozenberg, A. F. Santander-Syro, and P. Le Fèvre, “Engineering two-dimensional electron

gases at the (001) and (101) surfaces of TiO_2 anatase using light," *Physical Review B*, vol. 92, no. 4, p. 041106, 2015.

[49] M. Jackman, P. Deák, and K. Syres, "Observation of vacancy-related polaron states at the surface of anatase and rutile TiO_2 by high-resolution photoelectron spectroscopy," *http://arxiv.org/abs/1406.3385*, 2014.

[50] S. Moser, L. Moreschini, J. Jaćimović, O. S. Barišić, H. Berger, A. Magrez, Y. J. Chang, K. S. Kim, A. Bostwick, E. Rotenberg, L. Forró, and M. Grioni, "Tunable Polaronic Conduction in Anatase TiO_2," *Physical Review Letters*, vol. 110, no. 19, p. 196403, 2013.

[51] S. Moser, S. Fatale, P. Krüger, H. Berger, P. Bugnon, A. Magrez, H. Niwa, J. Miyawaki, Y. Harada, and M. Grioni, "Electron-Phonon Coupling in the Bulk of Anatase TiO_2 Measured by Resonant Inelastic X-Ray Spectroscopy," *Physical Review Letters*, vol. 115, no. 9, p. 096404, 2015.

[52] K. Syres, A. Thomas, F. Bondino, M. Malvestuto, and M. Gratzel, "Dopamine Adsorption on Anatase TiO_2(101): A Photoemission and NEXAFS Spectroscopy Study," *Langmuir*, vol. 26, no. 18, pp. 14548–14555, 2010.

[53] K. L. Syres, A. G. Thomas, W. R. Flavell, B. F. Spencer, F. Bondino, M. Malvestuto, A. Preobrajenski, and M. Grätzel, "Adsorbate-Induced Modification of Surface Electronic Structure: Pyrocatechol Adsorption on the Anatase TiO_2(101) and Rutile TiO_2(110) Surfaces," *The Journal of Physical Chemistry C*, vol. 116, no. 44, pp. 23515–23525, 2012.

[54] A. G. Thomas, W. R. Flavell, A. K. Mallick, A. R. Kumarasinghe, D. Tsoutsou, N. Khan, C. Chatwin, S. Rayner, G. C. Smith, R. L. Stockbauer, S. Warren, T. K. Johal, S. Patel, D. Holland, A. Taleb, and F. Wiame, "Comparison of the electronic structure of anatase and rutile TiO_2 single-crystal surfaces using resonant photoemission and x-ray absorption spectroscopy," *Physical Review B*, vol. 75, no. 3, p. 035105, 2007.

[55] A. G. Thomas, W. R. Flavell, A. R. Kumarasinghe, A. K. Mallick, D. Tsoutsou, G. C. Smith, R. Stockbauer, S. Patel, M. Grätzel, and R. Hengerer, "Resonant photoemission of anatase TiO_2(101) and (001) single crystals," *Physical Review B*, vol. 67, no. 3, p. 035110, 2003.

[56] A. Thomas, W. Flavell, C. Chatwin, S. Rayner, D. Tsoutsou, A. Kumarasinghe, D. Brete, T. Johal, S. Patel, and J. Purton, "Adsorption of biisonicotinic acid on anatase TiO_2(101) and (001) studied by photoemission

and NEXAFS spectroscopy," *Surface Science*, vol. 592, no. 1-3, pp. 159–168, 2005.

[57] A. G. Thomas and K. L. Syres, "Observation of UV-induced Auger features in catechol adsorbed on anatase TiO_2(101) single crystal surface," *Applied Physics Letters*, vol. 100, no. 17, p. 171603, 2012.

[58] C. E. Patrick and F. Giustino, "Structure of a Water Monolayer on the Anatase TiO_2(101) Surface," *Physical Review Applied*, vol. 2, no. 1, p. 014001, 2014.

[59] G. S. Herman, Z. Dohnálek, N. Ruzycki, and U. Diebold, "Experimental Investigation of the Interaction of Water and Methanol with Anatase-TiO_2(101)," *The Journal of Physical Chemistry B*, vol. 107, no. 12, pp. 2788–2795, 2003.

[60] R. Sanjines, H. Tang, H. Berger, F. Gozzo, G. Margaritondo, and F. Levy, "Electronic structure of anatase TiO_2 oxide," *Journal of Applied Physics*, vol. 75, no. 6, p. 2945, 1994.

[61] A. C. Papageorgiou, N. S. Beglitis, C. L. Pang, G. Teobaldi, G. Cabailh, Q. Chen, A. J. Fisher, W. A. Hofer, and G. Thornton, "Electron traps and their effect on the surface chemistry of TiO_2(110)," *Proceedings of the National Academy of Sciences of the United States of America*, vol. 107, no. 6, pp. 2391–2396, 2010.

[62] Y. He, O. Dulub, H. Cheng, A. Selloni, and U. Diebold, "Evidence for the Predominance of Subsurface Defects on Reduced Anatase TiO_2(110)," *Physical Review Letters*, vol. 102, no. 10, p. 106105, 2009.

[63] A. Tilocca and A. Selloni, "Structure and Reactivity of Water Layers on Defect-Free and Defective Anatase TiO_2(101) Surfaces," *The Journal of Physical Chemistry B*, vol. 108, no. 15, pp. 4743–4751, 2004.

[64] H. Sun, D. J. Mowbray, A. Migani, J. Zhao, H. Petek, and A. Rubio, "Comparing Quasiparticle H_2O Level Alignment on Anatase and Rutile TiO_2," *ACS Catalysis*, vol. 5, no. 7, pp. 4242–4254, 2015.

[65] U. Aschauer, Y. He, H. Cheng, S.-C. Li, U. Diebold, and A. Selloni, "Influence of Subsurface Defects on the Surface Reactivity of TiO_2: Water on Anatase (101)," *The Journal of Physical Chemistry C*, vol. 114, no. 2, pp. 1278–1284, 2010.

[66] A. Tilocca and A. Selloni, “Vertical and Lateral Order in Adsorbed Water Layers on Anatase TiO_2(101),” *Langmuir*, vol. 20, no. 19, pp. 8379–8384, 2004.

[67] L. E. Walle, A. Borg, E. M. J. Johansson, S. Plogmaker, H. Rensmo, P. Uvdal, and A. Sandell, “Mixed Dissociative and Molecular Water Adsorption on Anatase TiO_2(101),” *The Journal of Physical Chemistry C*, vol. 115, no. 19, pp. 9545–9550, 2011.

Chapter 2

Theoretical Aspects of Techniques

Abstract

Both a practical and theoretical understanding of experimental instrumentation is required for proper interpretation of scientific results. Providing a theoretical consideration of the experimental techniques used in this work, this chapter focuses primarily on photoemission spectroscopy. Ancillary techniques of low-energy electron diffraction and Auger electron spectroscopy are also described.

2.1 Femtosecond Lasers

The advent of femtosecond (1 fs = 10^{-15} s) lasers in the late 1980s allowed the dynamics of ultra-fast processes to be studied for the first time. Femtosecond laser experiments typically employ pump-probe techniques, in which the first pulse creates a perturbation to the system which is interrogated by the probe pulse. Precisely what information can be obtained from these measurements depends upon the observation method and excitation scheme.

The simplest laser cavity consists of a gain medium enclosed by two mirrors. The gain medium is pumped to create a population inversion and spontaneously emitted photons stimulate the emission of further photons. Optical modes exist within the cavity as standing waves, with nodes located at the two cavity mirrors. Hence, these longitudinal modes have a frequencies of $\nu = \frac{nc}{2L}$, where L is the cavity length, c is the speed of light in a vacuum and n is an integer. In order to obtain femtosecond pulses, the modes within the cavity must oscillate in phase with one another. This is refered to as mode-locking. By aligning the phases of all the longitudinal modes in the cavity at one point, a very small region of constructive interference is achieved, which lasts for just a few femtoseconds. The greater the number of modes there are, the smaller this region becomes and so broadband lasers are a fundamental requirement for ultra-fast pulses. The energy-time uncertainty principle, which may be used to determine the shortest possible pulse duration, Δt, for a pulse with spectral width $\Delta\nu$, is given by:

$$\Delta\nu\Delta t \geq \frac{4ln2}{2\pi} = 0.441, \tag{2.1}$$

Equation 2.1 is known as the time-bandwidth product. $\Delta\nu$ and Δt, if expressed in units of Hertz and seconds, respectively, are the full-widths at half maximum (FWHM) of the laser pulse.

Mode-locking in a Ti:Sapphire laser exploits the change in the refractive index of a medium induced by an intense incident electric field, known as the optical Kerr effect. As a result of this effect, Gaussian beams (which are produced by most lasers) experience a varation in refractive index over its profile equivalent to a positive lens, resulting in self-focussing of the laser pulse. Self-focussing is exploited in femtosecond lasers to achieve mode-locking, by placing an aperture around the waist of the focused beam and removing the unfocused CW pump

laser light. In practice, Kerr-lens mode-locking does not occur spontaneously and is typically triggered by vibrating one of the laser cavity mirrors, which induces a noise spike in the intensity of the beam over the lower intensity continuous wave (CW) light.

Mode-locked lasers typically deliver pulse powers limited to nanojoules per pulse. In order to obtain higher pulse powers, of the order of milijoules per pulse, further amplification can be introduced via a chirped-pulse amplification system. Before amplification, the seeding pulse is temporally stretched (positive chirp) using gratings and collimation optics to avoid non-linear processes and damage to the laser gain medium. The amplifier is typically pumped by a nanosecond Nd:YLF laser. Switching of Pockels cells allow entry of the nanosecond seed pulse into the amplifier cavity to activate the gain medium. After several passes through the Ti:Sapphire gain medium, the cavity outputs an amplified pulse. The timing of the Pockels cells is optimised to maximise laser power and minimise dispersion. Following ejection from the amplifier cavity, an optical compressor consisting of another diffraction grating and mirrors introduces negative chirp to reduce the temporal profile of the laser pulse. This amplified laser beam permits the operation of tuneable optical parametric amplifiers (OPAs) or higher harmonic generation, which extend the accessible energy range by exploiting non-linear optical processes.

Non-Linear Optics

Transmission of light through a medium distorts the electron density within the material, which induces a polarisation of the sample that is in most cases proportional to the applied electric field. In this case of linear optics, light may be reflected, delayed or attenuated while passing through a medium, however, its frequency remains unaltered. When the light is of greater intensity, such as that generated by a laser, the polarisation induced in the medium is often not a linear function of the applied electric field, $\mathbf{E}$, but can be described by non-linear optics. The non-linear polarisation, $\mathbf{P}$, is usually expanded in a power series:

$$\mathbf{P} = \varepsilon_0 \left(\chi^{(1)}\mathbf{E} + \chi^{(2)}\mathbf{E}^2 + \chi^{(3)}\mathbf{E}^3 \ldots \right), \tag{2.2}$$

where ε_0 is the permittivity of free space, and $\chi^{(n)}$ is the n^{th} order susceptibility of

the medium. It is required that $\chi^{(3)}\mathbf{E}^3 \ll \chi^{(2)}\mathbf{E}^2 \ll \chi^{(1)}\mathbf{E}$ for the series to converge.

The electric field of the laser light of frequency ω takes the form $\mathbf{E} = \mathbf{E}_\omega cos\,(\omega t)$. Substituting this into Equation 2.2 allows it to be written as:

$$\mathbf{P} = \mathbf{P_0} + \mathbf{P_1} cos\,(\omega t) + \mathbf{P_2} cos\,(2\omega t) + \mathbf{P_3} cos\,(3\omega t) + \ldots \tag{2.3}$$

The first term is the direct current term, the second corresponds to the fundamental harmonic, the third to the second harmonic term and so on. Hence, the non-linear response of the medium gives rise to components of light at frequencies of ω, 2ω, 3ω etc..

Second harmonic generation gives rise to light at the frequency 2ω and is commonly employed to extend the energy range of laser systems. This technique requires the media to be non-centrosymmetric and hence anisotropic crystals are used, rather than gases or liquid mediums. Since 11 of the 32 crystal classes possess inversion symmetry, this constraint is useful in excluding many materials from consideration for second-order nonlinear optical processes [1]. However, this phenomenon is not necessarily observed when intense light passes through a medium that responds non-linearly, due to the additional constraints that both the energy and momentum of the photons must be conserved. These quantities may be conserved through a process called phase matching. Employing an anisotropic medium in which the refractive index is different along each axis of the sample, the wavelength dependence of the refractive index can be compensated for. By rotating the optical axis of such a material in the laser beam, the phase velocity of both frequencies can be matched, which dramatically increases the efficiency of the harmonic generation process. In optical parametric amplifiers, sequential optical mixing is used to create tuneable fs pulses in the visible to ultra-violet regions of the electromagnetic spectrum.

High harmonic generation may be achieved in media with or without inversion symmetry. In centrosymmetric media, such as gases, frequencies of light at odd multiples of the original frequency (ω) may be generated, up to a characteristic cut-off energy . The energy of this cut-off is related to the ponderomotive energy, which describes the average oscillation energy that a free electron gains in the radiation field of the laser pulse [2, 3]. Phase matching must also be considered in the generation of high harmonics in order to optimise the efficiency of the har-

monic generation process. Although a much smaller fraction of the input laser power may be converted to higher harmonics than in second harmonic generation, high harmonic generation is useful for obtaining ultra-fast extreme ultra-violet or soft X-ray pulses.

2.2 Photoemission Spectroscopy

Photoemission spectroscopy (PES) has proven itself a popular technique for studying the electronic density of states of condensed matter systems. Variants of this versatile technique allow energy- and time-resolved studies of occupied core and valence band levels, as well as unoccupied levels above the Fermi level (E_F).

2.2.1 Single-photon Photoemission Spectroscopy

In this work, the single-photon photoemisson (1PPE) techniques of ultra-violet (UPS) and X-ray (XPS) photoemission spectroscopy are used to monitor valence band and core levels, respectively. The absorption of a photon of energy $h\nu$ may lead to photoemission of a core or valence band electron with energy ϵ_i so long as $h\nu + \epsilon_i > E_{vac}$. In this case, the electron is able to overcome its binding force towards the atom's nucleus and surpass the vacuum level (E_{vac}). A schematic of this process is shown in Figure 2.1a.

In XPS spectra, the core-level peak shape is given by a Voigt lineshape (a convolution of Lorentzian and Gaussian lineshapes). The width of the Lorentzian term is given by the inherent line width, while the Gaussian peak width arises from experimental broadening due to factors such as the energy resolution of the analyser, the finite width of the photon source and thermal broadening. The inherent line width of a core level, Γ, is related to the core-hole lifetime, τ_{hole}, by Heisenberg's uncertainty principle [4]:

$$\Gamma = \frac{\hbar}{\tau_{hole}}, \tag{2.4}$$

UPS is better suited than XPS to studies of the valence band of surfaces due to

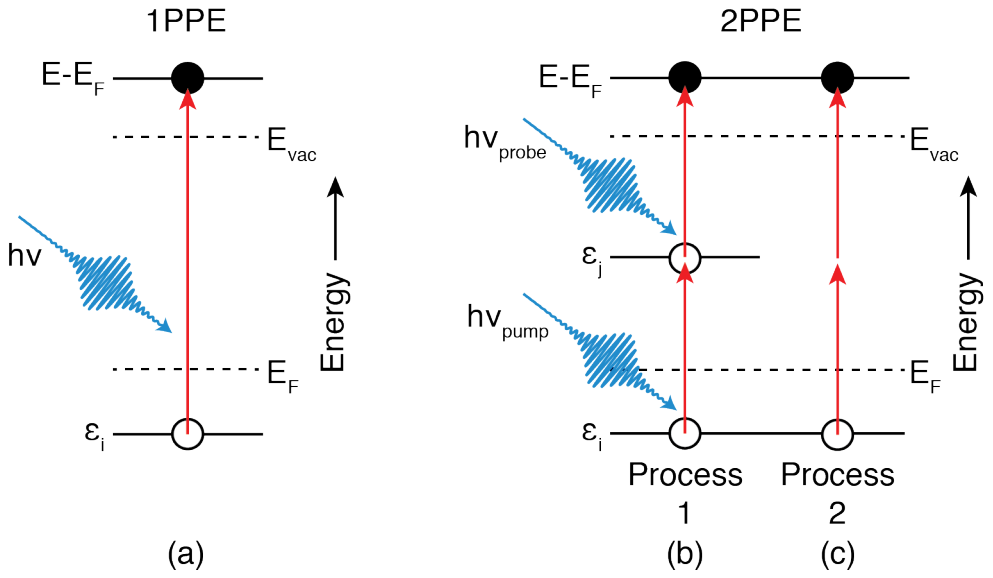

Figure 2.1: Schematic of possible excitation processes for (a) 1PPE and (b) & (c) 2PPE .

the shorter kinetic energy range of photoemitted electrons (∼50 eV). UPS allows the binding and orientation of adsorbates on the surface to be studied, and is also sensitive to the sample workfunction (Φ) [5].

A complementary single-photon technique, inverse photoemission spectroscopy, can be used to gain insight into the density of unoccupied states above E_F.

2.2.2 Two-photon Photoemission Spectroscopy

The capabilities of 1PPE and inverse photoemission spectroscopy are combined in two-photon photoemission spectroscopy (2PPE), which provides information pertaining to occupied and unoccupied states simultaneously. This pump-probe technique has been used extensively to study image potential and surface states at clean and adsorbate-covered metal surfaces [6]. By ensuring that $E_F < h\nu_{pu} + \epsilon_i < E_{vac}$, an electron in an initial state ($|i\rangle$) is excited to an unoccupied intermediate state ($|j\rangle$), of energy (ϵ_j), following the adsorption of a pump photon ($h\nu_{pu}$). This excited state electron may then undergo photoemission by absorbing a second, probe photon ($h\nu_{pr}$) within the lifetime of state $|j\rangle$, providing $h\nu_{pr} + \epsilon_j > E_{vac}$.

In addition to the excitation process described above, an electron in state $|i\rangle$ may also adsorb two photons simultaneously and undergo photoemission via a virtual intermediate state. A schematic of photoexcitation via real or virtual intermediate

states is shown in Figure 2.1b & c, respectively. When photoemission is due to coherent excitation from an occupied state ($|i\rangle$) via a virtual intermediate state (Process 2), it gives rise to a peak in the 2PPE spectrum at a final state energy ($E - E_F$) given by:

$$E - E_F = \epsilon_i + h\nu_{pu} + h\nu_{pr}, \tag{2.5}$$

When 2PPE is due to two independent, step-like excitation processes via a real intermediate state ($|j\rangle$) (Process 1), a peak is seen in the 2PPE spectrum at:

$$E - E_F = \epsilon_j + h\nu_{pr}, \tag{2.6}$$

Hence, it is possible to differentiate between these excitation processes by plotting the photon energy dependence of the spectral region. In monochromatic 2PPE measurements ($h\nu_{pu} = h\nu_{pr}$), Equation 2.5 results in a line with a gradient of two, while the energy dependence of Equation 2.6 has a gradient of one. By extrapolating to the point where $h\nu_{pu} = h\nu_{pr} = 0$ eV the energy of states $|i\rangle$ and $|j\rangle$ may be determined. Additionally, the point at which these two lines intercept gives the resonant photon energy for these states $h\nu_{res}$. These features are illustrated in Figure 2.2. Although the photon energy dependence of 2PPE features permits identification of the states involved, little is known about the underlying elementary excitation processes [6].

2PPE may also be used to investigate the dynamics of excitation processes. By delaying $h\nu_{pr}$ relative to $h\nu_{pu}$ the lifetime of the unoccupied state may be extracted. Time-resolved 2PPE (TR-2PPE) has become increasingly powerful since the advent of ultra-fast femtosecond laser pulses. In bichromatic 2PPE measurements ($h\nu_{pu} \neq h\nu_{pr}$), TR-2PPE spectra are required to verify the order of the photoexcitation process.

Optical Bloch Equations

Although the elementary excitation processes which give rise to 2PPE spectra are not fully understood, time- and energy-resolved spectra may be described phe-

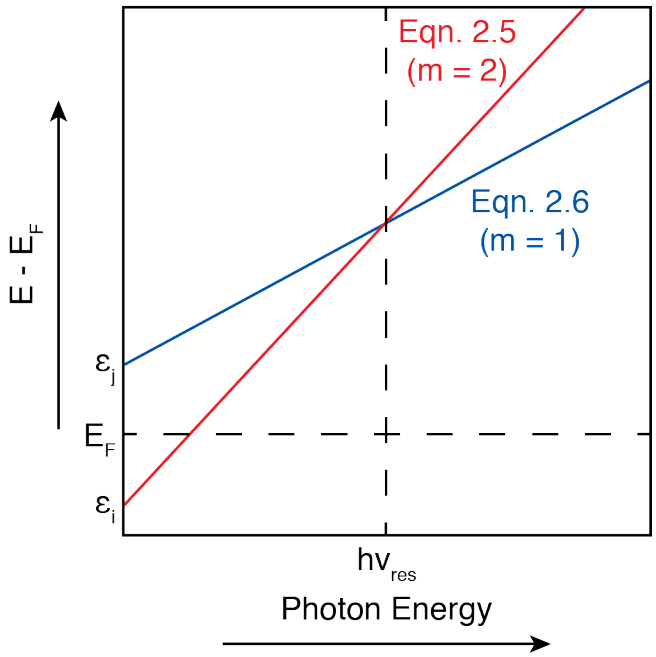

Figure 2.2: Photon energy dependence of 2PPE excitation processes described by Equations 2.5 (red) & 2.6 (blue), with gradients (m) of one or two, respectively, for monochromatic 2PPE measurements. The y-intercept of these lines gives the energy of states $|i\rangle$ and $|j\rangle$, respectively. The resonant photon energy ($h\nu_{res}$) is indicated by the dashed vertical line.

nomenologically by parameterised optical Bloch equations. This description was derived for metal surfaces [6], however, it has also been applied to semiconductor surfaces [7, 8]. 2PPE excitation processes can differ in their degree of coherence, which is defined in terms of the phase relation between the photoexcited electron and its hole.

Early theoretrical treatments of 2PPE spectra focused on coherent excitation processes, in which phase relations are maintained. This allowed the form and intensity of 2PPE spectra to be related to the density of states of the material. In their study of image states at the Cu(111) surface, Wallauer & Fauster found that an additional contribution was required in this model to fully describe the spectral intensity of photoemission from the unoccupied state [9]. This contribution was attributed to incoherent excitation processes, in which the scattering events at defects and relaxation processes break the phase relation between initial and final states.

Femtosecond laser pulses allow the dynamics of electron processes to be followed in the real time domain. The key physics of 2PPE spectra obtained using

ultra-fast laser pulses depends upon the relative time scales of the relaxation (T_1) and dephasing (T_2) times of the unoccupied state, and the laser pulse duration (t_p). In the case that $t_p \gg T_2$, there is no coherence effect, as there is no coherent superposition of the polarisation and electromagnetic field oscillations. This is typically the case for the nanosecond laser pulses used to attain high energy resolution 2PPE spectra. However, if t_p is comparable to or shorter than T_2, a coherent interaction is required to properly describe the temporal evolution of the transition dipole moment of the material and the photon field. This can be accomplished using the Liouville-von Neumann equation, which describes the temporal evolution of the density matrix ρ of the interacting system:

$$\frac{d\rho}{dt} = -i\left[H_0 + H_{int}^c, \rho\right] - i\left[H_{int}^r, \rho\right], \tag{2.7}$$

where H_0 is the unperturbed Hamiltonian of the electronic system, H_{int}^r is a random perturbation responsible for the relaxation of the excited medium and H_{int}^c is the coherent interaction with the photon field.

In the regime where the correlation time of the random force H_{int}^r is comparable to the duration of interaction with the photon pulse, the second term in Equation 2.7 may be approximated in terms of a relaxation time describing the asymptotic evolution of the system. This relaxation time can be introduced phenomenologically, in the form of the optical Bloch equations for the density matrix ρ.

The optical Bloch equations for a three-level system consisting of initial $|i\rangle$, intermediate $|j\rangle$ and final $|p\rangle$ states result in a density matrix such that:

$$\rho(t) = \begin{pmatrix} \rho_{ii} & \rho_{ij} & \rho_{ip} \\ \rho_{ji} & \rho_{jj} & \rho_{jp} \\ \rho_{pi} & \rho_{pj} & \rho_{pp} \end{pmatrix}. \tag{2.8}$$

There are therefore two excitation pathways to reach the final photoelectron state ρ_{pp} from the initial state ρ_{ii}. The first is a step-by-step one-photon process via the intermediate state: (1) $\rho_{ii} \rightarrow \rho_{ij} \rightarrow \rho_{jj} \rightarrow \rho_{jp} \rightarrow \rho_{pp}$ (plus their complex conjugates). This process produces an intermediate state peak in the 2PPE spectrum and also gives its population relaxation in TR-2PPE spectra. The second process is a two-photon ionisation process via a virtual state (2) $\rho_{ii} \rightarrow \rho_{ij} \rightarrow \rho_{ip} \rightarrow \rho_{jp} \rightarrow$

ρ_{pp} (plus their complex conjugates). Process (2) gives rise to an initial state peak in the 2PPE spectrum.

In order to obtain a steady state equation for 2PPE spectra it is convienient to introduce a single photon lineshape for the $|i\rangle \rightarrow |j\rangle$ transition, $I_{ij}(h\nu) = (h\nu - \epsilon_{ij} - i/T_2^{ij})$ where ϵ_{ij} is the energy difference between the initial and intermediate states and T_2^{ij} is the dephasing between electrons in these states. Hence, the 2PPE spectral intensity can be written as:

$$P\left(h\nu_{pu}, h\nu_{pr}; \epsilon\right) = 2T_1 Im\left[I_{ji}\left(h\nu_{pu}\right)\right] \cdot Im\left[I_{pj}\left(h\nu_{pr}\right)\right] - Im\left[I_{ji}\left(h\nu_{pu}\right) I_{pj}\left(h\nu_{pr}\right) I_{pi}\left(h\nu_{pu} + h\nu_{pr}\right)\right], \quad (2.9)$$

Here the first term corresponds to a step-by-step incoherent process (1), and the second to a coherent two-photon process (2). Both terms depend on the same one-photon process $I_{pj}(h\nu_{pr})$, which indicates that the intermediate state can be populated by non-resonant coherent virtual excitation.

$$P(h\nu_{pu}, h\nu_{pr}; \epsilon_p) = \frac{1}{(h\nu_{pr} + \epsilon_j - \epsilon_p)^2 + (1/T_2^j)^2} \times \left[\frac{\tau_i^*}{(h(\nu_{pu} + \nu_{pr}) + \epsilon_i - \epsilon_p)^2 + \tau_i^{*2}} + 2T_1\tau_j^* \frac{1/T_2^{ji}}{(h\nu_{pu} + \epsilon_i - \epsilon_j)^2 + (1/T_2^{ji})^2}\right], \quad (2.10)$$

Equation 2.10 reveals that the 2PPE intensity is proportional to the sum of two Lorentzian terms. The first term on the right hand side is due to coherent excitation, process (2) in Figure 2.1 and gives rise to a peak in 2PPE spectra at an energy described by Equation 2.5. The left hand side term arises from a mixture of processes (1) & (2), namely incoherent and non-resonant coherent excitations, which produces an additional 2PPE feature whose energy is described by Equation 2.6.

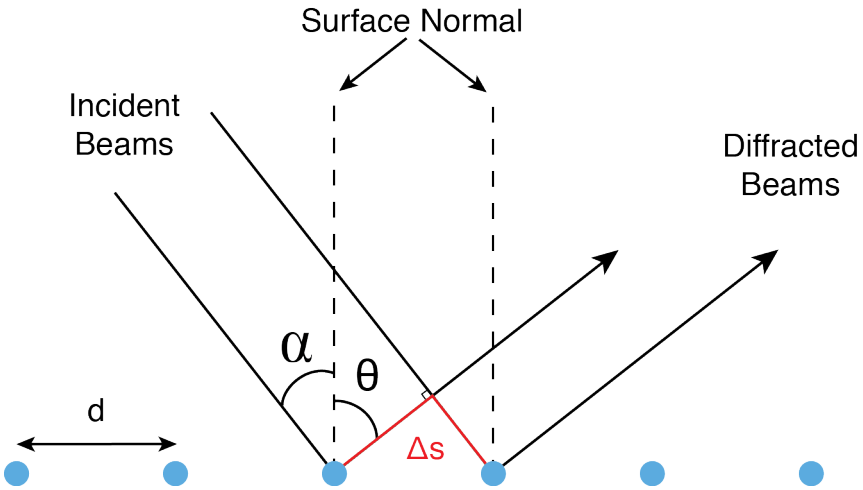

Figure 2.3: Schematic of diffraction from a one dimensional array of atoms (blue circles), separated by a distance d. The path difference (Δs) between the incident and diffracted beams is shown by red lines.

2.3 Low-energy Electron Diffraction

Experiments in the 1920s by Clinton Davisson and George Thomson investigating electron scattering at gold and nickel single crystal surfaces demonstrated that the elastically back-scattered electrons emerge in preferential directions [10–13]. The distribution of these diffracted electrons is governed by the periodic nature of the crystal lattice. This paved the way for the development of low-energy electron diffraction (LEED), which has proved itself to be an invaluable tool for elucidating the structure of many surfaces. Accordingly, Davisson and Thomson were awarded the Nobel Prize in Physics in 1937 for their discovery.

Figure 2.3 illustrates how an incident monochromatic electron beam is diffracted by a one dimensional array of atoms, separated by a distance d. By considering two parallel beams it is seen that the path difference Δs between the two beams following diffraction is given by:

$$\Delta s = d(sin\theta - sin\alpha), \tag{2.11}$$

where α and θ are the angles of the incident and diffracted beams respectively.

The Bragg conditions for constructive interference between the two beams are satisfied when Δs is equal to an integer number, n, of wavelengths λ. Hence, it

holds that constructive interference occurs when:

$$\Delta s = d(sin\theta - sin\alpha) = n \cdot \lambda, \tag{2.12}$$

In the simplest case, where $n = 1$ and α and θ are known, the atomic separation d can be determined using Equation 2.12. This case is easily extended to two dimensions, allowing the structure of a crystalline surface to be determined. Additionally, LEED-IV measurements, in which the position and intensity of diffracted beams are measured as a function of electron beam energy, allow precise determination of the three dimensional structure of the first few atomic layers of the surface. However, in this work such investigations are not required.

An important consideration in the study of surface science is the sensitivity of the probe to the first few atomic layers of the surface. Electrons moving within a crystal medium are susceptible to both elastic and inelastic scattering via numerous mechanisms, leading to an energy-dependent attenuation length. By examining the electron attenuation length for various energies and in various materials, the relationship shown in Figure 2.4 can be created. The electron energies typically used for LEED range between 50-200 eV, at which the escape depth of electrons is approximately 6 Å [14]. For comparison, the spacing between Ti planes at the rutile TiO_2(110) surface is $\sim$3.6 Å. Resultantly, LEED demonstrates a high degree of surface sensitivity, as the probe electrons travel only a few atomic layers into the crystal, even when the incoming beam is at normal incidence to the surface.

2.4 Auger Electron Spectroscopy

Auger electron spectroscopy (AES) is a widely used technique for determining the chemical composition of surfaces and was discovered independently by Lise Meitner in 1923 [15–17] and Pierre Auger in 1925 [18]. A schematic of the Auger process is shown in Figure 2.5. Firstly, an electron is emitted from an atomic core level following irradiation by an incident electron or photon. This leads to the creation of a hole within the atom or near the surface, followed by autoionisation, in which the vacancy is filled by an electron transition from a level closer to the Fermi level (E_F). As a result there is an available quantum of energy, with a magnitude given by the difference in binding energies between the core hole and the elec-

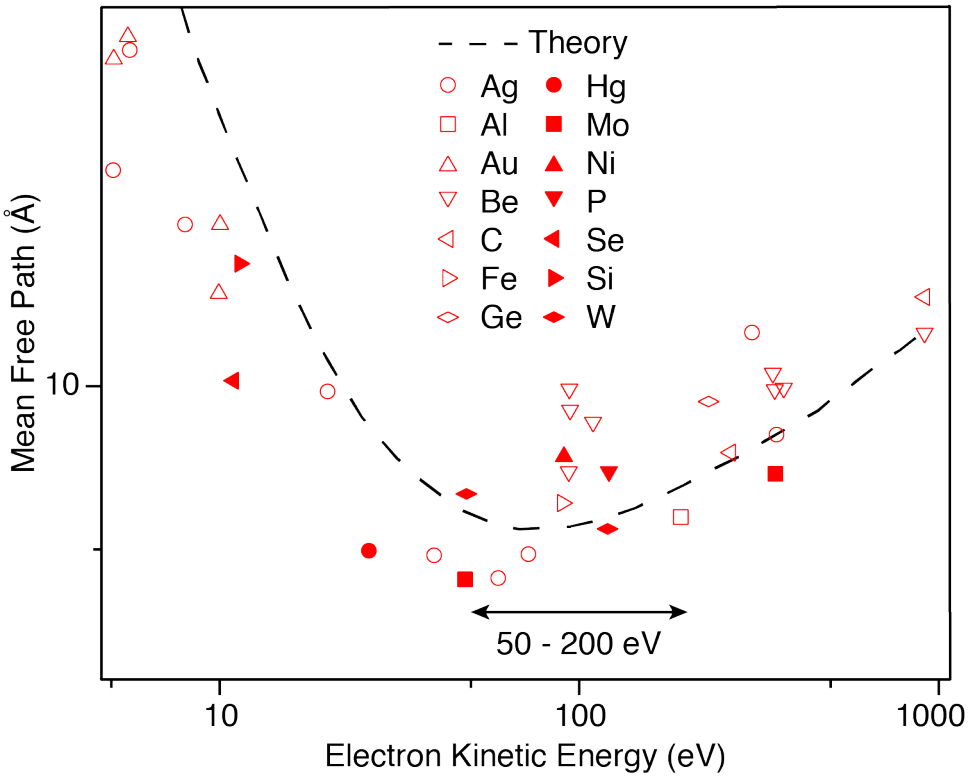

Figure 2.4: A plot of electron mean free path in various materials versus electron kinetic energy along with values calculated from theory (dashed line). This illustrates the inherent surface sensitivity of electrons with energies in the range 50-200 eV used in LEED. Adapted from data in [14].

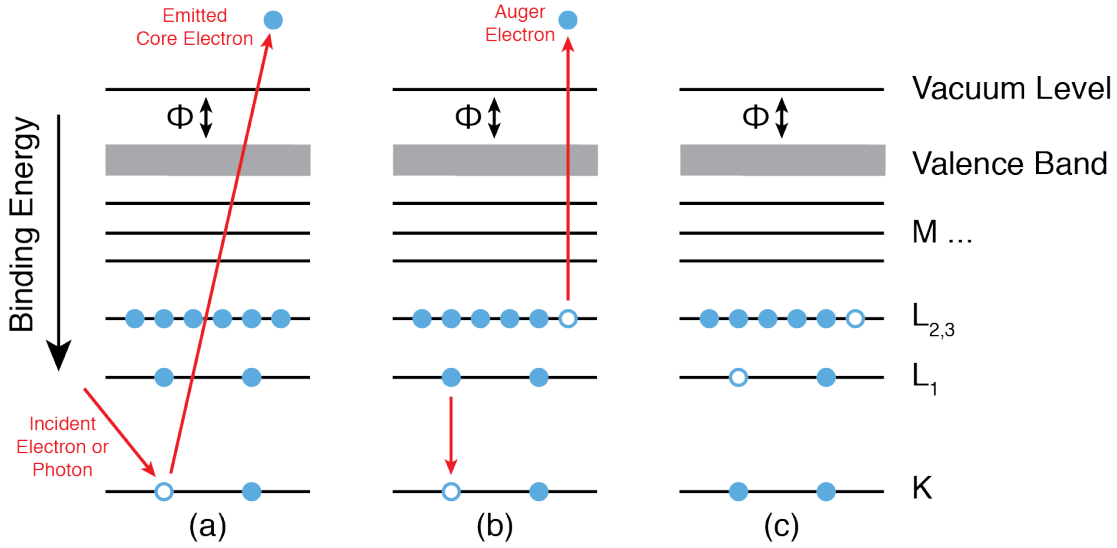

Figure 2.5: Schematic of the Auger process, in which the stimulated emission of an atomic core level electron leads to autoionisation and the emission of an Auger electron. The species of the atom can be identified from the energy of this Auger electron.

tron which fills this vacancy. This energy can be released via X-ray fluorescence or by transfer to a third, Auger electron which is excited above the vacuum level and emitted with a kinetic energy (E_{kin}) given by Equation 2.13, in which Φ is the workfunction and E_K, E_{L_1} and $E_{L_{2,3}}$ are the energies of the K, L_1 and $L_{2,3}$ levels, respectively.

$$E_{kin} = E_K - E_{L_1} - E_{L_{2,3}} - \Phi. \tag{2.13}$$

The emitted Auger electron possesses an element-specific energy, which allows chemical identification of atoms at the surface or near-surface region. AES employs electrons with energies of a few hundred eV which, although greater than those typically used in LEED, allow a good degree of surface sensitivity. Measuring Auger spectra in the kinetic energy range of $\sim$0-2 keV allows the identification of any element possessing three or more electrons. Peaks in Auger spectra are identified by letters corresponding to the energy levels of the three electrons involved in the Auger process. This nomenclature is dictated by the quantum number of the electron (n), such that K describes $n = 1$, L describes $n = 2$ and so on. For example, the Auger process shown in Figure 2.5 is denoted as $KL_1L_{2,3}$.

References

[1] R. W. Boyd, *Nonlinear Optics*. Elsevier, 2008.

[2] R. T. Chapman, *Building a Laboratory based XUV Microscope*. PhD thesis, University of Southampton, 2012.

[3] I. Shchatsinin, *Free clusters and free molecules in strong, shaped laser fields*. PhD thesis, Freie Universität Berlin, 2009.

[4] L. Schiff, *Quantum Mechanics*. McGraw-Hill, 1968.

[5] V. E. Henrich, "The surfaces of metal oxides," *Reports on Progress in Physics*, vol. 48, no. 11, pp. 1481–1541, 1985.

[6] H. Ueba and B. Gumhalter, "Theory of two-photon photoemission spectroscopy of surfaces," *Progress in Surface Science*, vol. 82, no. 4-6, pp. 193–223, 2007.

[7] K.-I. Shudo and T. Munakata, "Resonant photoexcitation of Si(001) measured with two-photon photoemission spectroscopy," *Physical Review B*, vol. 63, no. 12, p. 125324, 2001.

[8] K.-I. Shudo, S. Takeda, and T. Munakata, "Resonant surface-state transitions of Si(111)-7$\times$7 measured with two-photon photoemission spectroscopy," *Physical Review B*, vol. 65, no. 7, p. 075302, 2002.

[9] W. Wallauer and T. Fauster, "Two-photon excitation processes and linewidths of surface and image states on Cu(111)," *Surface Science*, vol. 374, no. 1-3, pp. 44–50, 1997.

[10] C. Davidson and L. Gemer, "Diffraction of Electrons by a Crystal of Nickel," *Physical Review*, vol. 30, pp. 705–740, 1927.

[11] G. P. Thomson, "Experiments on the Diffraction of Cathode Rays," *Proceedings of the Royal Society London A*, vol. 117, no. 778, pp. 600–609, 1928.

[12] G. P. Thomson, “The Analysis of Surface Layers by Electron Diffraction,” *Proceedings of the Royal Society London A*, vol. 128, no. 808, pp. 649–661, 1930.

[13] G. P. Thomson, “The Diffraction of Electrons by Single Crystals,” *Proceedings of the Royal Society London A*, vol. 133, no. 821, pp. 1–25, 1931.

[14] A. Zangwill, *Physics at Surfaces*. Cambridge University Press, 1988.

[15] L. Z. Meitner, “On the formation of the β-ray spectra of radioactive substances,” *Physik*, vol. 9, no. 1, pp. 131–144, 1922.

[16] L. Z. Meitner, “The β-ray spectrum of UX_1 and its interpretation,” *Physik*, vol. 17, no. 1, pp. 54–66, 1923.

[17] L. Z. Meitner, “On a possible interpretation of the continuous β-ray spectrum,” *Physik*, vol. 19, no. 1, pp. 307–312, 1923.

[18] P. Auger, “Sur les rayons β secondaires produits dans un gaz par des rayons X,” *Comptes Rendus de l’Acadmie des Sciences*, vol. 177, pp. 169–171, 1923.

Chapter 3

Instrumentation

Abstract

The ability of experimental science to realise reliable and accurate results is facilitated by the quality of the instrumentation. In this chapter, considerations for the practical implementation of the experimental techniques used in this study are described. These techniques include various photoemission spectroscopies, as well as additional techniques for sample preparation and characterisation. These techniques are executed in ultra-high vacuum systems which are themselves also described.

3.1 The UHV Systems

The requirement for ultra-high vacuum (UHV) environments in surface science studies is illustrated by a simplified example. Consider the adsorption of gas-phase molecules on a surface consisting of 10^{19} atoms m^{-2}. Assuming a unity sticking coefficient, the time required to attain monolayer coverage (ML) at a pressure of 10^{-10} mbar is $\sim$10 hours. Accordingly, UHV conditions, which typically refers to pressures in the region of 10^{-10} mbar, are vital for controlled and reliable studies of surfaces. Additionally, surface science techniques such as electron spectroscopy can only be operated under UHV conditions due to the limited mean free path of electrons between collisions with gas phase molecules. Achieving such clean, low pressure environments presents a considerable practical challenge and so requires the employment of specialised equipment which is described subsequently.

The majority of the work described in this thesis was undertaken at UCL using the vacuum chamber described in Section 3.1.1. The work in Chapter 6 employed the condensed matter end-station at the Artemis facility of the Rutherford Appleton Laboratory (RAL), which is described in Section 3.1.2. In both systems, a series of vacuum pumps is used to achieve increasingly low pressures. Turbomolecular (kinetic) pumps are backed by rotary (positive displacement) pumps and are responsible for removing the high quantity of gas present when bringing the vacuum system down from atmospheric pressure. A chilled water system present in the laboratories facilitates the cooling of turbo-pumps, as well as the X-ray light source at UCL.

In order to make the transition between high vacuum and UHV conditions it is necessary to bake the vacuum system for $\sim$48 hours at about 400 K to desorb molecules such as water and hydrocarbons from inner surfaces of the system. Following baking, ion getter and titanium sublimation pumps are used to achieve UHV conditions. On both the UCL and RAL systems, gas lines allow the introduction of high purity gases via high precision leak valves. Turbo-pumps recover UHV conditions following operations such as sputtering and dosing of gas phase molecules, during which the pressure inside the system may rise towards 10^{-6} mbar. The pressure of residual gases present under UHV conditions are monitored using Bayard-Alpert type hot-cathode ionisation gauges, which allow measurements in the range 10^{-4} mbar to 10^{-11} mbar. Higher pressure areas, such as in the backing lines of the turbo-pumps, are monitored using Pirani gauges which

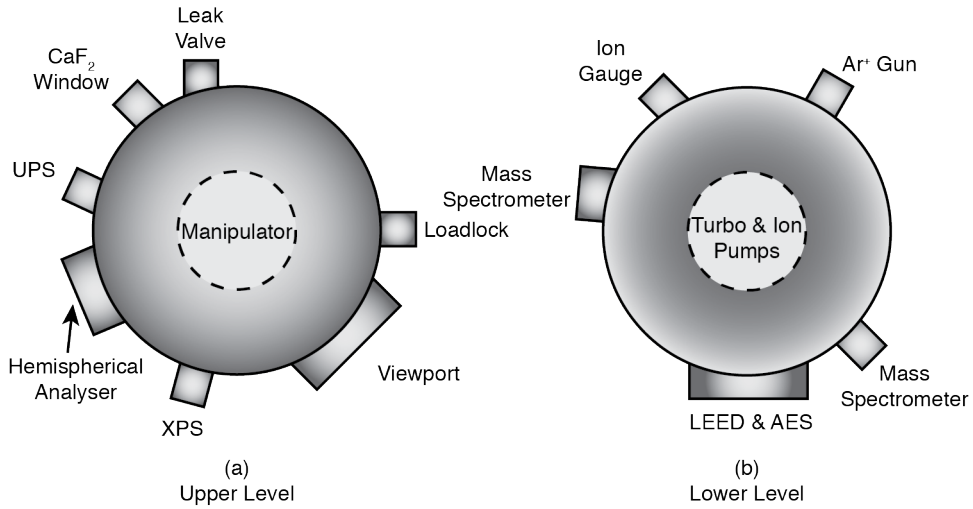

Figure 3.1: Schematic of the ultra-high vacuum chamber at UCL. (a) The upper level of the chamber contains instrumentation for photoemission studies, such as the hemispherical analyser and X-ray and UV light sources. The manipulator at the top of the chamber is capable of moving in three dimensions. (b) The lower level of the chamber contains optics for LEED and AES, two mass spectrometers, the ion gauge and Ar^+ sputtering gun. A flange at the base of the chamber leads to two independent gates valves, behind which are a large turbo-pump and an ion pump.

operate at pressures of 10^{-2} mbar and above.

3.1.1 UCL UHV System

The UHV system at UCL consists of a single mu-metal chamber, equipped with ultra-violet (*UPS, VG Microtech*) and X-ray (*XR3HP, VG Microtech*) light sources, quadrupole mass spectrometers (*HAL 100 & 101, Hiden Analytical*), LEED and AES optics (*ErLEED RFA, Specs*), a sputtering gun, an ion gauge and a hemispherical electron energy analyser (*R3000, VG Scienta*). The arrangement of these facilities is shown schematically in Figure 3.1. For ultra-fast photoemission experiments, the laser beam is focused by a biconvex lens through a CaF_2 window, which was chosen not only as it transmits in the ultra-violet (UV) region but is also sufficiently thin so as to limit dispersion, and therefore temporal broadening, of the fs laser pulse. The laser beam was incident upon the sample at an angle of $(68 \pm 1)^\circ$ to the sample surface normal and photoelectrons were collected by the hemispherical analyser, which was normal to the sample surface.

Sample preparation consisted of cycles of Ar^+ sputtering and thermal annealing

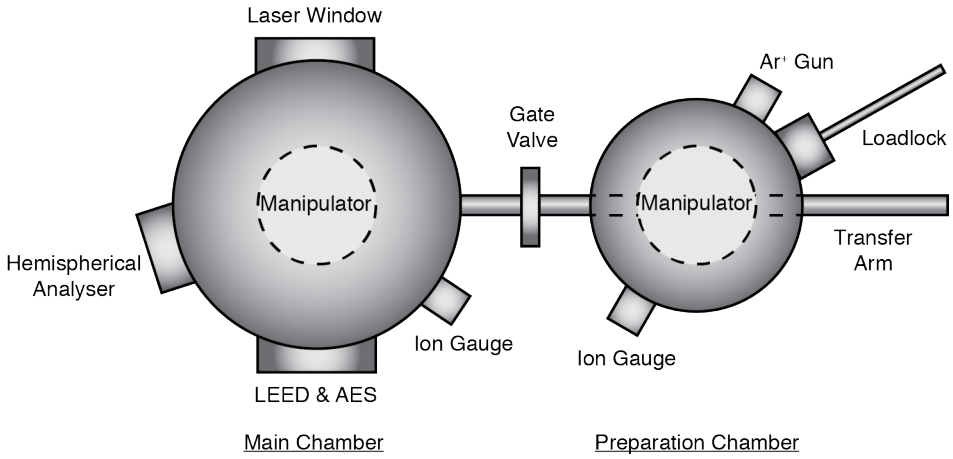

Figure 3.2: Schematic of the ultra-high vacuum chamber at RAL. Ar^+ sputtering took place in the preparation chamber before the sample was transferred to the main chamber via the transfer arm. The main chamber is pumped by turbo and ion pumps to a base pressure of 2×10^{-10} mbar.

to ~ 1000 K via bombardment of the back of the sample plate with high energy (~ 1 keV) electrons. The sample cleanliness was verified via AES and/or XPS and long-range order was verified using LEED. The proportions and species of residual gases in the UHV chamber were monitored via mass spectrometry, and the base pressure of the chamber was typically 2×10^{-10} mbar.

3.1.2 RAL UHV System

The RAL UHV system consists of two adjoining mu-metal chambers, which may be isolated by closing a gate valve. The experimental chamber, shown schematically in Figure 3.2, operates at a base pressure of 2×10^{-10} mbar and is equipped with LEED and AES optics (*ErLEED RFA, Specs*) and a hemispherical electron energy analyser (*Phoibos 100, SPECS*). The energy resolution of the spectra recorded by the hemispherical analyser is limited by the bandwidth of the XUV laser, which is typically 130 meV for a 30 fs pulse duration.

The isolated preparation chamber allows high pressure procedures such as Ar^+ sputtering to be undertaken without contaminating the main experimental chamber. The sample was inserted into the preparation chamber via a fast entry loadlock system. Sample preparation consisting of Ar^+ sputtering and thermal annealing to $\sim$1000 K was undertaken in the preparation chamber, before a transfer arm was used to move the prepared sample to the experimental chamber.

3.2 The Laser Systems

3.2.1 UCL Laser System

The femtosecond laser system at UCL consisted of a series of commercial optical set-ups, which, combined, could produce 0.47-6.0 eV laser pulses with sub-100 fs duration. A schematic of this system is shown in Figure 3.3. The broadband 80 MHz Ti:Sapphire oscillator (*Coherent Micra*) was pumped by 5 W of 532 nm light supplied by a continuous wave (CW) Nd:YLF laser (*Coherent Verdi*). The Ti:Sapphire oscillator produced $\sim$100 fs laser pulses with a central wavelength around 800 nm and an average power of $\sim$350 mW once mode-locked.

The oscillator was used to seed a 1 kHz regenerative amplification cavity (*Coherent Legend*) which produced 2-2.4 W of 800 nm light. The amplifier was pumped by a nanosecond Nd:YLF laser (*Coherent Evolution 30*), which produced 30 W at 527 nm. Beamsplitters were used to guide fractions of the amplifier output into two tuneable OPAs (*Coherent TOPAS*) ($\sim$0.7 W per OPA) and frequency doubling boxes. Combined, the frequency doubling boxes are capable of providing harmonics of the IR beam, resulting in 3 eV (400 nm), 4.66 eV (266 nm) and 6 eV (200 nm) photons. The tuneable OPAs are capable of generating light with a continuously variable energy between 5.25 eV and 0.47 eV (236 nm and 2630 nm, respectively). Although each energy range within the OPA's operation had a specified linear polarisation, this could be altered from parallel (*p*) to the plane of incidence to perpendicular (*s*), or vice versa, by placing a periscope in the beamline after the OPA.

A pair of fused silica prisms was employed to introduce negative chirp to the output of the OPAs and so obtain the shortest possible pulse duration. The ability of this set-up to minimise dispersion of the laser pulse depends upon the refractive index of the prism material, the distance between the two prisms and the path length of the laser beam inside the prism. Large alterations in the amount of negative dispersion introduced by the prism pair were made by altering the inter-prism distance, while fine tuning was achieved by tuning the path length of the laser beam through one of the prisms. Subsequently, a beamsplitter could be introduced into the optical path to split the beam into two identical pulses for TR-2PPE experiments. A piezo-electric delay stage was used to introduce a variable time delay between the pump and probe pulses before these beams were recom-

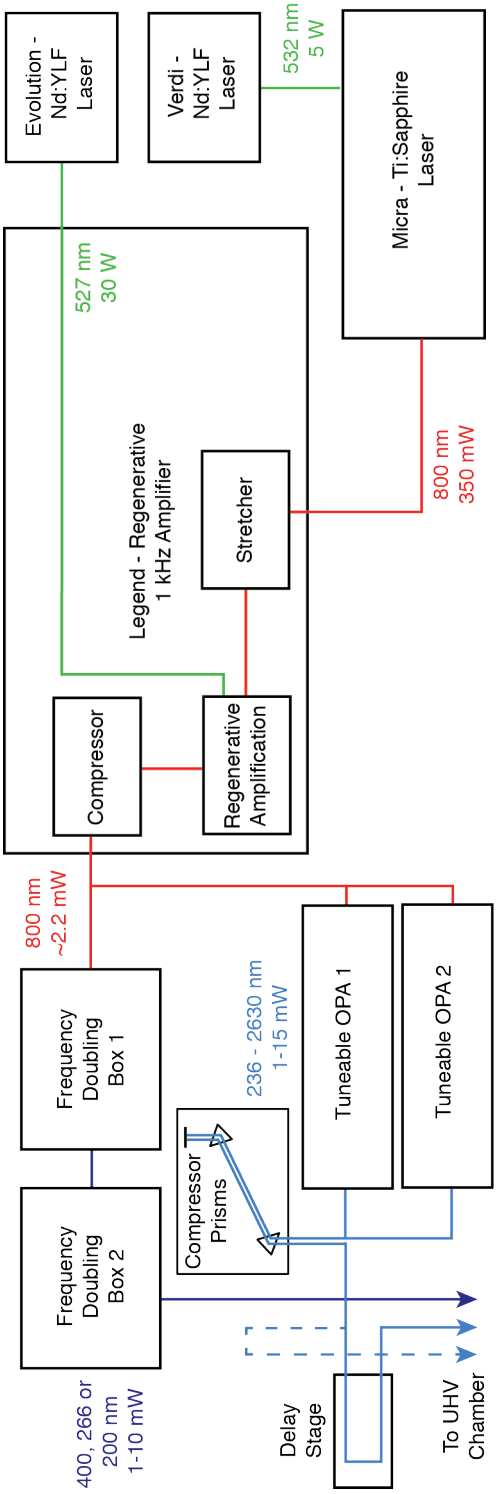

Figure 3.3: Schematic of the laser system at UCL. A Ti:Sapphire laser provides 80 MHz, 800 nm light with an average power of 350 mW. This light is amplified by a 1 kHz regenerative amplifier, which outputs 2-2.4 W at 800 nm. Subsequently, the infra-red light is fed into systems for higher harmonic generation or frequency mixing. The outputs of the tuneable OPAs are compressed temporally by a pair of prisms to obtain the shortest possible pulse duration. Finally, a variable delay stage allows a time delay to be introduced between pulses, which is required for time-resolved photoemission measurements.

bined. Finally, the laser beam was focused by a plano-convex spherical lens and guided into the UHV chamber through a thin CaF_2 window.

3.2.2 RAL Laser System

The beamline at the Artemis facility of the Rutherford Appleton Laboratory consists of two main components, as shown in Figure 3.4. The first provides tuneable pulses in the region of 235 nm to 15 microns whilst the second generates much higher energy photons, in an energy regime known as extreme ultra-violet (XUV). As the temporal profile for both these energy ranges is sub-100 fs, the facility provides an excellent opportunity for time-resolved studies of core and valence band levels following photoexcitation.

A Ti:Sapphire laser (*RedDragon Komodo KMLabs*) is fed into a two-stage 1 kHz amplification system (*RedDragon KMLabs*), providing $>$13 W of 30 fs long pulses with a central wavelength of 780 nm. A beamsplitter was used to divide this output into two components, which are fed into OPAs or the XUV generation chamber. Tuneable pulses in the UV to infra-red (IR) spectral regions are provided by a high energy tuneable OPA (*HE-TOPAS Light Conversion*). A delay stage provides a variable time delay between the OPA output and the XUV pulse, allowing time-resolved studies to be undertaken. The remaining IR beam from the amplifier enters the XUV generation chamber and a gas-phase medium (Ar or Ne) is used for higher harmonic generation via non-linear optical processes. The XUV light generated maintains the properties of the pump laser for both temporal and spatial coherence. Four interchangeable diffraction gratings cover two spectral ranges, 12-30 nm and 30-90 nm, allowing isolated harmonics to be selected with energies up to $\sim$80 eV. A motorised mirror was used to achieve spatial overlap of the two pulses at the sample surface.

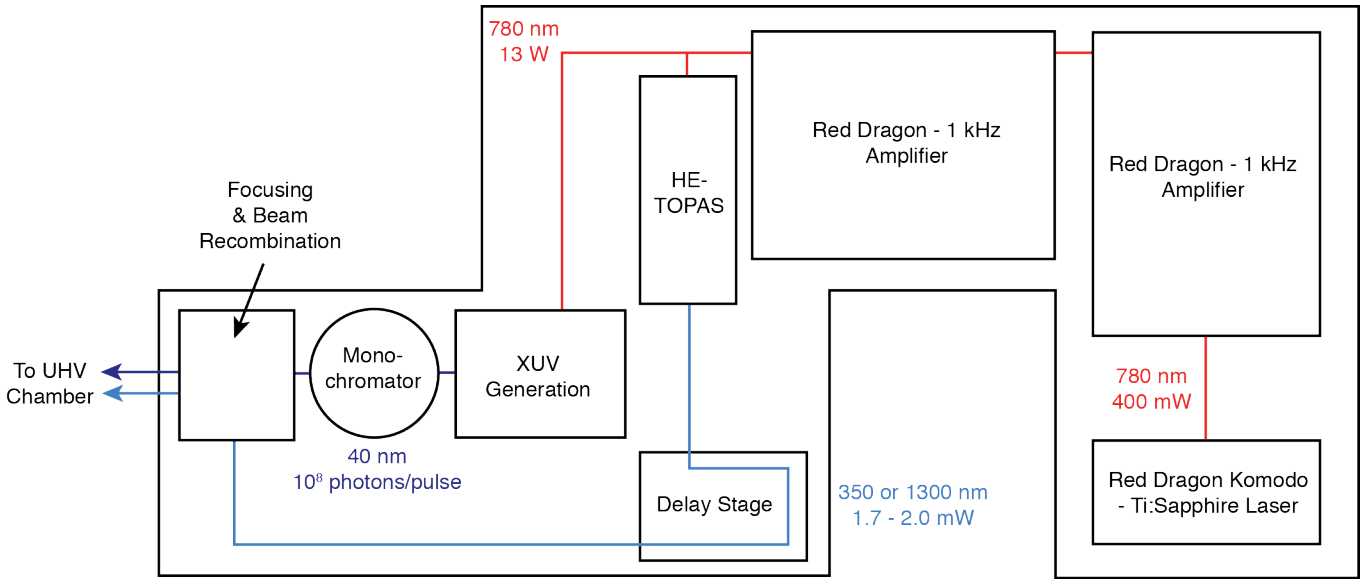

Figure 3.4: Schematic of the laser system at RAL. A Ti:Sapphire laser is amplified by a two-stage 1 kHz Red Dragon amplifier to a power of 13 W, centred at 780 nm. Subsequently, the infra-red light is split and fed into a high energy tuneable OPA or the XUV generation line. The OPA output enters the UHV chamber via a delay stage, introducing femtosecond delays between the pump and XUV probe pulses. The XUV line consists of a chamber for high harmonic generation in a gas-phase medium, a monochromator and a focussing system, which also recombines the pump and probe pulses.

3.3 Sample Preparation

3.3.1 Argon Ion Bombardment

Bombarding a sample with ions of inert gas molecules is a common method of removing surface contaminants [1, 2]. This process, also known as sputtering, employs an ion gun to form a Gaussian beam of ions which is incident upon the sample at a variable angle. The location of the ion gun (*IQE 11 Specs*) is shown in Figure 3.1 & 3.2 and the sample is rotated such that the ion beam is incident at an angle of 45° to the surface normal. The small angle between the ion beam and the surface allows the sample to be cleaned without embedding an undesirably large number of Ar atoms in the surface. The ion gun is attached to a gas line, which provides a source of laboratory-grade pure argon gas.

The ion gun contains a hot filament which emits electrons that are then accelerated towards a high voltage grid. The grid is positively biased with a voltage of 1 kV and the acceleration of the electrons towards this grid provides sufficient energy for them to ionise the argon atoms upon collision, forming an Ar^{+} ion plasma. The Ar^{+} ions are accelerated towards the grounded sample by the electric field created by the positively biased, high voltage grid. The accelerated ions subsequently pass through focussing elements, resulting in an ion beam with energies between 200-5000 eV. Upon impact, this kinetic energy is transferred to atoms at the sample surface, removing them and producing a roughened surface. The rate of ion bombardment is measured from the sample drain current, typically of the order of 1 μA, and can be controlled by altering the emission current.

3.3.2 Sample Heating & Manipulation

The single crystal samples studied at UCL were mounted on polycrystalline Ta sample plates and fixed by spot-welding strips of Ta foil over the edges of the sample as shown in Figure 3.5a. At RAL, a Ta sample plate was also used but the sample was fixed beneath a Ta plate using four Ta screws. The Ta plate had a circular cut-out region which provided access to the sample, as shown in 3.5b. Mounted samples were introduced to the vacuum system via a fast entry loadlock using a magnetic transfer arm. Inside the UHV chamber, the sample was placed

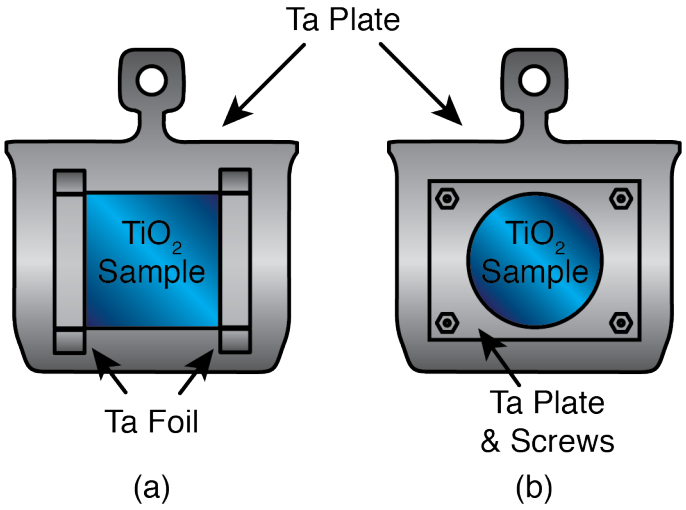

Figure 3.5: Schematic depictions of samples mounted at (a) UCL and (b) RAL.

in a precision manipulator (*Omniax Translator Vacuum Generators*) which allows x,y and z translational movement and 360° rotation.

Heating of the sample was required in sample preparation to reconstruct the surface following roughening by Ar^+ bombardment. Heating is achieved by electron bombardment of the back of the sample plate. Electrons are emitted from a hot filament and accelerate towards the sample plate, which is positively biased by 1 kV. The heating power is controlled by altering the electron flux, which depends upon the sample plate bias and filament current. The sample temperature is monitored using a K-type thermocouple, located ∼5 mm from the sample, or a pyrometer. Thermal annealing temperatures typically ranged between 950 K to 1000 K depending on the specific sample.

3.3.3 Dosing of Gas Phase Molecules

Dosing of gas phase molecules at UCL employed a high precision leak valve, shown in Figure 3.1. Although the residual pressure of water vapour in the UHV chamber is sufficient to hydroxylate reduced TiO_2 surfaces, deliberate dosing of water vapour was desired for some experiments. Deionised water in a glass vial was attached to the UHV system via a conflat flange and could be pumped by a rotary pump. The water was cleaned by repeated freeze-pump-thaw cycles to remove dissolved gases, and its cleanliness verified by quadrupole mass spectrometry. The same gas line could also be used to dose other gases, such as oxygen, into the UHV chamber. The pressure of dosed gases was measured

inside the UHV chamber using an ion gauge or mass spectrometer.

3.3.4 Electron Bombardment

As with Ar^+ bombardment, electron bombardment may stimulate the ejection of atoms from the sample surface. Hence, this procedure was used experimentally to locally alter the surface structure. Initial attempts at electron bombardment utilised the filament employed for thermal annealing of the sample, however, this led to an undersirably high pressure in the UHV chamber. Instead, the experiments described in this work exploit the LEED/AES optics (described in Section 3.4.3) as a focused source of electrons with tuneable energy.

By tuning the voltages applied to the electron lenses of the LEED/AES optics the spatial profile of the electron beam could be controlled. At energies above $\sim$500 eV, electrons incident at TiO_2 surfaces stimulate luminescence in the visible spectral region [3, 4]. Using this phenomenon, the size and position of the electron beam could be determined. Additionally, the measured sample drain current could be used to determine the diameter of the electron beam. The current density was estimated from the beam diameter and sample drain current to be 13 μA mm^{-2} for 500-550 eV electrons.

3.4 Ancillary Techniques

3.4.1 X-ray Source

Core level spectroscopy provides chemically sensitive information about the sample and was used in this work to verify its cleanliness and degree of reduction. XPS measurements employed a commercial X-ray source (*XR3HP VG Microtech*), the design of which is shown schematically in Figure 3.6. A high voltage (typically $\sim$10 kV) is applied across two magnesium coated anodes. Applying this high bias voltage leads to the emission of electrons from the grounded filaments. These electrons bombard the Mg anode face, on which X-rays with an energy of 1253.6 eV (Mg Kα) are produced.

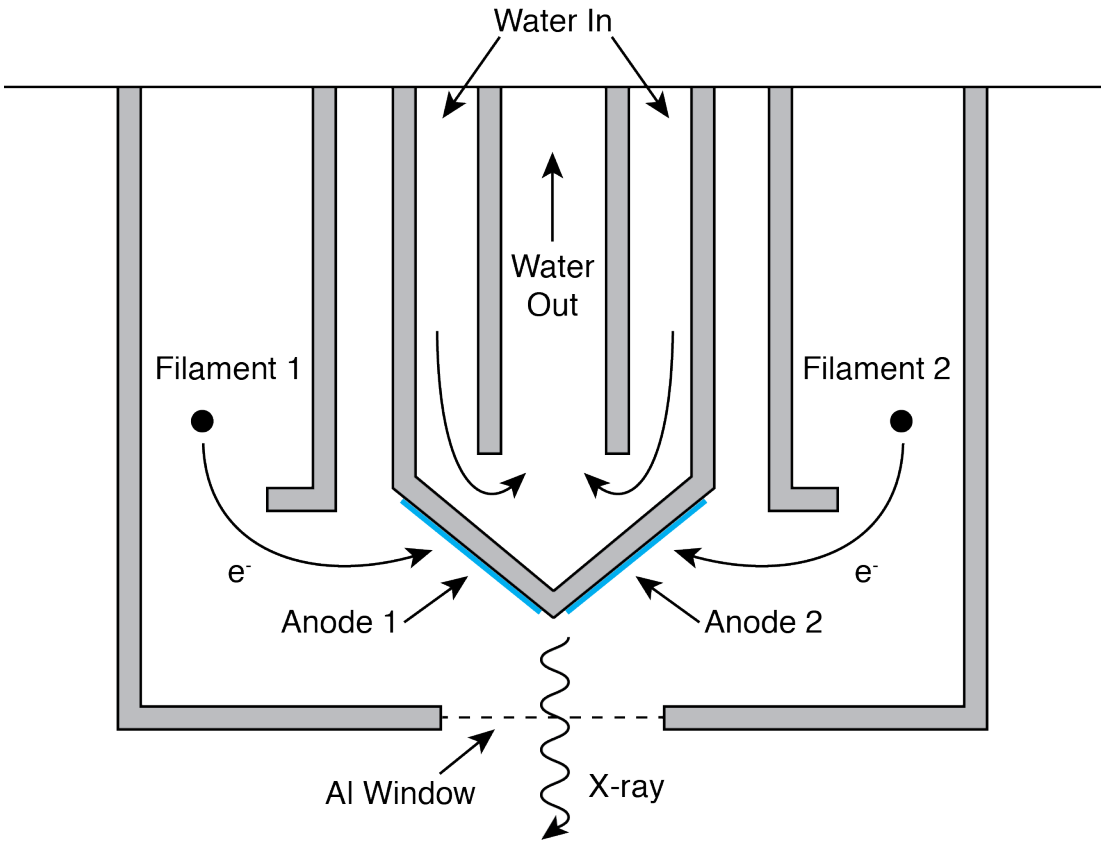

Figure 3.6: Schematic of the X-ray source at UCL. The two anodes (blue) are made of magnesium. Adapted from [5].

Subsequently, the X-rays travel through an aperture in the shielding, which is covered in a sheet of Al foil. The Al foil screens the sample from stray electrons and isolates it from heating effects and contaminants present in the X-ray source, without significantly attenuating the photon flux. The anodes are cooled by a supply of chilled water to prevent overheating of the X-ray source.

3.4.2 Ultra-violet Light Source

A commercial UV light source (*UPS, VG Microtech*) was used to acquire UPS measurements of the sample valence band and defect states in the band gap. The design of the UV lamp, shown in Figure 3.7, consists of a gas discharge region and a final capillary tube. During operation, high purity noble gas, such as Ar, Ne, He or Xe, is leaked into the discharge region via a high precision leak valve. Applying a high bias voltage across the discharge region stimulates ionisation of the gas atoms in the electric field and the emission of photons at characteristic energies dictated by the gas species used.

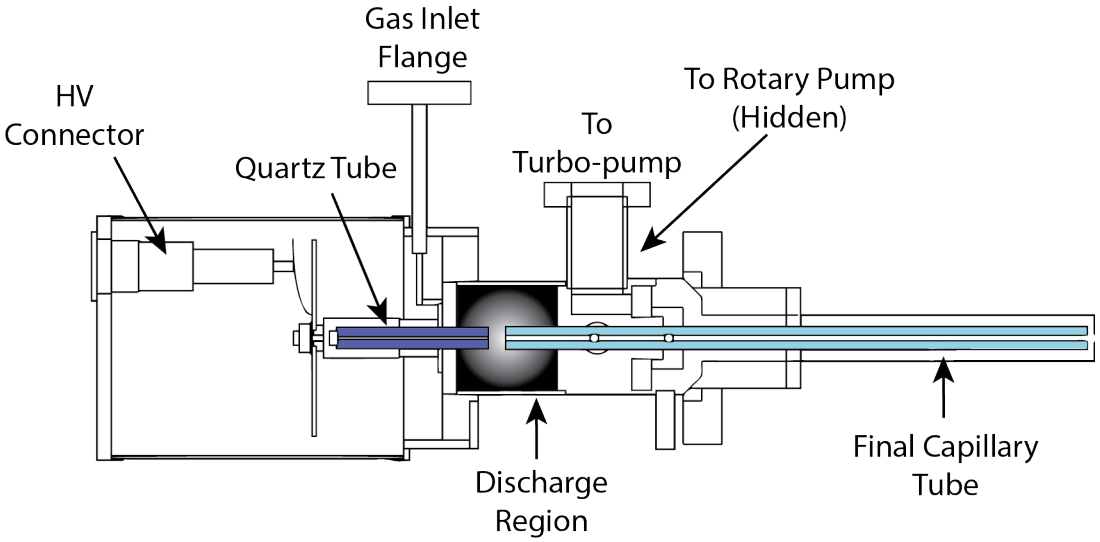

Figure 3.7: Schematic of the UV source at UCL. UV light is generated in the discharge region and is guided through the final capillary tube (light-blue) towards the sample. Adapted from [6].

With the use of He, the UV lamp emits at two main wavelengths. At higher He pressures, the emission is primarily the He I α line at 21.2 eV resulting from singly ionised He atoms. However, at lower He pressures the ratio of double to singly ionised atoms increases and so the He II α emission line at 40.8 eV becomes increasingly significant. The light produced in the discharge region is guided through the capillary tube (diameter $\sim$1 mm) into the UHV chamber where it is incident upon the sample. The UV source is connected to a rotary pump for rough pumping and a turbo-pump for fine pumping, which reduces the pressure rise in the UHV chamber during operation.

3.4.3 LEED & AES Optics

A schematic of the combined system used for LEED and AES measurements (*ErLEED RFA, Specs*) is shown in Figure 3.8a and b, respectively. The instrument comprises of an electron gun, a rear view fluorescent screen and a system suitable for retarding field analysis (RFA). The electron gun is capable of producing a monochromatic beam of electrons with energies ranging between 0-3000 eV. However, for the acquisition of LEED patterns in this work, an electron energy of 75-150 eV was used to minimise electron-induced changes of the sample surface.

In LEED mode, electrons diffracted by the sample travel through the four grids

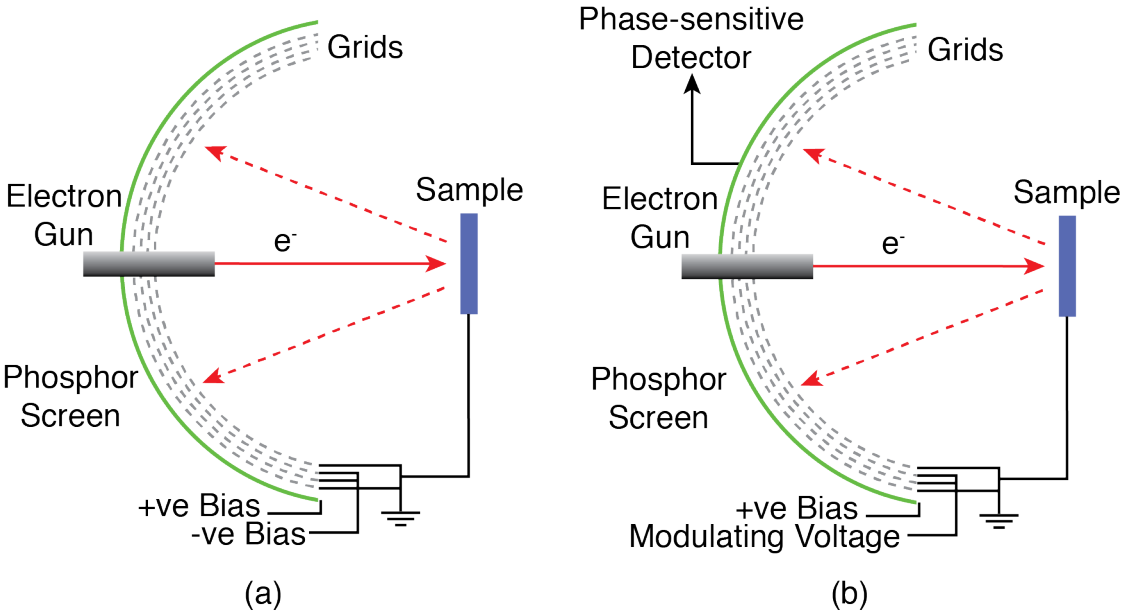

Figure 3.8: Schematic of the LEED (a) and AES (b) optics used at UCL and RAL.

towards a fluorescent phosphor screen. The external pair of grids is earthed to provide a "field free region" through which the scattered electrons travel. A negative bias is applied to the internal pair of grids, forming an electric field that ensures that only elastically scattered electrons are able to proceed towards the phosphor screen, which is itself held at a floating bias of 6 kV. Electrons incident upon the phosphor screen cause bright spots on a dark background and the resulting diffraction pattern is recorded using a digital camera.

Operating in RFA mode, Auger spectra could also be recorded with this instrument. A modulating voltage is applied to the internal grids shown in Figure 3.8 and a lock-in amplifier allows phase-sensitive detection, which is required to record Auger spectra in derivative mode.

3.4.4 Quadrupole Mass Spectrometer

Commercial quadrupole mass spectrometers (QMS) (*HAL 100 & 101, Hiden Analytical*) were employed to verify the species and partial pressures of residual gases under UHV conditions. Additionally, the QMS was used to check the purity of gases such as argon, oxygen and water vapour which were deliberately leaked into the UHV system. Analysis of residual gas in the UHV systems typically revealed a combination of H_2 (m/z = 2), C (12), H_2O (18), CO and N_2 (28) and CO_2

(44).

References

[1] D. Woodruff and T. Delchar, *Modern Techniques of Surface Science*. Cambridge University Press, 1994.

[2] J. Venables, *Introduction to Surface and Thin Film Processes*. Cambridge University Press, 2000.

[3] I. Fernández, A. Cremades, and J. Piqueras, "Cathodoluminescence study of defects in deformed (110) and (100) surfaces of TiO_2 single crystals," *Semiconductor Science and Technology*, vol. 20, no. 2, pp. 239–243, 2005.

[4] M. M. Mikhailov and S. A. Yuryev, "Cathodoluminescence of TiO_2 powders," *Inorganic Materials: Applied Research*, vol. 5, no. 5, pp. 462–466, 2014.

[5] D. Briggs and M. Seah, *Practical Surface Analysis*, vol. 1. John Wiley and Sons Ltd, 1990.

[6] V. Microtech, *Ultraviolet Sources Operating Manual*. VG Microtech, 1999.

Chapter 4

Resonant Photoexcitation at Rutile TiO_2(110) Surfaces

Abstract

Excited electrons and holes facilitate redox reactions at metal oxide surfaces. However, precise details of the charge transfer process remain unclear. This chapter presents two-photon (2PPE, $h\nu$ = 3.10-4.09 eV) and ultra-violet (UPS, $h\nu$ = 21.2 eV and 40.8 eV) photoemission spectra measured from the reduced, hydroxylated and water-covered rutile TiO_2(110) surfaces. 2PPE spectra evidence resonant enhancement, which is attributed to photoexcitation from the Ti 3d band gap states to unoccupied conduction band levels of predominantly t_{2g} or e_g symmetry, centred (2.73 $\pm$ 0.03) eV above the Fermi level (E_F). The lifetime of the excited state is estimated to be $\leq$14 fs. The 2PPE resonance, though present at surfaces containing oxygen vacancies, increases in intensity following the adsorption of bridging hydroxyl groups. Further enhancement at the water-covered surface is attributed to the creation of bridging hydroxyls within the monolayer. Finally, water adsorption was found to shift the central energy of the unoccupied state by $\sim$-0.1 eV.

The work presented in this chapter has been published as References [1] and [2].

4.1 Introduction

The rutile TiO_2(110) surface has arguably become the prototypical metal oxide surface. Stoichiometric rutile TiO_2 is an electronic insulator, however, it becomes an n-type semiconductor with an indirect band gap of 3.0 eV following reduction [3]. The conduction band of stoichiometric rutile TiO_2 consists principally of two Ti 3d bands. These bands posess t_{2g}-like symmetry (d_{xy}, d_{yz} and d_{xz} orbitals) close to the Fermi level (E_F) and e_g-like symmetry ($d_{x^2-y^2}$ and d_{z^2} orbitals) at greater energies [4]. Reduction of the TiO_2(110) surface results in a Jahn-Teller distortion and further splitting of the t_{2g}-like levels. Excess electrons present in the crystal lattice following reduction become trapped at Ti sites, filling the lower energy levels of t_{2g} symmetry, and result in occupied polaronic band gap states (BGS) centred $\sim$1 eV below E_F in photoemission measurements [5–7].

Reduction of TiO_2 may be achieved by the creation of intrinsic defects such as oxygen vacancies (O_b-vacs), bridging hydroxyls (OH_b) and Ti interstitial atoms (Ti_{int}), in addition to doping [8]. At the rutile TiO_2(110) surface, excess electrons localise as polarons at Ti sites in a process known as self-trapping [9, 10]. The extent of polaron localisation at the rutile TiO_2(110) surface in theoretical calculations differs between methods [11–13]. Density functional theory (DFT) calculations containing a Hubbard correction term, U, are particularly sensitive since this parameter influences degree of electron localisation. Presently, a consensus on the method for determining an appropriate value of U has not been reached. Subsequently, this parameter varies between works, resulting in differing predictions [12].

OH_b are common surface defects, which may be formed at the TiO_2(110) surface via dissociative adsorption of water at O_b-vacs between about 170 K and 500 K [14]. Hydroxylation does not influence the magnitude or energy of the BGS peak in photoemission measurements [15, 16]. It has been proposed that OH_b formation may still influence the degree of polaron localisation at the surface [17]. However, recent calculations have suggest that the nature of polarons at the TiO_2(110) surface is in fact independent of the donor surface defect [11]. Additionally, experimental works demonstrate similar infra-red absorption spectra independent of the reduction method [18].

Upon chemisorption, the molecular orbitals (MOs) of OH_b can hybridise with the surface electronic structure. This process alters the appearance of photoemission

spectra of the valence band region [16, 19, 20]. In ultra-violet photoemission spectroscopy (UPS) measurements, the adsorption of OH_b results in increased spectral intensity in two regions, centred 10.8-10.2 eV and 8.0-7.6 eV below E_F [16, 19]. MOs are defined under the linear combinations of atomic orbitals (LCAO) approximation [21], according to which the occupied MOs of a hydroxyl group are the 3σ and 1π orbitals. Since the feature $\sim$10.5 eV below E_F lies outside the valence band of TiO_2, it is not expected to hybridise significantly, and so may be associated with the 3σ MO of OH_b. Conversely, a feature $\sim$7.8 eV below E_F may be associated with the 1π MO, although a significant redistribution of these levels is expected upon hybridisation with the Ti 3d orbitals of the substrate [20]. This assignment was originally made in comparison to measurements of the OH^- group of solid NaOH [16, 22]. Additionally, calculations have predicted that OH_b induce new levels in the conduction band region [13].

Once O_b-vacs at the surface are saturated, the majority of studies suggest that water adsorbs molecularly below room temperature [16, 19, 23–26]. Temperature-programmed desorption (TPD) spectra evidence peaks at 270 K, 175 K and 155 K. These features were assigned to desorption of monolayer, bilayer and multi-layer water, respectively. Monolayer water chemisorbs at Ti_{5c} sites and hybridises with the sample's valence band [20], whilst bilayer water physisorbs on the rows of bridging O_{2c} atoms. Only the first layer of water influences the sample work-function. Monolayer water donates electrons to the substrate due to its relative electronegativity, reducing the workfunction value by $\sim$1 eV compared to that of the clean surface [27]. Bilayer water has been shown to slightly alter the structure of the chemisorbed monolayer through the formation of hydrogen bonds (HBs) [14, 28, 29].

Despite the general consensus that water adsorbs molecularly on the defect-free and hydroxylated TiO_2(110) surface, there is increasing evidence for a mono-layer consisting of both water and hydroxyl groups [30–34]. Water dissociation at the defect-free surface results in one OH_b and terminal hydroxyl (OH_t) pair per molecule. In the presence of O_b-vacs, the two possible dissociation pathways compete such that one dissociation event at an O_b-vac substitutes another in a defect-free area. Hence, the total hydroxyl coverage remains roughly constant. It was shown that 40% of the monolayer consists of hydroxyls (OH_b & OH_t), for initial O_b-vac densities of $\leq$0.2 ML [32].

The first two-photon photoemission spectroscopy (2PPE) study of the TiO_2(110) surface was published in 2004, and focused principally on measurements of the

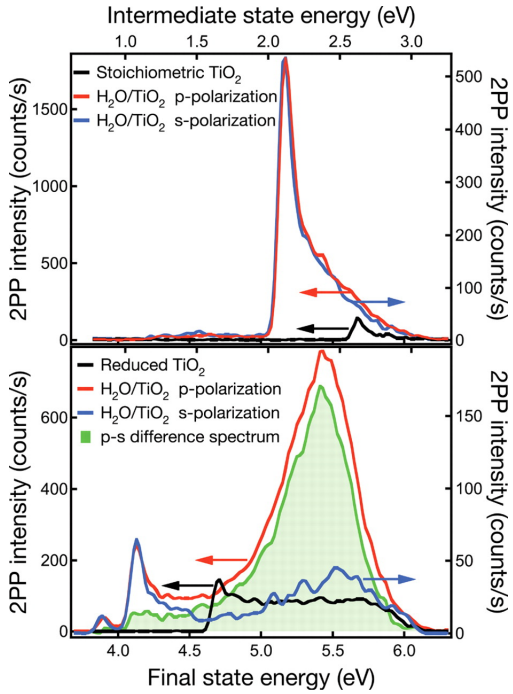

Figure 4.1: 2PPE spectra ($h\nu$ = 3.05 eV) from the stoichiometric and reduced TiO_2(110) surfaces. At the reduced surface, differences between spectra obtained using s- and p-polarised light is attributed to the formation of 'wet electron' states following water adsorption at 100 K. Reproduced from Reference [27].

workfunction following various sample preparations [35]. Additionally, this work presented initial evidence for an unoccupied state 2.4 eV above E_F, following the adsorption of molecular water. The H_2O/TiO_2(110) interface was investigated further in a subsequent 2PPE study, accompanied by DFT calculations. In this work, the 2PPE feature was attributed to resonant photoexcitation from the BGS via an unoccupied state (2.4$\pm$0.1) eV above E_F, which is formed by a network of HBs in the presence of chemisorbed H_2O and OH_b [27]. As the excited electrons populating this state were localised at the surface and partially hydrated by the water molecules, the unoccupied state was named the 'wet-electron' state.

Differences between s- & p-polarised 2PPE spectra, shown in the lower panel of Figure 4.1, suggested that the transition moment of resonant photoexcitation to the 'wet-electron' state was normal to the surface. The resonant feature was also absent in single-photon photoemission (1PPE) measurements, confirming the involvement of an unoccupied intermediate state [27, 35]. The 2PPE signal reached maximum intensity at a coverage of 1 ML water, when using a photon energy of 3.05 eV (407 nm). Additionally, the energy and lifetime of the 'wet-electron' state were suggested to be coverage-dependent. On the 'bare' surface, which was likely hydroxylated, using 3.05 eV photons the 'wet-electron' state was not observed and the laser pulse cross-correlation showed no broadening by an

intermediate state lifetime. DFT calculations predicted that the 'wet-electron' state lies $\sim$4.5 eV above E_F for a coverage of 0.5 ML OH_b and hence could not be populated from the BGS using this photon energy. The addition of 1 ML H_2O was predicted to decrease the energy of the 'wet-electron' state by 2 eV. A 'wet-electron' state lifetime of $\leq$15 fs was suggested for such a surface.

The 2PPE works described above were limited in respect to the available photon energy range and by the absence of chemically sensitive surface science techniques. The fixed 3.05 eV photon energy did not permit the energy distribution of the 2PPE resonance to be mapped, and the spectra displayed space-charge peaks at the workfunction cut-off which can influence the kinetic energy of photoelectrons. Additionally, the intensity of the BGS following reduction and exposure to gas-phase molecules was not monitored.

Subsequent studies revealled similar resonant processes at the TiO_2(110) surface following the adsorption of methanol or ethanol [36–39]. In this case, the 'wet-electron' state was found to lie between 2.2 eV and 2.45 eV above E_F and possess a lifetime of $\sim$24 fs [36]. Due to the dependence of the 2PPE intensity on laser-irradiation time, the 'wet-electron' state was related to the coverage of OH_b, created after photodissociation of the alcohol molecules [36, 39]. Finally, delocalised states 3-3.5 eV above the conduction band minimum of the TiO_2-terminated $SrTiO_3$(100) surface were predicted in DFT calculations, following water adsorption. To the author's knowledge, these solvated states, which were compared to the 'wet-electron' states at the TiO_2(110) surface, have not been verified experimentally.

In this chapter, 2PPE and UPS measurements of the reduced, hydroxylated and water-covered TiO_2(110) surfaces are presented. The photon energy and coverage dependence of the 2PPE resonance is examined, supported by measurements of the occupied density of states.

4.2 Experimental Procedure

A reduced rutile TiO_2(110)(1$\times$1) single crystal sample (*Pi-Kem*) was prepared by cycles of Ar^+ sputtering (1 kV, 1 μA cm^{-2}, 30 minutes) and thermal annealing to 1000 K (10 minutes) in the ultra-high vacuum (UHV) chamber at UCL,

described in Section 3.1.1. Low-energy electron diffraction (LEED) displayed a sharp (1×1) pattern and X-ray photoemission spectra evidenced a contamination level of <0.4%, comprising of C, Ar and F. After annealing, the sample was permitted to cool in the residual vacuum and is expected to hydroxylate with a coverage of 0.1-0.2 ML OH_b [14]. Such a hydroxylated surface will be referred to as *h*-TiO_2(110). The sample temperature was recorded using a K-type thermocouple, located 5 mm from the sample surface, or by a pyrometric reading from the Ta sample plate at very high temperatures (>600 K).

2PPE spectra were recorded using photon energies in the range of 3.10 eV to 4.09 eV (400 nm to 303 nm), with a -6 V bias applied to the sample. All 2PPE spectra were measured using p-polarised light, with the scattering plane perpendicular to the surface [001] azimuth. The laser power was reduced to ∼1 mW using a variable neutral density filter to limit space-charge effects and the spot size at the sample surface was ∼0.5 mm in diameter. The tuneable femtosecond pulses were compressed using a pair of fused silica prisms to a duration of between 80 fs and 95 fs. The pulse duration was determined from the cross-correlation measured from the polycrystalline Ta sample holder, as described later. All photoemission spectra presented in this chapter were recorded at room temperature, unless otherwise stated.

To prepare the water-covered surface, studied in Section 4.3.2, the *h*-TiO_2(110) surface was cooled to ∼100 K before exposure to 1.8 L of water vapour (1 L = 1.33×10^6 mbar.s). Water deliberately dosed into the UHV chamber was purified by repeated freeze-pump-thaw cycles. 2PPE and UPS spectra were recorded as the sample warmed to 290 K, at a rate of ∼1 K/minute. Following this, the sample was heated to a maximum temperature of 330 K. Temperatures below room temperature were subsequently calibrated with reference to the known adsorption behaviour of water on the reduced TiO_2(110) [24] (see Section 4.3.2).

4.3 Results & Discussion

4.3.1 The *h*-TiO_2(110) Surface

2PPE spectra recorded from the *h*-TiO_2(110) surface using photon energies between 3.10 eV to 4.09 eV are presented in Figure 4.2. As seen in Figure 4.2c,

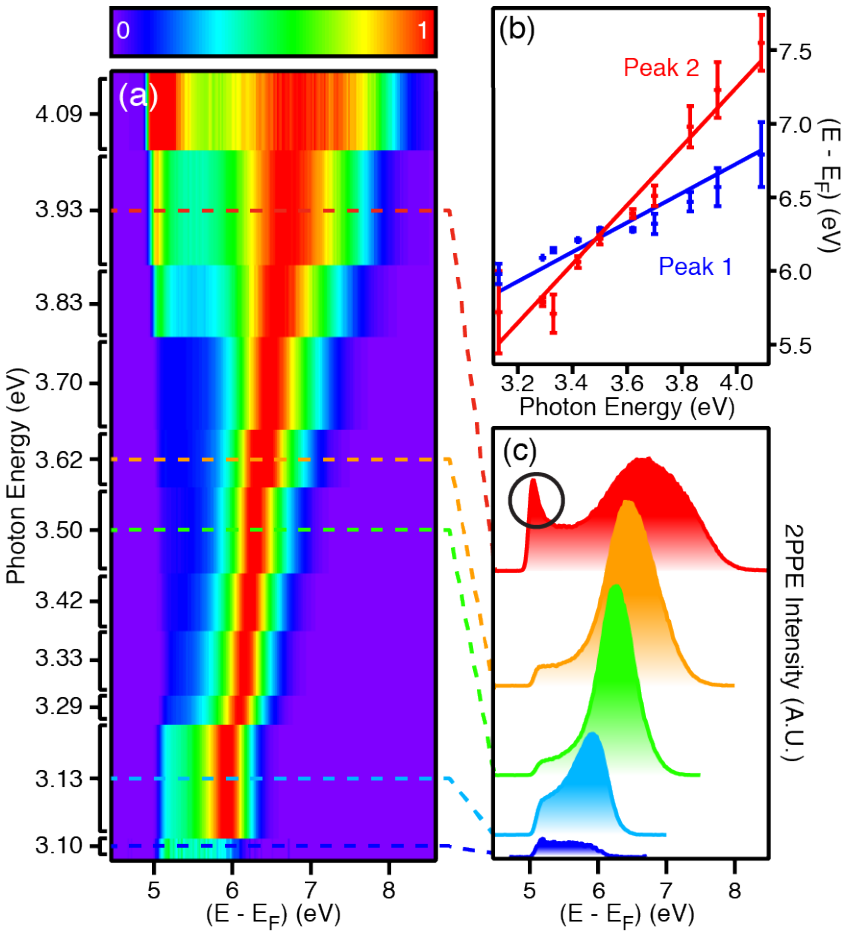

Figure 4.2: 2PPE spectra ($h\nu$ = 3.10-4.09 eV) measured from the *h*-TiO_2(110) surface. (a) Colour map of the 2PPE spectra normalised to the photon flux. (b) Photon energy dependence of the two fitted peaks given by Equations 2.5 (red) and 2.6 (blue). (c) Selected spectra from panel (a) highlighting resonant enhancement of the 2PPE signal. 2PPE from the valence band maximum appears for photon energies above 3.9 eV, shown in a black circle.

the spectrum recorded using 3.10 eV photons (dark-blue) is flat and featureless, similar to that measured at 3.05 eV in Reference [27]. However, increasing the photon energy to 3.13 eV results in the appearance of a peak centred $\sim$6 eV above E_F. This feature becomes more intense with increasing photon energy until about 3.5 eV, after which it again decreases. The photon-energy-dependent intensity of the 2PPE peak is suggestive of resonant photoexcitation processes. At high photon energies, for example 3.93 eV (red), a peak at the workfunction cut-off develops in the spectra, which is highlighted by a black circle. This feature arises principally, not from space-charge effects, but 2PPE from the valence band maximum. 2PPE from the valence band is possible when photon energies above 3.9 eV are used, as this provides sufficient energy to overcome the *h*-TiO_2(110) surface workfunction of $\sim$5 eV.

Subsequent UPS measurements indicated that no molecular water was present at the surface, as expected at room temperature from TPD spectra [40]. On the *h*-TiO_2(110) surface, DFT calculations predict that the 'wet-electron' states lie about 4 eV above E_F [27] and so cannot participate in the resonance observed using 3 eV to 4 eV photons. Hence, the resonance observed on the *h*-TiO_2(110) surface is inconsistent with the 'wet-electron' state interpretation.

The energy of the unoccupied state in the observed resonant photoexcitation process may be determined from the photon energy dependence of the 2PPE spectra. As described in Section 2.2.2, a 2PPE spectrum may be decomposed into two contributions. The first contribution represents purely coherent photoexcitation from the initial state in the excitation process, in this case the BGS, via a virtual intermediate state and is described by Equation 2.5. The second contribution arises from both coherent excitation and incoherent, step-wise photoexcitation via a real unoccupied state. The central energy of this spectral feature is described by Equation 2.6. This implies that non-resonant virtual excitation may contribute to the intensity of the intermediate state peak so long as the ionisation occurs within the electronic dephasing time of the material [41].

Accordingly, the 2PPE spectra in Figure 4.2 were fit with the sum of two Voigt lineshape approximations (the product of Gaussian and Lorentzian peaks with a mixing of 30% and 70%, respectively), in addition to a linear background. An example of the fitting procedure is shown in Figure 4.3, for a spectrum measured using 3.29 eV photons. The positions of the fitted Voigt-like peaks are plotted in Figure 4.2b as a function of photon energy. Linear equations with fixed gradients of one and two for Peaks 1 and 2, respectively, were fit to this data. Hence, Peak 2

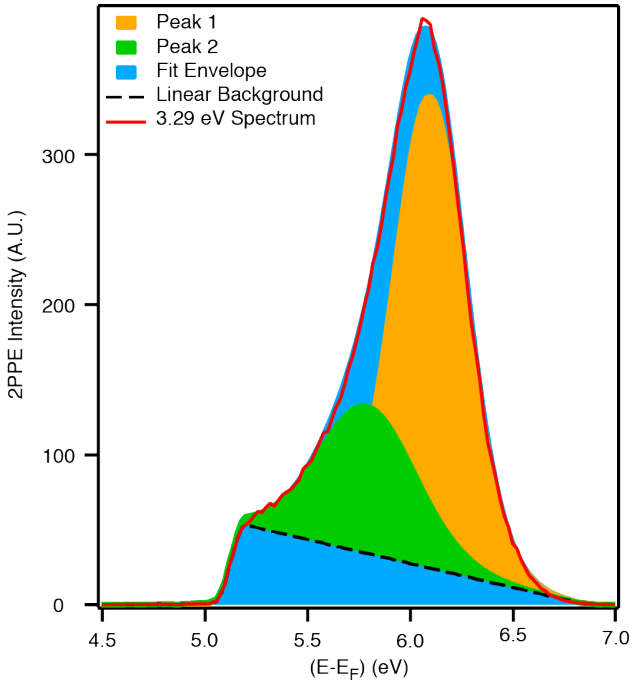

Figure 4.3: 2PPE spectrum ($h\nu$ = 3.29 eV) measured from the *h*-TiO_2(110) surface, illustrating the 2PPE fitting procedure. The spectrum is decomposed into the sum of two Voigt lineshape approximations and a linear background. The continuous red line represents the raw data curve.

is found to result from purely coherent excitation from the BGS while Peak 1 contains information pertaining to the real, unoccupied state. Extrapolating Equations 2.5 & 2.6 to $h\nu$= 0 eV reveals the energies of the states involved in the photoecxitation process. The energy of the initial, occupied state, centred (0.75 $\pm$ 0.04) eV below E_F, is consistent with previous photoemission measurements of the BGS [6, 16, 42–44]. The central energy of the unoccupied state was determined to be (2.73 $\pm$ 0.03) eV above E_F.

To ascertain whether the 2PPE resonance is an innate feature of the reduced TiO_2(110) surface or induced by by adsorbates, the sample was heated above the desorption temperature for OH_b of $\sim$500 K. Accordingly, UPS measurements of the valence band region at this temperature evidenced the extinction of the peak $\sim$10.5 eV below E_F, which is related to the hydroxyl 3σ MO. 2PPE spectra recorded from the reduced surface at $\sim$550 K are shown in Figure 4.4(a). The sample workfunction is $>$5 eV, suggesting an absence of reducing adsorbates. The spectra display resonant enhancement in the absence of OH_b, although it is much less pronounced than that observed at the *h*-TiO_2(110) surface. The photon energy dependence of the resonance at the reduced surface is identical to that at the *h*-TiO_2(110) surface, suggesting that the energy of the unoccupied state remains constant.

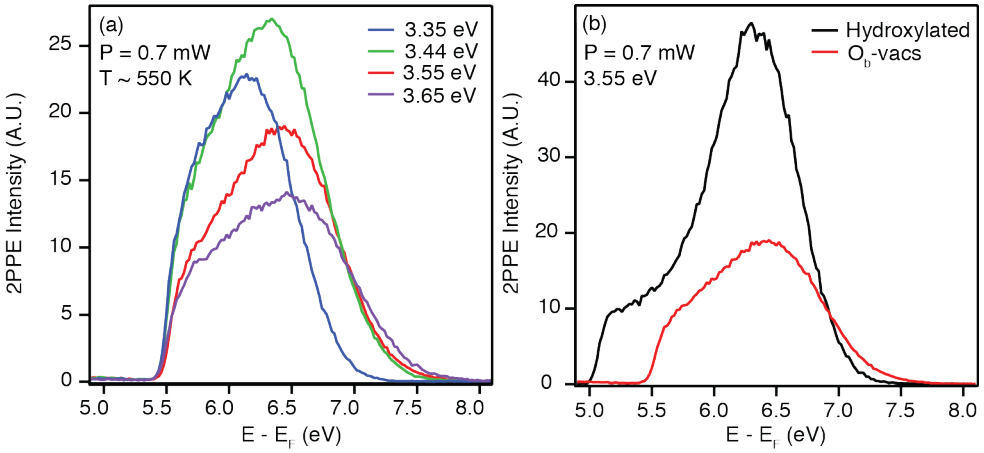

Figure 4.4: 2PPE spectra recorded from the reduced and hydroxylated TiO_2(110) surfaces. (a) 2PPE spectra measured above the desorption temperature of OH_b [40]. Hence the surface is expected to possess O_b-vacs only, which is supported by its high workfunction value. Resonant enhancement is observed, reaching a maximum around 360 nm ($h\nu$ = 3.44 eV). (b) Comparison between 2PPE spectra ($h\nu$ = 3.55 eV, ~350 nm) measured from the reduced (red, ~550 K) and hydroxylated (black, ~300 K) TiO_2(110) surfaces. The presence of OH_b was verified or excluded via UPS He II measurements ($h\nu$ = 40.8 eV). The 2PPE signal is increased by a factor of ~3 on the *h*-TiO_2(110) surface.

In a separate measurement, the effect of hydroxylation on the intensity of the 2PPE resonance was observed directly, as shown in Figure 4.5. The sample was heated to ~540 K and 2PPE spectra were recorded as it cooled using a near-resonant photon energy of 3.44 eV. The high noise level is a result of the limited data acquisition time as the sample cooled. At 536 K, the surface is expected to contain 0.05-0.1 ML O_b-vacs [14] and the 2PPE resonance is weak. As the sample cools, water in the residual vacuum may adsorb dissociatively to form OH_b with a coverage between 0.1-0.2 ML. This hydroxylation is evidenced by the reduction in the sample workfunction with temperature [35]. After an exposure of 0.3 L H_2O (350 K) the intensity of the 2PPE feature remained constant, suggesting that all the O_b-vacs had been filled via dissociative water adsorption.

In order to separate any temperature effects on the 2PPE spectra from the effect of hydroxylation, the measurement in Figure 4.5 was repeated at different partial pressures of water. Figure 4.6a & b show that saturation of the 2PPE signal occurred more rapidly for higher partial pressures of water, suggesting that the 2PPE signal intensity correlates with water pressure. In a separate experiment, UPS He II ($h\nu$ = 40.8 eV) spectra were recorded from the reduced surface as it cooled from 560 K to 370 K under the same partial pressures of water as the 2PPE experiments. These measurements, shown in Figure 4.6c, evidence the

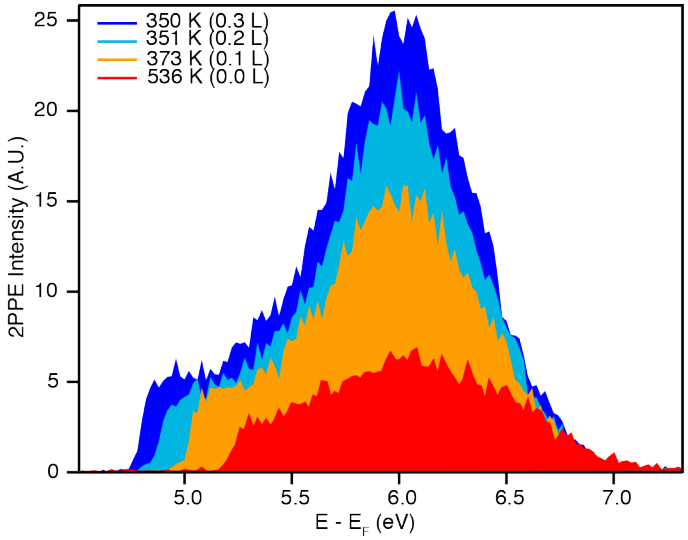

Figure 4.5: 2PPE spectra ($h\nu$ = 3.44 eV) measured as the sample cooled from 536 K to 350 K. As the sample cools, the workfunction value decreases and the 2PPE signal increases. The effective exposure to water is shown in brackets. Below ∼500 K, water adsorbs dissociatively at the surface to for two OH_b per O_b-vac. After an exposure of 0.3 L H_2O, the 2PPE signal saturates as all the O_b-vac are filled.

appearance a peak 10.8 eV below E_F, associated with the OH_b 3σ MO, over the same timescale as the increase in 2PPE intensity previously observed. Furthermore, the intensity of the BGS peak, centred ∼0.8 eV below E_F was unaffected in UPS He I spectra ($h\nu$ = 21.2 eV).

To eliminate the possibility that the 2PPE resonance is induced by the laser, through beam damage or photodissociation of adsorbed molecules, two tests were carried out. Firstly, UPS He I measurements confirmed that the BGS peak intensity was unchanged following irradiation by 3.44 eV photons (P≃1 mW) for 2 hours. Secondly, the 2PPE spectra themselves were stable over an irradiation period of 20 minutes. Hence, irradiation-induced effects are excluded from our interpretation of the data presented in this chapter.

Time-resolved 2PPE (TR-2PPE) spectra, measured from the *h*-TiO_2(110) surface and the Ta sample holder using 3.44 eV photons, are shown in Figure 4.7. 2PPE from the Ta sample holder proceeds via unoccupied states with lifetimes of just a few femtoseconds [45]. Hence, for TR-2PPE from the Ta sample holder, the spectral broadening resulting from the lifetimes of the unoccupied states is negligible in comparison to the laser pulse duration and the cross-correlation trace follows the temporal profile of the laser pulse. Fitting a Gaussian lineshape to the spectrum measured from the Ta sample holder reveals the pulse duration of the

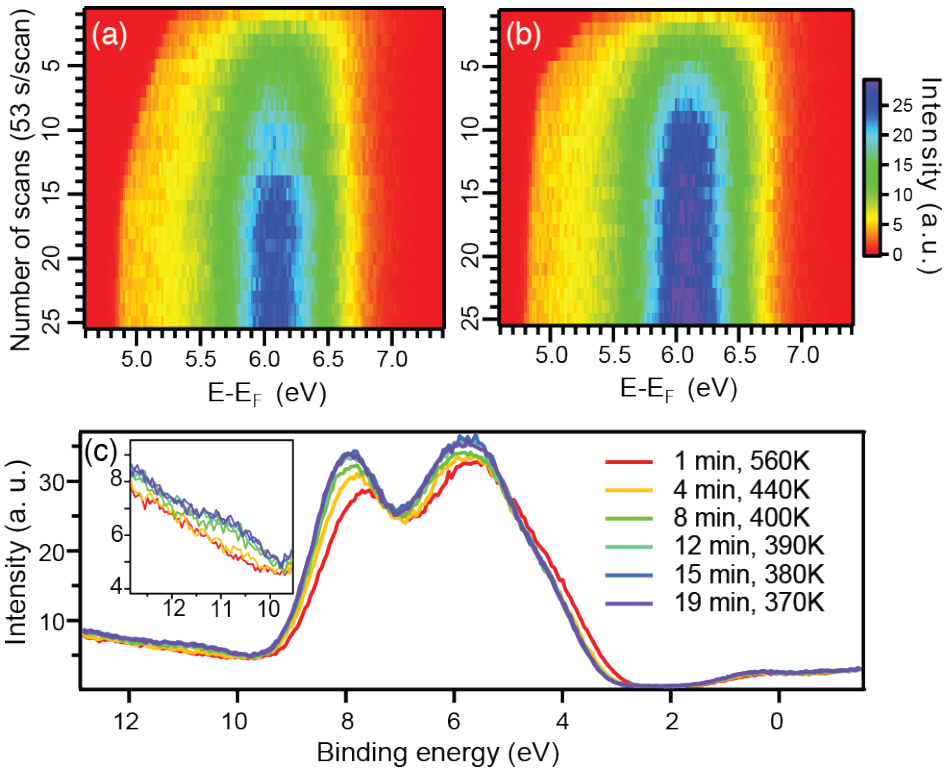

Figure 4.6: 2PPE and UPS spectra measured from the TiO_2(110) surface at various temperatures and water exposures. (a) and (b) display 2PPE spectra recorded as the sample cooled after annealing to ∼1000 K under lower and higher partial pressures of water, respectively. Saturation of the 2PPE signal occurs more rapidly under greater partial pressures of water, excluding any possible temperature effects. (c) UPS He II ($h\nu$ = 40.8 eV) measured as the sample cooled. The appearance of the peak ∼10.8 eV below E_F occurs on the same timescale as the increase of the 2PPE signal and is associated with the 3σ MO of OH_b.

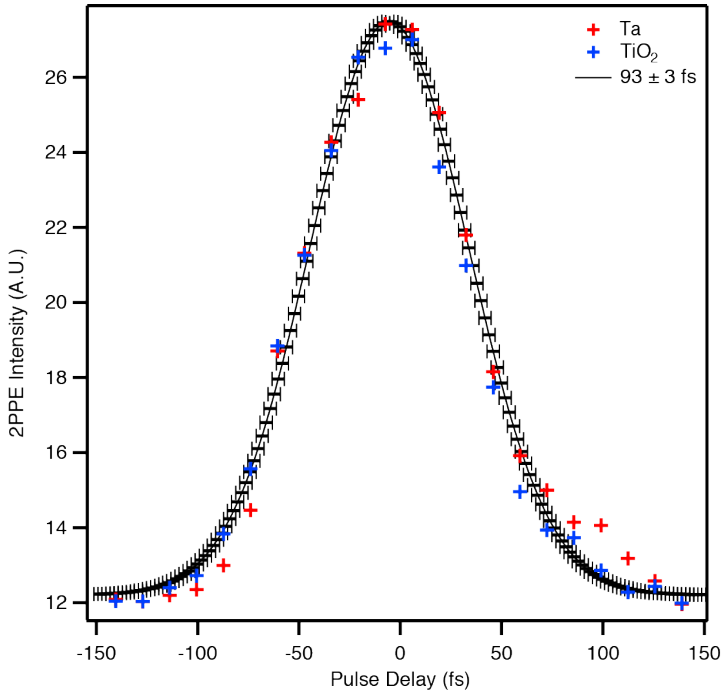

Figure 4.7: Time-resolved 2PPE spectra measured from *h*-TiO_2(110) (blue) and Ta polycrystalline (red) surfaces. The Ta spectrum was fit by a Gaussian lineshape and is assumed to represent the temporal profile of the laser pulse. No appreciable broadening was observed on the Gaussian width of (93 $\pm$ 3) fs, indicating that the lifetime of the unoccupied state at the *h*-TiO_2(110) surface is very fast. Hence, an upper limit of 14 fs for the lifetime of this state was inferred from the resolution of the measurement.

laser to be (93 $\pm$ 3) fs. No broadening was observed in the spectrum measured from the *h*-TiO_2(110) surface, suggesting that the lifetime of the unoccupied state is less than the resolution of our measurement.

By estimating the maximum possible broadening to the cross-correlation trace which could occur within our experimental resolution, an upper limit may be placed on the lifetime of the unoccupied state. Assuming a minimum laser pulse duration of 90 fs, the maximum possible broadening by the lifetime of the unoccupied state is 6 fs. By convoluting Gaussian profiles of various widths with a 90 fs cross-correlation, an upper limit of 14 fs is established for the lifetime of the unoccupied state on the *h*-TiO_2(110) surface. This result agrees well with the sub-15 fs lifetime measured for the 'wet-electron' state in Reference [27]. The lifetime of the unoccupied state on the 'bare' surface, which was likely hydroxylated, was too fast to be measured by the 10 fs laser pulse. Considering the results presented in this chapter, it is likely that no broadening was observed for the 'bare' surface since to the fixed photon energy available (3.05 eV) is below the onset of the 2PPE resonance.

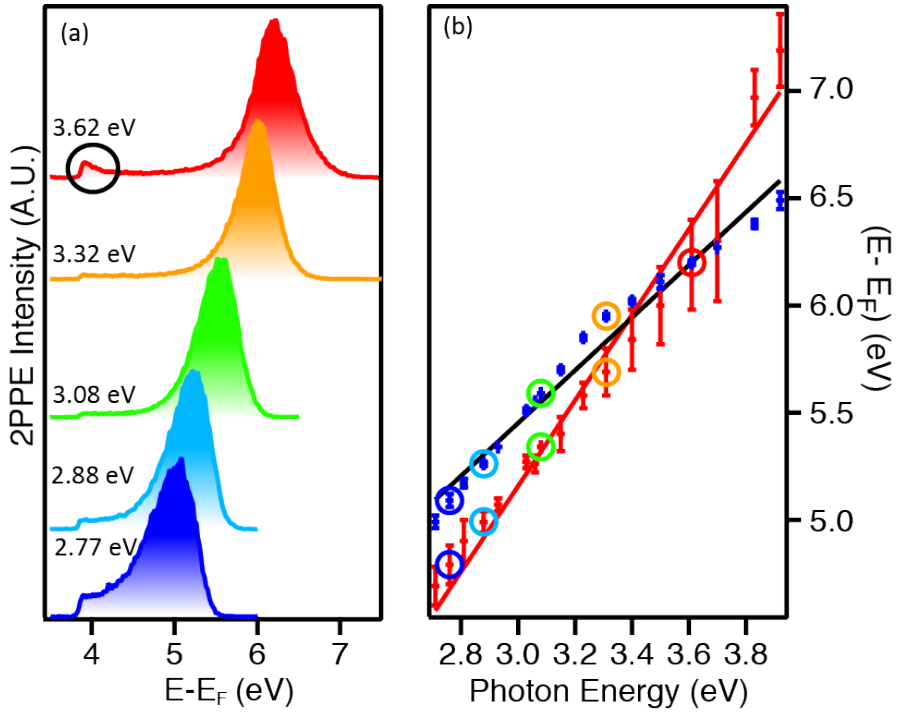

Figure 4.8: 2PPE spectra ($h\nu$ = 2.71-3.92 eV) measured from the water-covered *h*-TiO_2(110) surface. (a) Selected 2PPE spectra illustrating the resonant spectral feature and the onset of 2PPE from the valence band (black circle). (b) Energy dependence of the peaks fitted to the 2PPE spectra. The solid lines represent fits to Equations 2.5 (red) and 2.6 (black). The data points corresponding to the spectra shown in panel (a) are highlighted by circles of the same colour in panel (b).

4.3.2 The H_2O/TiO_2 Surface

According to the 'wet-electron' state interpretation of the 2PPE resonance at the hydrated TiO_2(110) surface, the energy and intensity of the 'wet-electron' state is a function of OH_b and H_2O coverage [27]. For the water-covered *h*-TiO_2(110) surface, the 'wet-electron' state was measured to be (2.4 $\pm$ 0.1) eV above E_F. Since the availability of tuneable laser pulses revealed the 2PPE resonance to be present even in the absence of adsorbed molecules, the water-covered surface is revisited in order to reconcile these observations.

The *h*-TiO_2(110) surface was exposed to (1.8 $\pm$ 0.2) L H_2O at $\sim$100 K. Subsequently, 2PPE spectra were acquired using photon energies between 2.71 eV and 3.92 eV (457 nm to 316 nm), and selected spectra are displayed in Figure 4.8a. The adsorption of water reduced the sample workfunction by $\sim$1 eV, as expected from X-ray photoemission [25] and 2PPE [35] measurements. The change indicated by these photoemission techniques is greater than the $\sim$0.6

eV change seen in metastable impact electron spectra [26]. These results are directly comparable, since 2PPE data suggests that the effect of water adsorption on the workfunction has little dependence on the sample preparation [35]. The saturation of the workfunction change suggests that the surface coverage of water is $\geq$1 ML after exposure to (1.8 $\pm$ 0.2) L H_2O at low temperature.

The 2PPE spectra in Figure 4.8 were fitted using the procedure described in Section 4.3.1. The photon energy dependence of the two fitted peaks is shown in Figure 4.8b. Invoking Equations 2.5 & 2.6, the energies of the occupied and unoccupied states are (0.84 $\pm$ 0.03) eV below and (2.50 $\pm$ 0.03) eV above E_F, respectively. As established previously, the BGS serve as the initial state in the 2PPE resonance. The energy of the unoccupied state is consistent with the (2.4 $\pm$ 0.1) eV measured for the 'wet-electron' state in Reference [27].

The energy of the unoccupied state at the water-covered *h*-TiO_2(110) surface is about 0.2 eV lower than measured in the absence of water at room temperature. However, core-level XPS and UPS measurements of the sample's valence band evidence a shift of all TiO_2 orbitals by (-0.10 $\pm$ 0.05) eV at $\sim$100 K, which is attributed to band bending induced by the adsorption of water [16]. This finding reconciles the difference in the measured energy of the BGS from the water-covered surface and the hydroxylated surface in Section 4.3.1. Accounting for band bending, the change in the central energy of the unoccupied state is $\sim$-0.1 eV following water adsorption. This is much smaller than the 2 eV or more shift predicted by DFT calculations of the 'wet-electron' state [27]. Scanning the surface density of states to $>$8 eV above E_F revealed no evidence of additional unoccupied states. Hence, it is proposed that the unoccupied state present at the reduced and hydroxylated surfaces is shifted by $\sim$-0.1 eV by the adsorption of molecular water.

Having determined the effect of water adsorption on the energy of the unoccupied state, we address its influence on the intensity of the 2PPE resonance. DFT calculations of the 'wet-electron' state predict a maximum in the intensity of the 2PPE resonance at 1 ML coverage of water. To test this assertion, the *h*-TiO_2(110) surface was exposed to (1.8 $\pm$ 0.2) L H_2O at $\sim$100 K and allowed to warm at a rate of $\sim$1 K/minute. During this time, UPS ($h\nu$ = 21.22 eV) and 2PPE ($h\nu$ = 3.23 eV) spectra were recorded. It is known from TPD measurements that monolayer water is stable on the TiO_2(110) surface at temperatures between $\sim$190 K and 230 K [40]. As a result, the sample surface condition will be constant in this temperature range and little variation will be seen in the UPS spectra. This allows for

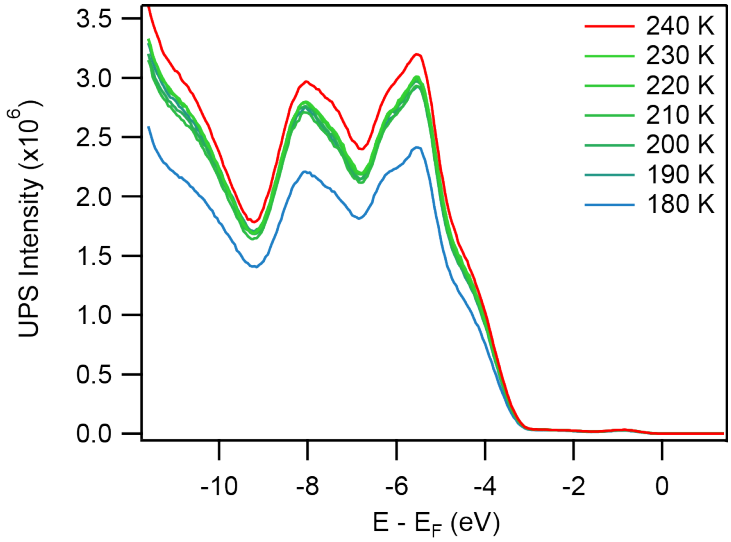

Figure 4.9: UPS He I ($h\nu$ = 21.2 eV) spectra measured from the water-covered *h*-TiO_2(110) surface as it warmed from 180 K to 240 K. The UPS spectra have not been normalised. The spectra are nearly identical over a temperature range of 190 K to 230 K, suggesting that the sample surface condition is constant. This is attributed to the presence of 1 ML H_2O.

calibration of the sample temperature.

Indeed, the measured UPS spectra were nearly identical over a range of 40K, between 160 K and 200 K according to the thermocouple. This is illustrated in Figure 4.9. Furthermore, saturation of sample workfunction change and the onset of BGS signal attenuation, which occur at and above monolayer coverage, respectively, coincided with these temperatures. The coincidence of these three diagnostic tools supports the assignment of 1 ML coverage between the measured temperatures of 160 K and 200 K. Since this range is $\sim$30 K lower than the behaviour seen in TPD measurements [40], where the temperature of the surface is much better defined, the temperatures associated with the UPS and 2PPE spectra measured below room temperature are shifted by 30 K to higher temperatures to correct for this systematic offset. The temperature difference is attributed to the 5 mm distance between the thermocouple and the sample. The UPS and 2PPE spectra are shown in Figure 4.10 with their corrected temperatures, which are referred to in the subsequent discussion.

The UPS spectra were fitted in the region of 3.5 eV below to 1 eV above E_F, as shown in Figure 4.11. The BGS appear (0.90 $\pm$ 0.05) eV below E_F in the UPS spectra. Figure 4.12 shows that the BGS peak area is smallest at 140 K, increasing until 190 K after which it is approximately constant. An additional peak, labelled satellite, was added 2.1 eV below E_F in order to improve the agreement

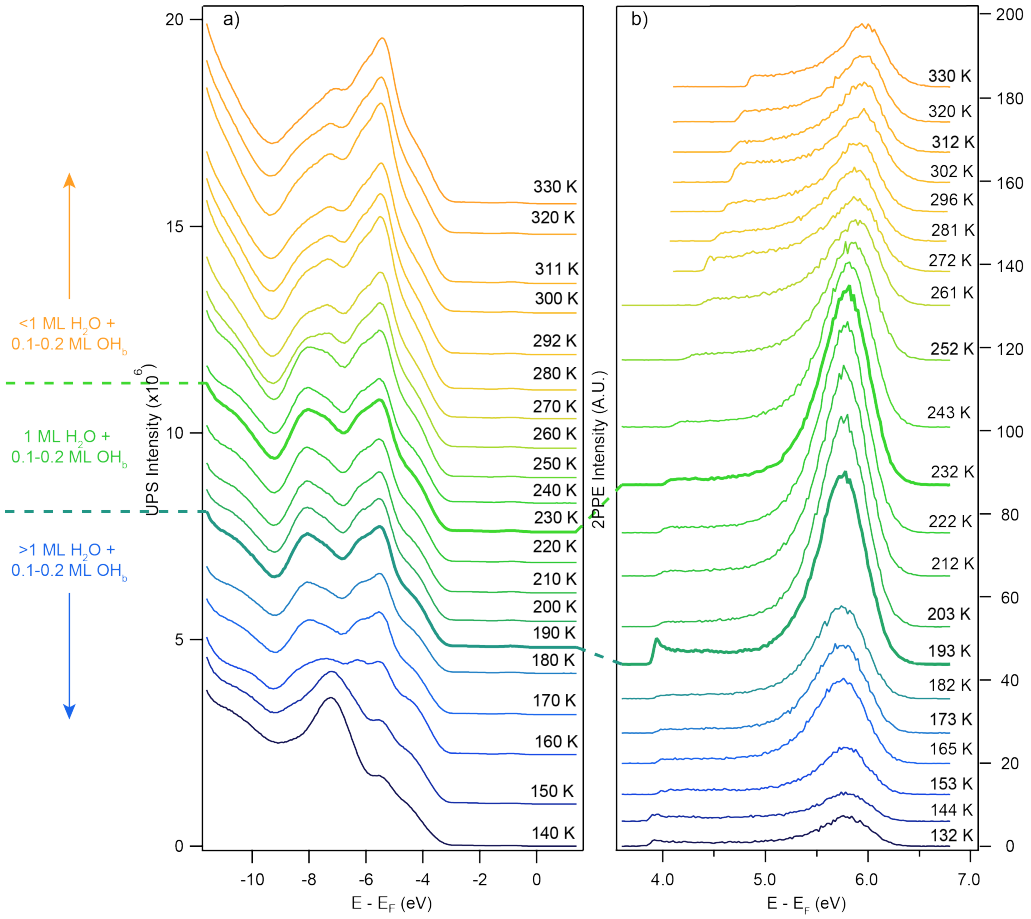

Figure 4.10: (a) UPS He I ($h\nu$ = 21.2 eV) and (b) 2PPE ($h\nu$ = 3.23 eV) acquired between 130 K and 330 K following exposure of the *h*-TiO_2(110) surface to ∼1.8 L H_2O at about 100 K.The 2PPE spectra display maximum intensity between 193 K and 232 K.

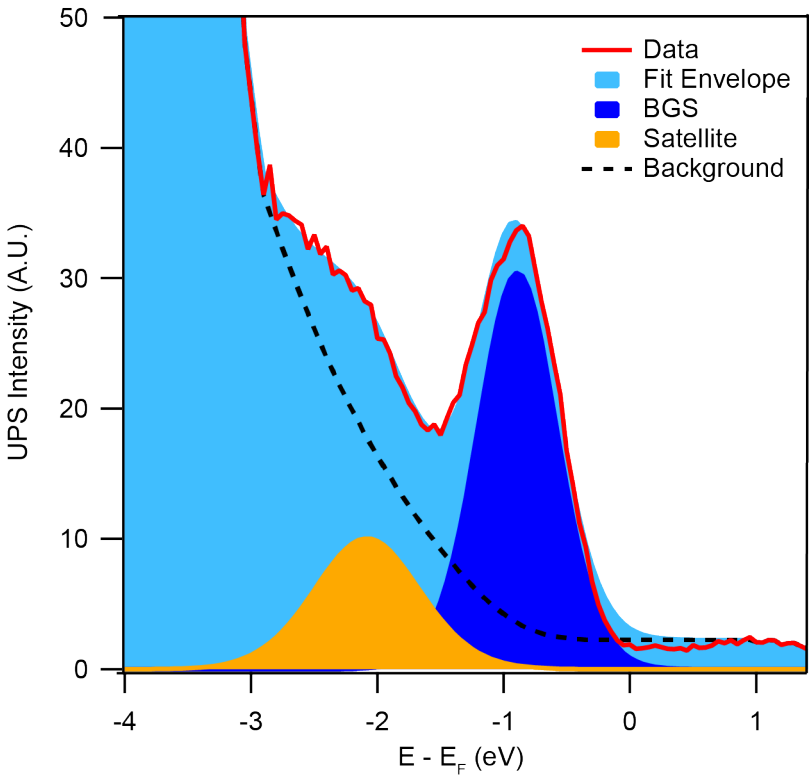

Figure 4.11: Example of the fitting procedure for UPS He I ($h\nu$ = 21.2 eV) for the spectrum measured at 240 K. Two Voigt-like peaks, representing the BGS (dark-blue) and satellite feature (orange), are superimposed upon a Tougaard background (dashed line). The satellite feature is believed to arise from photoemission from both the valence band and O 2s core levels caused by the He Iβ and He IIα, respectively, and does not appear in monochromatic synchrotron measurements [6, 16].

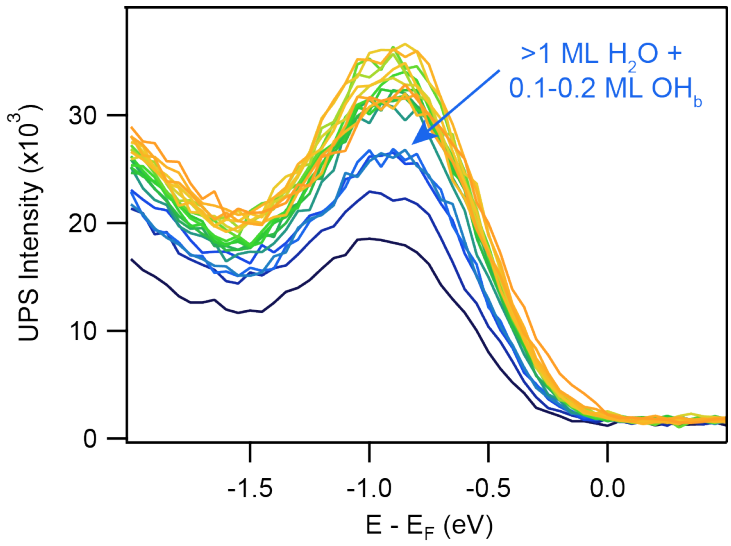

Figure 4.12: UPS He I ($h\nu$ = 21.2 eV) measurements from Figure 4.10, magnified to show the BGS. The colours correspond to the same temperatures as in Figure 4.10. At or below monolayer coverage, the BGS intensity is essentially constant (330-190 K, orange to green). Above 1 ML, the photoemission signal is attenuated by the physisorbed, second layer of water (180-140 K, light- to dark-blue).

of the fitting. Investigation into the origin of the satellite peak revealed that this feature was most intense when relatively low He pressure was used in the emission lamp, suggesting that it arises from photoemission via additional He emission lines. Additionally, this feature does not appear in monochromatic synchrotron measurements [6, 16]. Hence, the satellite feature is believed to originate from photoemission from both the valence band and O 2s core level, caused by the He Iβ and He IIα emission, respectively. The satellite peak displayed no significant change in area with water coverage.

The 2PPE spectra presented in Figure 4.10 contain a feature ~6 eV above E_F at all temperatures. This is attributed to resonant photoexcitation from the BGS to unoccupied levels in the conduction band region, as discussed in Section 4.3.1. The 2PPE peak is smallest at low temperatures and increases in intensity as the sample warms to 193 K. The intensity then remains roughly constant until 232 K, above which it again reduces in intensity. The 2PPE spectra were fitted using the procedure described in Figure 4.3. A shift of the peak pertaining to photoemission via the real unoccupied state of ~0.15 eV away from E_F was observed as the sample warmed from 222 K to 296 K. This shift is believed to arise partly from a reduction of band bending and a shift in the energy of the unoccupied state caused by water desorption as the sample warmed.

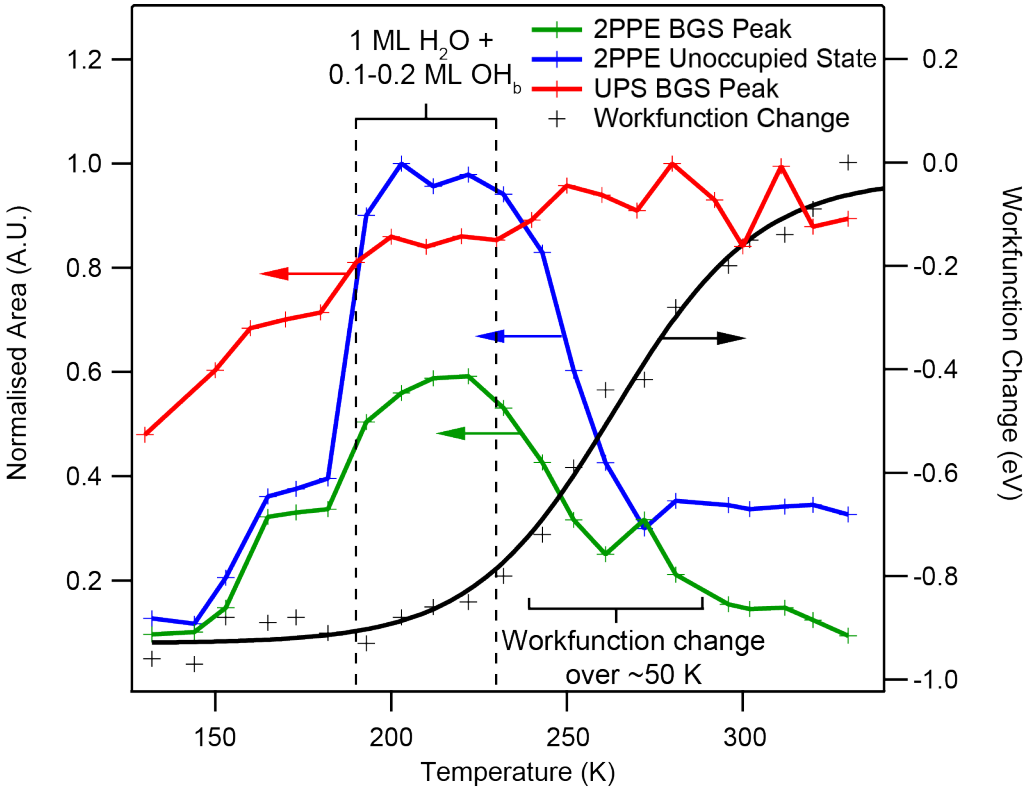

Figure 4.13: Results from the fitting of the UPS He I ($h\nu$ = 21.2 eV) and 2PPE ($h\nu$ = 3.23 eV) spectra in Figure 4.10. The 2PPE resonance reaches a maximum at 1 ML H_2O + 0.1-0.2 ML OH_b, indicated by the dashed lines. Changes in the 2PPE spectra may be attributed to changes in the excited state as the UPS BGS intensity is constant above 190 K. The maximum workfunction change, relative to that of the hydroxylated surface at 330 K, is (-0.92 $\pm$ 0.08) eV.

Chemisorption of molecular water was accompanied by a concomitant change in the workfunction. TPD studies of the adsorption behaviour of water at reduced TiO_2(110) surfaces serve as a useful comparison to workfunction measurements in the monolayer coverage regime. The workfunction measurements were fit with a sigmoid curve, shown in Figure 4.13, representing the integrated area of the monolayer adsorption peak in TPD measurements [40]. Since only the first, chemisorbed layer of water is expected to influence the sample workfunction, other features in TPD measurements were not considered [25, 35]. The width of the fitted sigmoid curve is about 50 K, in good agreement with the full-width at half maximum of the TPD monolayer peak centred at 270 K [40]. Similarly, the centre of the fitted sigmoidal curve was (264 $\pm$ 2) K.

The results obtained by fitting the UPS and 2PPE spectra are shown in Figure 4.13. The UPS BGS peak area (red) is normalised to its intensity at 280 K. The 2PPE peak areas are normalised to the intensity of the unoccupied state peak at 203 K. The workfunction change is measured relative to that of the *h*-TiO_2(110)

surface, recorded at 330 K. The maximum change in the sample workfunction was (-0.92 $\pm$ 0.04) eV, given by the form of the sigmoid curve. This value is consistent with the change observed in previous photoemission studies [25, 35].

The BGS peak area in the UPS spectra decreases below 190 K. Whilst hydroxylation of the reduced TiO_2(110) surface has been shown not to affect the intensity of the BGS [13, 16], molecular water is known to attenuate the photoemission signal from the surface significantly for coverages above 1 ML [46]. Hence, the reduction in the BGS peak area below 190 K is attributed to the presence of a second, physisorbed layer of water. Above 190 K, there is $\leq$1 ML H_2O and the BGS peak area is approximately constant. Since only water coverages above 1 ML attenuate the UPS BGS signal, the lower temperature limit of monolayer coverage in this experiment can be identified.

2PPE spectra are comprised of contributions from both occupied and unoccupied states, which are represented by the two peaks in the fitting procedure. The temperature dependence of the BGS (green) and unoccupied state (blue) peaks is shown in Figure 4.13. Both 2PPE peak areas display maxima between 193 K and 232 K, which corresponds to the monolayer coverage regime. As the sample temperature increases above 232 K, the coverage of water is expected to decrease and a concomitant decrease in the 2PPE peak areas is observed. UPS measurements of the BGS indicate that the intensity of this feature is constant above 190 K. Hence, enhancement of the 2PPE peak associated with photoexcitation via the real unoccupied state (blue) at 1 ML water coverage may be explained by modifications to the unoccupied state. The similar trend observed for the BGS peak, which proceeds via virtual excitation, may be explained by resonant enhancement of coherent 2PPE processes, due to the presence of a near-by resonance. An analogy may be drawn with resonance-enhanced four-wave mixing, $\omega_{FWM} = 2\omega_1 \pm \omega_2$, in which the proximity of a resonance at the two photon level ($2\omega_1$) enhances the intensity of light generated at the sum and difference frequencies (ω_{FWM}) [47].

The photon energy dependence of the resonant excitation process may also contribute to the observed maximum in the 2PPE signal with 1 ML water. The data shown in Figure 4.8 suggests that the energy of the unoccupied state shifts by 0.1 eV towards lower energies following the adsorption of molecular water. The shift in the energy of the unoccupied state brings the fixed photon energy of 3.23 eV closer to the resonant energy, resulting in an increase of the 2PPE peak from the BGS. This is supported by the 2PPE spectra acquired using variable pho-

ton energy presented previously, which display similar ratios of intensity for both 2PPE peaks for the same detuning from the resonant photon energies for the water-covered and hydroxylated surfaces.

There are three possible origins of the 2PPE signal enhancement observed for the *h*-TiO_2(110) surface at monolayer water coverage. First, we address the 'wet-electron' state interpretation. Although DFT calculations do not properly describe 2PPE spectra measured from the *h*-TiO_2(110) surface, these simulations do agree with observations from the water-covered surface [27]. The delocalised nature of the 'wet-electron' state orbitals may explain the reduced energy and slightly longer lifetime of the unoccupied state at the water-covered surface and may also be the origin of the enhanced resonance intensity. Above 1 ML coverage, the reduction in 2PPE intensity may be explained by the formation of HBs between the first and second layer of water. In the 'wet-electron' state interpretation, excited electrons are stabilised by the dangling hydrogen atoms of water molecules or hydroxyls. The formation of HBs between the first and second water layers consumes these dangling H atoms and hence reduces the density of unoccupied states [27].

2PPE spectra of the water-covered Cu(111) surface display an increase in the intensity of the solvated electron peak when the coverage was increased from one to four water bilayers [48]. This is opposite to the trend observed in Figure 4.13. Furthermore, the intensity of peaks from surface and image potential states pertaining to the bare Cu(111) surface decrease with water coverage. Hence, the second layer of water may decrease the 2PPE signal measured at the rutile TiO_2(110) surface via attenuation, as seen in UPS measurements of the BGS. Since the UPS BGS peak area decreases at temperatures below 190 K, changes in the 2PPE intensity cannot be attributed solely to changes in the unoccupied density of states. This observation suggests that the resonant 2PPE signal originates from the surface region rather than depending on adsorbed water molecules.

Secondly, the 2PPE signal enhancement may be related to the reduced workfunction of the water-covered surface, which allows greater separation between secondary electrons and the excited resonance signal. The separation between the sample workfunction and the 2PPE signal may be varied by changing the photon energy, however, the effect is not easily separated from the photon energy dependence of the resonance. Given that the resonant feature in Figure 4.10 is well separated from the workfunction cut-off for all photon energies, it is unlikely

that the the workfunction separation is the sole origin of the 2PPE enhancement at monolayer water coverage.

Finally, an explanation for the 2PPE enhancement at monolayer coverage may be found in evidence suggesting that the monolayer consists of a mix of molecular and dissociated water. The intensity of the 2PPE resonance was shown in Section 4.3.1 to depend on the coverage of OH_b. Hence, the enhancement of the 2PPE resonance in the presence of monolayer water may arise from the creation of additional hydroxyls and therefore be unrelated to molecular water. In support of this interpretation, the OH_b-OH_t believed to be formed via water dissociation in the monolayer desorb above 230 K, which coincides with the onset of the reduction of the 2PPE signal intensity [32]. Although BGS are associated with the *h*-TiO_2(110) surface, the dissociation of water neutral molecules is not expected to further reduce the surface and indeed the UPS BGS peak remains constant above 190 K.

4.3.3 Discussion

Several recently published works have examined the two-photon resonances present at the reduced and adsorbate-covered TiO_2(110) surfaces [1, 2, 4, 49, 50]. The persistence of the two-photon resonance to temperatures above the desorption temperature of OH_b has led to the consensus that the 2PPE spectra result from resonant photoexcitation from the BGS of Ti 3d t_{2g} character to t_{2g} or e_g levels in the conduction band [4, 49]. This assignment is supported by inverse photoemission studies, which evidence a broad feature centred about 3 eV above E_F following reduction of the oxidised surface by Ar^+ sputtering [51]. A concomitant increase of the BGS peak in photoemission measurements ($h\nu$ = 47 eV) suggests that the feature $\sim$3 eV above E_F in inverse photoemission spectra is associated with these Ti 3d levels [51]. Additionally, weak bands in absorption spectra at 2.30 eV and 2.92 eV have been attributed to spin allowed d-d transitions associated with the e_g levels of Ti^{3+} ions [52].

In Reference [49], the Ti 3d resonance was attributed to the presence of two nearly degenerate, unoccupied states, whose optical transition moments depend on the polarisation of the light and the surface azimuthal orientation. The 2PPE intensity was greatest when the electric field vector was parallel to the [110] and/or [1$\bar{1}$0] directions for both s- and p-polarised light. As the relevant states were

present in calculations of the bulk electronic structure of reduced TiO_2, the presence of OH_b was claimed to make no contribution to the 2PPE spectra [50]. Additionally, the 'wet-electron' states were proposed to be spectroscopically distinct from the d-d transitions, being observed only in p-polarised 2PPE spectra.

However, s-polarised 2PPE spectra measured from the reduced TiO_2(110) surface have been shown to be identical to 1PPE spectra measured using the doubled photon energy [4]. Hence, no contribution from unoccupied states can be claimed in s-polarised 2PPE spectra, contrary to the interpretation of Reference [49]. This is consistent with our assignment of some spectral intensity to virtual photoexcitation from the BGS, which is not considered in Reference [49]. Hence, photoexcitation via a real unoccupied state at the reduced TiO_2(110) occurs only in p-polarised 2PPE spectra and is most intense when the electric field vector is parallel to the [110] and/or [$1\bar{1}0$] directions [4]. DFT calculations of the rutile TiO_2(110) surface in Reference [4] suggest that reduction of the surface via hydroxylation reorganises the conduction band levels. Furthermore, 2PPE measurements demonstrated a linear relationship between the resonance signal and the coverage of OH_b [4]. Hence, OH_b and O_b-vacs were suggested to contribute similarly to the unoccupied state.

Considering the works described in this chapter, the origin of the 2PPE resonance at the reduced TiO_2(110) surface may be attributed to photoexcitation between the BGS of t_{2g} symmetry and unoccupied t_{2g} or e_g levels in the Ti 3d conduction band. The resonance is present at surfaces containing O_b-vacs but is greatly increased in intensity by hydroxylation. Hence, a large proportion of resonant signal is proposed to be associated with the surface, rather than the bulk, electronic structure. The increased 2PPE intensity observed at the surface in the presence of 1 ML H_2O is assigned to the creation of additional OH_b rather than the formation of 'wet electron' states. Similarly, studies of methanol and ethanol at the TiO_2(110) surface may be explained by laser-induced dissociation of these molecules and the production of additional OH_b groups [37].

4.4 Summary & Conclusion

In this chapter, 2PPE and UPS spectra measured from the reduced and adsorbate-covered rutile TiO_2(110) surfaces were presented. Resonant enhancement of the

2PPE signal was attributed to photoexcitation from the BGS to an unoccupied state centred (2.73 $\pm$ 0.03) eV above E_F at the reduced surface. As the resonance persists at temperatures above the desorption temperature of OH_b, the unoccupied state was associated with conduction band levels of e_g or t_{2g} symmetry. The intensity of the 2PPE resonance was seen to increase following hydroxylation of the surface via dissociative water adsorption at O_b-vacs. Since hydroxylation does not affect the energy or intensity of the BGS, the enhancement is attributed to modifications in the unoccupied state. The lifetime of the unoccupied state was too fast to be directly observed via TR-2PPE, however, an upper limit of 14 fs was established from the resolution of the experiment.

The effect of water adsorption at low temperatures on the 2PPE resonance was examined. The energy of the unoccupied state was found to decrease relative to the hydroxylated surface. On the water-covered surface the unoccupied state is centred (2.50 $\pm$ 0.03) eV above E_F. However, (0.10 $\pm$ 0.05) eV of the $\sim$0.2 eV shift was assigned to band bending, which is induced by water adsorption at low temperatures. Hence, the water-induced shift of the unoccupied state is only $\sim$-0.1 eV, much less than the $\sim$2 eV predicted by DFT calculations of the purported 'wet electron' state [27]. Investigating the density of states to over 8 eV above E_F did not evidence the existence of additional resonant unoccupied states.

Consistent with previous experimental works, a maximum in the 2PPE signal intensity was observed at 1 ML coverage of water. As UPS measurements of the BGS displayed constant intensity for water coverages of $\leq$1 ML, the enhancement of the 2PPE signal was assigned unambiguously to modifications in the unoccupied density of states. The enhancement was suggested to arise from the creation of additional bridging hydroxyls in the monolayer, supported by photoemission and photoelectron diffraction studies [30–34]. Features pertaining to 'wet electron' states at the reduced TiO_2(110) surface have been observed only by one research group [27, 50]. Subsequently, this assignment remains controversial. The evidence presented in this chapter suggests that the 2PPE resonance present at reduced and adsorbate-covered surfaces may be explained by enhancement of the intrinsic Ti 3d resonance by adsorbed OH_b, whose central energy weakly depends upon the presence co-adsorbed molecules.

Future work on this topic may investigate charge transfer to or from photoexcited molecules at the reduced TiO_2(110) surface. This is of interest as the mechanism underlying the function of dye-sensitised solar cells is believed to rely on efficient injection of photoexcited electrons from the dye molecule to the conduc-

tion band of TiO_2. Further study of the resonant d-d transition identified in this work may provide insight into decay of injected electrons into conduction band levels. The presence of the defects such as O_b-vacs and OH_b may be beneficial to some catalytic processes by providing active sites for adsorption, whilst hindering others by increasing the likelihood of electron-hole recombination at the surface [53–59]. Energy- and time-resolved photoemission studies may augment scanning probe measurements to provide a fundamental understanding of these processes. Finally, it may be possible to verify the existence of 'wet electron'-like states predicted at the TiO_2-terminated $SrTiO_3$(100) surface following water adsorption via 2PPE [60].

References

[1] Y. Zhang, D. T. Payne, C. L. Pang, H. H. Fielding, and G. Thornton, "Non-Band-Gap Photoexcitation of Hydroxylated TiO_2," *The Journal of Physical Chemistry Letters*, vol. 6, no. 17, pp. 3391–3395, 2015.

[2] D. T. Payne, Y. Zhang, C. L. Pang, H. H. Fielding, and G. Thornton, "Coverage-dependent two-photon photoexcitation at the H_2O/TiO_2 interface," *Surface Science*, vol. 652, pp. 189–194, 2016.

[3] L. Kavan, M. Grätzel, S. E. Gilbert, C. Klemenz, and H. J. Scheel, "Electrochemical and Photoelectrochemical Investigation of Single-Crystal Anatase," *Journal of the American Chemical Society*, vol. 118, no. 28, pp. 6716–6723, 1996.

[4] Z. Wang, B. Wen, Q. Hao, L.-M. Liu, C. Zhou, X. Mao, X. Lang, W.-J. Yin, D. Dai, A. Selloni, and X. Yang, "Localized Excitation of Ti^{3+} Ions in the Photoabsorption and Photocatalytic Activity of Reduced Rutile TiO_2," *Journal of the American Chemical Society*, vol. 137, no. 28, pp. 9146–9152, 2015.

[5] C. M. Yim, C. L. Pang, and G. Thornton, "Oxygen Vacancy Origin of the Surface Band-Gap State of TiO_2," *Physical Review Letters*, vol. 104, no. 3, p. 036806, 2010.

[6] A. G. Thomas, W. R. Flavell, A. K. Mallick, A. R. Kumarasinghe, D. Tsoutsou, N. Khan, C. Chatwin, S. Rayner, G. C. Smith, R. L. Stockbauer, S. Warren, T. K. Johal, S. Patel, D. Holland, A. Taleb, and F. Wiame, "Comparison of the electronic structure of anatase and rutile TiO_2 single-crystal surfaces using resonant photoemission and x-ray absorption spectroscopy," *Physical Review B*, vol. 75, no. 3, p. 035105, 2007.

[7] R. Sanjines, H. Tang, H. Berger, F. Gozzo, G. Margaritondo, and F. Levy, "Electronic structure of anatase TiO_2 oxide," *Journal of Applied Physics*, vol. 75, no. 6, p. 2945, 1994.

[8] M. Setvin, C. Franchini, X. Hao, M. Schmid, A. Janotti, M. Kaltak, C. G. Van de Walle, G. Kresse, and U. Diebold, "Direct View at Excess Electrons in TiO_2 Rutile and Anatase," *Physical Review Letters*, vol. 113, no. 8, p. 086402, 2014.

[9] P. Deák, B. Aradi, and T. Frauenheim, "Quantitative theory of the oxygen vacancy and carrier self-trapping in bulk TiO_2," *Physical Review B*, vol. 86, no. 19, p. 195206, 2012.

[10] M. Setvin, X. Hao, B. Daniel, J. Pavelec, Z. Novotny, G. S. Parkinson, M. Schmid, G. Kresse, C. Franchini, and U. Diebold, "Charge Trapping at the Step Edges of TiO_2 Anatase (101)," *Angewandte Chemie International Edition*, vol. 53, no. 18, pp. 4714–4716, 2014.

[11] P. G. Moses, A. Janotti, C. Franchini, G. Kresse, and C. G. Van de Walle, "Donor defects and small polarons on the TiO_2(110) surface," *Journal of Applied Physics*, vol. 119, no. 18, p. 181503, 2016.

[12] S. Chretien and H. Metiu, "Electronic Structure of Partially Reduced Rutile TiO_2(110) Surface: Where Are the Unpaired Electrons Located?," *The Journal of Physical Chemistry C*, vol. 115, no. 11, pp. 4696–4705, 2011.

[13] C. Di Valentin, G. Pacchioni, and A. Selloni, "Electronic Structure of Defect States in Hydroxylated and Reduced Rutile TiO_2(110) Surfaces," *Physical Review Letters*, vol. 97, no. 16, p. 166803, 2006.

[14] C. L. Pang, R. Lindsay, and G. Thornton, "Structure of Clean and Adsorbate-Covered Single-Crystal Rutile TiO_2 Surfaces," *Chemical Reviews*, vol. 113, no. 6, pp. 3887–3948, 2013.

[15] M. A. Henderson, W. S. Epling, C. H. F. Peden, and C. L. Perkins, "Insights into Photoexcited Electron Scavenging Processes on TiO_2 Obtained from Studies of the Reaction of O_2 with OH Groups Adsorbed at Electronic Defects on TiO_2(110)," *The Journal of Physical Chemistry B*, vol. 107, no. 2, pp. 534–545, 2003.

[16] R. L. Kurtz, R. Stock-Bauer, T. E. Madey, E. Román, and J. De Segovia, "Synchrotron radiation studies of H_2O adsorption on TiO_2(110)," *Surface Science*, vol. 218, no. 1, pp. 178–200, 1989.

[17] Z. Zhang, K. Cao, and J. T. Yates, "Defect-Electron Spreading on the TiO_2(110) Semiconductor Surface by Water Adsorption," *The Journal of Physical Chemistry Letters*, vol. 4, no. 4, pp. 674–679, 2013.

[18] V. N. Bogomolov and D. N. Mirlin, “Optical Absorption by Polarons in Rutile (TiO_2) Single Crystals,” *Physica Status Solidi (b)*, vol. 27, no. 1, pp. 443–453, 1968.

[19] I. M. Brookes, C. A. Muryn, and G. Thornton, “Imaging Water Dissociation on TiO_2(110),” *Physical Review Letters*, vol. 87, no. 26, p. 266103, 2001.

[20] A. Migani, D. J. Mowbray, J. Zhao, and H. Petek, “Quasiparticle Interfacial Level Alignment of Highly Hybridized Frontier Levels: H_2O on TiO_2(110),” *Journal of Chemical Theory and Computation*, vol. 11, no. 1, pp. 239–251, 2015.

[21] P. A. Thiel and T. E. Madey, “The interaction of water with solid surfaces: Fundamental aspects,” *Surface Science Reports*, vol. 7, no. 6-8, pp. 211–385, 1987.

[22] J. Connor, M. Considine, I. Hillier, and D. Briggs, “Low energy photoelectron spectroscopy of solids. Aspects of experimental methodology concerning metals and insulators,” *Journal of Electron Spectroscopy and Related Phenomena*, vol. 12, no. 2, pp. 143–159, 1977.

[23] O. Bikondoa, C. L. Pang, R. Ithnin, C. A. Muryn, H. Onishi, and G. Thornton, “Direct visualization of defect-mediated dissociation of water on TiO_2(110),” *Nature Materials*, vol. 5, no. 3, pp. 189–192, 2006.

[24] M. A. Henderson, “Structural Sensitivity in the Dissociation of Water on TiO_2 Single-Crystal Surfaces,” *Langmuir*, vol. 12, no. 21, pp. 5093–5098, 1996.

[25] M. B. Hugenschmidt, L. Gamble, and C. T. Campbell, “The interaction of H_2O with a TiO_2(110) surface,” *Surface Science*, vol. 302, no. 3, pp. 329–340, 1994.

[26] S. Krischok, O. Höfft, J. Günster, J. Stultz, D. Goodman, and V. Kempter, “H_2O interaction with bare and Li-precovered TiO_2: studies with electron spectroscopies (MIES and UPS(HeI and II)),” *Surface Science*, vol. 495, no. 1-2, pp. 8–18, 2001.

[27] K. Onda, “Wet Electrons at the H_2O/TiO_2(110) Surface,” *Science*, vol. 308, no. 5725, pp. 1154–1158, 2005.

[28] L.-M. Liu, C. Zhang, G. Thornton, and A. Michaelides, “Structure and dynamics of liquid water on rutile TiO_2(110),” *Physical Review B*, vol. 82, no. 16, p. 161415, 2010.

[29] G. A. Kimmel, M. Baer, N. G. Petrik, J. VandeVondele, R. Rousseau, and C. J. Mundy, "Polarization- and Azimuth-Resolved Infrared Spectroscopy of Water on TiO_2(110): Anisotropy and the Hydrogen-Bonding Network," *The Journal of Physical Chemistry Letters*, vol. 3, no. 6, pp. 778–784, 2012.

[30] L. E. Walle, A. Borg, P. Uvdal, and A. Sandell, "Experimental evidence for mixed dissociative and molecular adsorption of water on a rutile TiO_2(110) surface without oxygen vacancies," *Physical Review B*, vol. 80, no. 23, p. 235436, 2009.

[31] L. E. Walle, A. Borg, P. Uvdal, and A. Sandell, "Probing the influence from residual Ti interstitials on water adsorption on TiO_2(110)," *Physical Review B*, vol. 86, no. 20, p. 205415, 2012.

[32] L. Walle, D. Ragazzon, A. Borg, P. Uvdal, and A. Sandell, "Competing water dissociation channels on rutile TiO_2(110)," *Surface Science*, vol. 621, pp. 77–81, 2014.

[33] L. E. Walle, D. Ragazzon, A. Borg, P. Uvdal, and A. Sandell, "Photoemission studies of water dissociation on rutile TiO_2(110): Aspects on experimental procedures and the influence of steps," *Applied Surface Science*, vol. 303, pp. 245–249, 2014.

[34] D. A. Duncan, F. Allegretti, and D. P. Woodruff, "Water does partially dissociate on the perfect TiO_2(110) surface: A quantitative structure determination," *Physical Review B*, vol. 86, no. 4, p. 045411, 2012.

[35] K. Onda, B. Li, and H. Petek, "Two-photon photoemission spectroscopy of TiO_2(110) surfaces modified by defects modified by O_2 or H_2O adsorbates," *Physical Review B*, vol. 70, no. 4, p. 045415, 2004.

[36] Z.-Q. Wang, Q.-Q. Hao, X.-C. Mao, C.-Y. Zhou, Z.-B. Ma, Z.-F. Ren, D.-X. Dai, and X.-M. Yang, "Characterization of the Excited State on Methanol/TiO_2(110) Interface," *Chinese Journal of Chemical Physics*, vol. 28, no. 2, pp. 123–127, 2015.

[37] Z. Ma, Q. Guo, X. Mao, Z. Ren, X. Wang, C. Xu, W. Yang, D. Dai, C. Zhou, H. Fan, and X. Yang, "Photocatalytic Dissociation of Ethanol on TiO_2(110) by Near-Band-Gap Excitation," *The Journal of Physical Chemistry C*, vol. 117, no. 20, pp. 10336–10344, 2013.

[38] K. Onda, B. Li, J. Zhao, and H. Petek, "The electronic structure of methanol covered TiO_2(110) surfaces," *Surface Science*, vol. 593, no. 1-3, pp. 32–37, 2005.

[39] X. Mao, D. Wei, Z. Wang, X. Jin, Q. Hao, Z. Ren, D. Dai, Z. Ma, C. Zhou, and X. Yang, "Recombination of Formaldehyde and Hydrogen Atoms on TiO_2(110)," *The Journal of Physical Chemistry C*, vol. 119, no. 2, pp. 1170–1174, 2015.

[40] M. A. Henderson, "An HREELS and TPD study of water on TiO_2(110): the extent of molecular versus dissociative adsorption," *Surface Science*, vol. 355, no. 1-3, pp. 151–166, 1996.

[41] H. Ueba and B. Gumhalter, "Theory of two-photon photoemission spectroscopy of surfaces," *Progress in Surface Science*, vol. 82, no. 4-6, pp. 193–223, 2007.

[42] A. C. Papageorgiou, N. S. Beglitis, C. L. Pang, G. Teobaldi, G. Cabailh, Q. Chen, A. J. Fisher, W. A. Hofer, and G. Thornton, "Electron traps and their effect on the surface chemistry of TiO_2(110)," *Proceedings of the National Academy of Sciences of the United States of America*, vol. 107, no. 6, pp. 2391–2396, 2010.

[43] S. Wendt, P. T. Sprunger, E. Lira, G. K. H. Madsen, Z. Li, J. O. Hansen, J. Matthiesen, A. Blekinge-Rasmussen, E. Laegsgaard, B. Hammer, and F. Besenbacher, "The Role of Interstitial Sites in the Ti3d Defect State in the Band Gap of Titania," *Science*, vol. 320, no. 5884, pp. 1755–1759, 2008.

[44] V. E. Henrich, G. Dresselhaus, and H. J. Zeiger, "Observation of Two-Dimensional Phases Associated with Defect States on the Surface of TiO_2," *Physical Review Letters*, vol. 36, no. 22, pp. 1335–1339, 1976.

[45] V. P. Zhukov, O. Andreyev, D. Hoffmann, M. Bauer, M. Aeschlimann, E. V. Chulkov, and P. M. Echenique, "Lifetimes of excited electrons in Ta: Experimental time-resolved photoemission data and first-principles GW+T theory," *Physical Review B*, vol. 70, no. 23, p. 233106, 2004.

[46] V. E. Henrich, G. Dresselhaus, and H. Zeiger, "Chemisorbed phases of H_2O on TiO_2 and $SrTiO_3$," *Solid State Communications*, vol. 24, no. 9, pp. 623–626, 1977.

[47] R. Hilbig and R. Wallenstein, "Resonant sum and difference frequency mixing in Hg," *IEEE Journal of Quantum Electronics*, vol. 19, no. 12, pp. 1759–1770, 1983.

[48] C. Gahl, U. Bovensiepen, C. Frischkorn, and M. Wolf, "Ultrafast Dynamics of Electron Localization and Solvation in Ice Layers on Cu(111)," *Physical Review Letters*, vol. 89, no. 10, p. 107402, 2002.

[49] A. Argondizzo, X. Cui, C. Wang, H. Sun, H. Shang, J. Zhao, and H. Petek, "Ultrafast multiphoton pump-probe photoemission excitation pathways in rutile TiO_2(110)," *Physical Review B*, vol. 91, no. 15, p. 155429, 2015.

[50] A. Argondizzo, S. Tan, and H. Petek, "Resonant Two-Photon Photoemission from Ti 3d Defect States of TiO_2(110) Revisited," *The Journal of Physical Chemistry C*, vol. 120, no. 24, pp. 12959–12966, 2016.

[51] A. K. See, "Inverse photoemission study of the defective TiO_2(110) surface," *Journal of Vacuum Science & Technology A: Vacuum, Surfaces, and Films*, vol. 10, no. 4, p. 2591, 1992.

[52] V. M. Khomenko, K. Langer, H. Rager, and A. Fett, "Electronic absorption by Ti^{3+} ions and electron delocalization in synthetic blue rutile," *Physics and Chemistry of Minerals*, vol. 25, no. 5, pp. 338–346, 1998.

[53] O. Carp, "Photoinduced reactivity of titanium dioxide," *Progress in Solid State Chemistry*, vol. 32, no. 1-2, pp. 33–177, 2004.

[54] X. Chen, L. Liu, P. Y. Yu, and S. S. Mao, "Increasing Solar Absorption for Photocatalysis with Black Hydrogenated Titanium Dioxide Nanocrystals," *Science*, vol. 331, no. 6018, pp. 746–750, 2011.

[55] Z.-T. Wang, N. A. Deskins, M. A. Henderson, and I. Lyubinetsky, "Inhibitive Influence of Oxygen Vacancies for Photoactivity on TiO_2(110)," *Physical Review Letters*, vol. 109, no. 26, p. 266103, 2012.

[56] N. G. Petrik and G. A. Kimmel, "Reaction Kinetics of Water Molecules with Oxygen Vacancies on Rutile TiO_2(110)," *The Journal of Physical Chemistry C*, vol. 119, no. 40, pp. 23059–23067, 2015.

[57] K. E. Kweon, D. Manogaran, and G. S. Hwang, "Synergetic Role of Photogenerated Electrons and Holes in the Oxidation of CO to CO_2 on Reduced TiO_2(110): A First-Principles Study," *ACS Catalysis*, vol. 4, no. 11, pp. 4051–4056, 2014.

[58] Z.-T. Wang, M. A. Henderson, and I. Lyubinetsky, "Origin of Coverage Dependence in Photoreactivity of Carboxylate on TiO_2(110): Hindering by Charged Coadsorbed Hydroxyls," *ACS Catalysis*, vol. 5, no. 11, pp. 6463–6467, 2015.

[59] C. Zhou, Z. Ma, Z. Ren, X. Mao, D. Dai, and X. Yang, "Effect of defects on photocatalytic dissociation of methanol on TiO_2(110)," *Chemical Science*, vol. 2, no. 10, pp. 1980–1983, 2011.

[60] S. Raghavan, A. Carvalho, F. Le Formal, N. Setter, S. Oberg, and P. R. Briddon, “Adsorbate-localized states at water-covered (100) $SrTiO_3$ surfaces,” *Applied Physics Letters*, vol. 98, no. 1, p. 012106, 2011.

Chapter 5

Excess Electron Creation at the Anatase TiO_2(101) Surface

Abstract

Reduction & oxidation reactions at the technologically relevant anatase TiO_2(101) surface are facilitated by excess electrons. The availability and localisation of these electrons is dictated by the defect concentration at the surface. This chapter presents a two-photon (2PPE, $h\nu$ = 3.01 - 3.45 eV) and ultra-violet (UPS, $h\nu$ = 21.2 and 40.8 eV) photoemission spectroscopy study, evidencing an increased concentration of excess electrons subsequent to electron bombardment at room temperature. Irradiation-induced surface oxygen vacancies at the anatase TiO_2 (101) surface quickly migrate to the sub-surface region at this temperature, restoring the equilibrium surface defect concentration. Hence, we propose that the irradiated surface is, in fact, hydroxylated. This finding is corroborated by the appearance of new features in UPS difference spectra. These peaks, centred 8.45 eV, 6.50 eV and 0.73 eV below the Fermi level (E_F), are associated with the 3σ and 1π hydroxyl molecular orbitals and Ti 3d band gap states, respectively. The greater concentration of excess electrons at the hydroxylated anatase TiO_2(101) surface may increase the potential for redox reactions.

The work presented in this chapter has been published as Reference [1].

5.1 Introduction

As with many metal oxides, the surface physics and chemistry of TiO_2 is heavily influenced by the presence of surface defects [2]. The creation of defects, namely oxygen vacancies (O_b-vacs), hydroxyls (OH), Ti interstitial atoms and step edges, leads to excess electrons, which may become trapped in the crystal lattice to form polarons [2–4]. Excess electrons at the anatase TiO_2(101) surface may only be trapped at defects [5, 6]. Consequently, defect sites accumulate excess electrons and often act as the prefered adsorption sites for molecules in the gas- or liquid-phase [2, 5, 7, 8]. Since the transfer of electrons to molecules adsorbed at the surface initiates redox reactions, insight into the nature of defects in TiO_2 is crucial for a complete understanding of its catalytic applications.

The reduction of anatase TiO_2 alters its electrical conductivity, changing it from an insulator to an n-type semiconductor with an indirect band-gap of 3.2 eV [9]. This increased conductivity is believed to be facilitated by excess electrons, which occupy Ti 3d states of t_{2g}-like symmetry, and manifest as a feature $\sim$1 eV below the Fermi level (E_F) in photoemission spectroscopy [10–12]. These states are referred to as the band gap states (BGS). Excess electrons added to the conduction band of a metal oxide may either retain their free-carrier behaviour or couple to lattice distortions induced by this surplus charge. This electron-phonon interaction is refered to as either a small or large polaron, depending on the extent of localisation [4]. Polaronic effects and the degree of electron localisation influence a material's chemical and physical properties. However, the modelling of such phenomena remains controversial [13, 14].

At stoichiometric and reduced rutile TiO_2(110) surfaces, excess electrons may localise at Ti sites to form small polarons [6]. In contrast, at the stoichiometric anatase TiO_2(101) surface excess electrons exhibit free-carrier behaviour. Consequently, the crystal lattice is unperturbed and excess electrons are distributed homogeneously throughout the material [6]. The same behaviour has been observed for excess electrons in the bulk [14]. This band-like charge carrier transport is required in applications such as photoelectrochemical solar cells. However, electron localisation and polaron formation at surfaces is beneficial for catalytic processes as it improves charge transfer to adsorbed molecules [7].

Recent evidence suggests that polaron formation occurs at the anatase TiO_2(101) surface following the creation of surface oxygen vacancies (O_b-vacs) [6]. O_b-vacs

at the anatase TiO_2(101) surface migrate to the sub-surface region at or above 200 K [15]. The surface coverage of O_b-vacs reaches a dynamic, thermally-dependent equilibrium, which results in a coverage of around 1% of a monolayer (ML) at 300 K. Hence, O_b-vacs are scarce at the anatase TiO_2(101) surface following typical ultra-high vacuum (UHV) sample preparation. O_b-vacs may be created at the surface via electron bombardment [15, 16], or pulled to the surface from the sub-surface region using a strongly negatively charged STM tip [17]. Scanning tunnelling spectroscopy of Ti atoms and O_b-vacs, measured at 6 K, revealed that the BGS are strictly localised to point defects at the anatase TiO_2(101) surface. These spectra are shown in Figure 5.1. Additionally, polaronic states at deeper lying energy levels have been associated with step edges [5]. These spectra reveal the nature of excess electrons at the anatase TiO_2(101) surface.

O_b-vacs at the reduced rutile TiO_2(110) surface are active sites for dissociative adsorption of gas-phase water for temperatures between 170 K and 520 K [18]. Similar predictions have been made for O_b-vacs at the anatase TiO_2(101) surface on the basis of molecular dynamics simulations [19]. Dissociative adsorption at surface O_b-vacs was predicted to result in the formation of two bridging hydroxyl groups (OH_b) per surface O_b-vac. In the absence of such point defects, the majority of experimental and theoretical works conclude that water adsorbs molecularly [8, 19–23], although there is also evidence suggesting a mixed monolayer of water and hydroxyls occurs [24, 25]. Recent simulations of the elecronic structure of hydroxylated and water-covered anatase TiO_2(101) reveal the alignment and extent of hybridisation of these adsorbates with the O 2p valence band of TiO_2 [26]. However, no experimental data was avaliable for comparison.

In this chapter, two-photon and ultra-violet photoemission spectroscopies are employed to study the the valence band and BGS of the single crystal anatase TiO_2(101) surface. Interpretations of the modifications induced by water adsorption and electron bombardment are discussed in terms of their physical and chemical nature and their implications for the applications of TiO_2.

5.2 Experimental Procedure

A natural anatase TiO_2(101)(1$\times$1) single crystal sample (5$\times$5 mm) was prepared by cycles of Ar^+ sputtering (1 kV, 1.5 μA cm^{-2}, 30 minutes) and thermal annealing

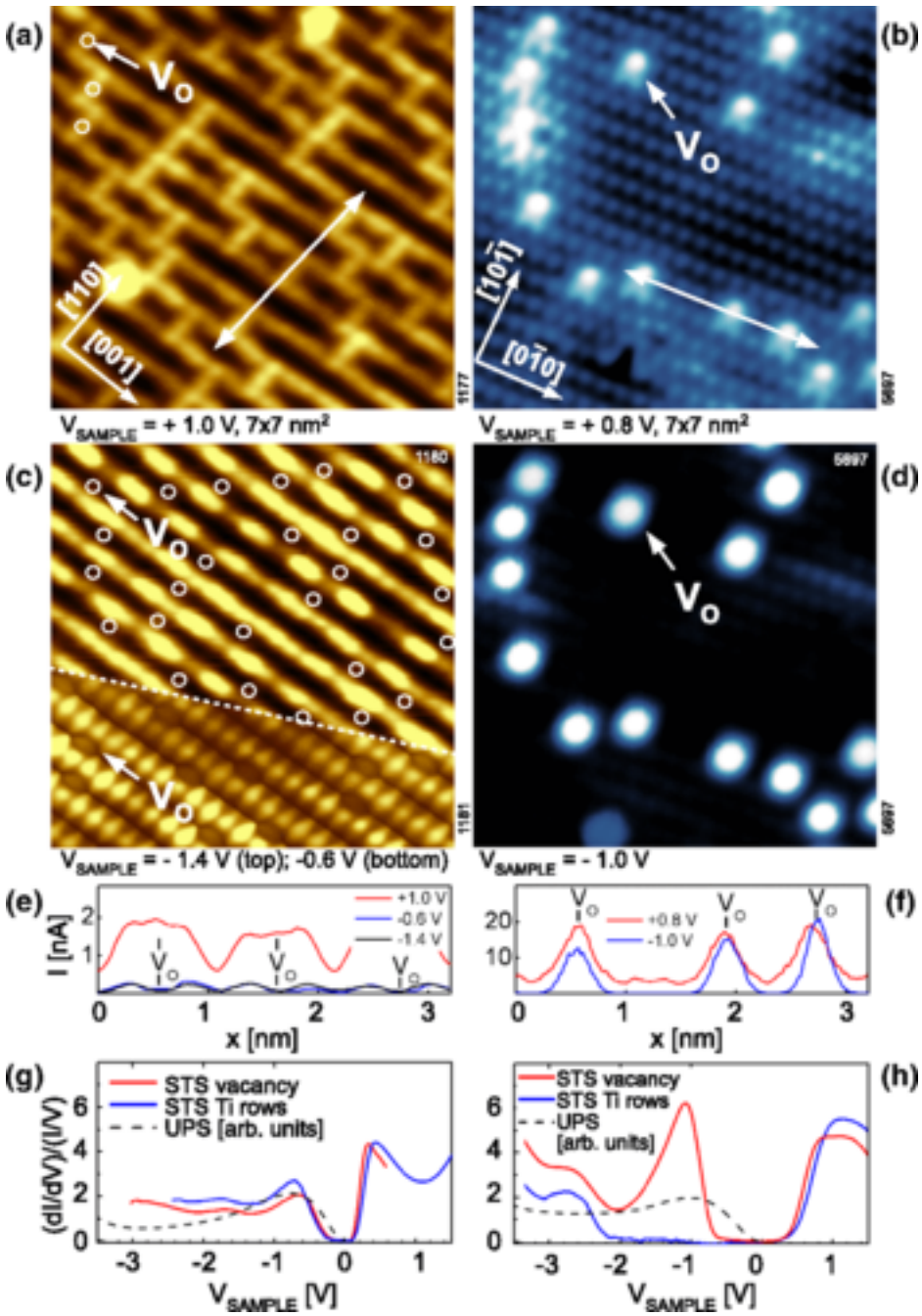

Figure 5.1: STM (a)-(d) & STS (e)-(h) measurements from rutile TiO_2(110) (left column) and anatase TiO_2(101) (right column) surfaces. STS spectra from the anatase surface (h) exhibit a peak 1 eV below E_F associated with polaronic states when measured at surface O_b-vacs sites only. Reproduced from Reference [6].

to a maximum temperature of 950 K (10 minutes). The long-range surface order was verified by low-energy electron diffraction (LEED) and the contamination level was determined to be less than 0.03 monolayers (ML) of carbon via X-ray photoemission spectroscopy (XPS). A minimum period of 15 minutes was allowed between annealing and photoemission measurements to ensure sufficient time for surface O_b-vacs to migrate into the sub-surface region [15]. This thermally equilibrated surface will subsequently be referred to as the 'as-prepared surface'. To create surface O_b-vacs non-thermally, the sample was irradiated with electrons from a fully-outgassed electron gun (500-550 eV, 13 μA mm^{-2}). De-ionised water, deliberately dosed into the vacuum chamber, was first cleaned via repeated freeze-pump-thaw cycles.

Measurements employed the ultra-high vacuum and laser systems at UCL described in Sections 3.1.1 and 3.2.1, respectively. 2PPE ($h\nu$ = 3.10-3.54 eV, 400-350 nm, 0.3-0.5 mW, spot diameter $\sim$0.5 mm) and UPS (He-I, $h\nu$ = 21.2 eV, 58 nm and He-II, $h\nu$ = 40.8 eV, 30 nm) spectra were recorded with a pass energy of 10 eV and a bias voltage of -3 V was applied to the sample during the 2PPE measurements. All photoemission spectra were obtained at room temperature, unless otherwise stated. Calibration of the sample E_F was made in reference to that of the Ta sample holder, which was also measured via photoemission.

5.3 Results & Discussion

5.3.1 Water Adsorption at 130 K

Despite receiving considerable attention, the adsorption behaviour of water on TiO_2 surfaces remains controversial. Recently, calculations of the electronic structure of the H_2O/TiO_2(101) interface have been attempted, however, no appropriate experimental works were available for comparison [26]. The as-prepared surface was cooled to $\sim$130 K preceding exposure to gas-phase water in steps of 0.45 L (1 L = 1.33$\times10^{-6}$ mbar s). No alterations were seen in the spectra for exposures above 3.15 L. 2PPE measurements of the H_2O/TiO_2(101) interface evidenced a maximum change in the sample workfunction of -0.9 eV, similar to the value previously obtained via photoemisson from water-covered rutile TiO_2(110) surfaces [27–29]. UPS He-II spectra were recorded following each exposure to water and subsequently normalised to the background of inelastically scattered

photoelectrons. These spectra, shown in Figure 5.2, evidence water-induced modifications in the valence band region and the growth of a feature centred at $\sim$-13 eV for all water exposures.

Figure 5.2b displays difference spectra obtained by subtracting the normalised spectrum from the as-prepared surface from those measured after exposure to water. The difference spectra evidence three main water-induced features, centred 13.16 eV, 9.91 eV and 7.33 eV below E_F, which we associate with the $1b_2$, $3a_1$ and $1b_1$ molecular orbitals of water, respectively. This assignment is made upon comparison with previous photoemission studies of molecular water adsorbed at the rutile TiO_2(110) surface and in the gas-phase [30, 31]. The peak with negative intensity, centred around -5.5 eV in Figure 5.2b, may arise from redistribution and depopulation of the sample's O 2p valence band levels upon hybridisation with the orbitals of chemisorbed water [26, 30].

The difference peaks exhibit no significant change in energy with water exposure. However, the peak associated with the $3a_1$ molecular orbital appears asymmetric in all but the 0.45 L difference spectrum. Shifts in the $3a_1$ molecular orbital peaks are known to arise from hydrogen bonding and other adsorbate-adsorbate interactions, which may explain the dependence of this feature on water coverage [32]. Compared to measurements in the gas-phase [30], the $3a_1$ molecular orbital peak is shifted 0.5 eV away from E_F on the anatase TiO_2(101) surface. This value is similar to the 0.4 eV stabilisation previously measured at the rutile TiO_2(110) surface [30, 31]. The $3a_1$ and $1b_1$ molecular orbitals of water hybridise with the sample's Ti 3d orbitals, making comparison with calculations more complicated. However, the $1b_2$ molecular orbital lies outside the valence band region and therefore does not hybridise with the surface. The position of the $1b_2$ molecular orbital peak in this work agrees well with recent calculations [26].

The spectra presented in Figure 5.2 support the many experimental and theoretical works which suggest that water adsorbs molecularly at the defect-free anatase TiO_2(101) surface [8, 19–22, 33–35]. Importantly, this finding does not exclude the possibility that a mixed monolayer of water and hydroxyls exists at temperatures above 130 K, as has also been suggested [24, 25]. This dissociative behaviour may not be expected at the low temperatures used in our measurements due to the presence of energetic dissociation barriers. Additionally, a small feature, centred 11 eV below E_F, present in the spectrum measured from the as-prepared surface at room temperature is assigned to dissociative adsorption of water at step edges.

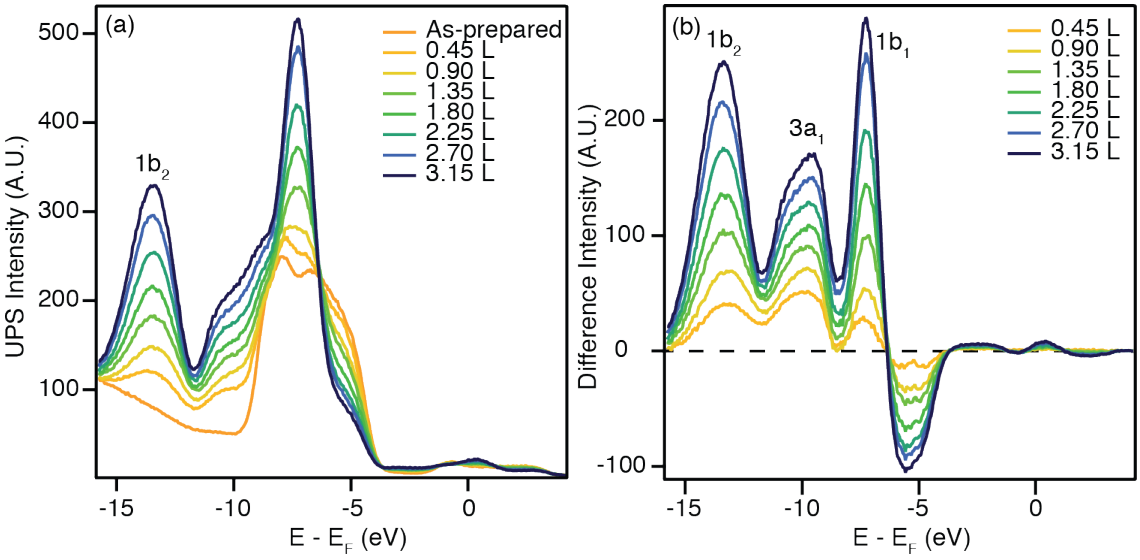

Figure 5.2: (a) UPS spectra ($h\nu$ = 40.8 eV) and (b) difference spectra measured from the as-prepared and water-covered anatase TiO_2(101) surface at 130 K. Water adsorption is seen to modify spectra of the valence band region, leading to the emergence of three main peaks which are associated with the molecular orbitals of water.

5.3.2 Electron Bombardment

Electron bombardment is known to create O_b-vacs at TiO_2 surfaces non-thermally [15, 16]. These point defects are implicated in many of the exotic behaviours of TiO_2 and are therefore of fundamental interest regarding the applications of this metal oxide. The as-prepared surface was irradiated with 500 eV electrons for 2 minutes or 5 minutes prior to the measurement of 2PPE and UPS spectra. 2PPE spectra of the as-prepared surface obtained using 400-350 nm (3.10-3.54 eV) photons are shown in Figure 5.3a. Photoemitted electrons in Figure 5.3 originate from the BGS, since photons below $\sim$320 nm (above 3.9 eV) are required to stimulate 2PPE from the valence band. The workfunction of the as-prepared surface, measured from the low-energy cut-off of the 2PPE spectra, was 4.8 eV, similar to the value of (4.7 $\pm$ 0.1) eV previously reported for the anatase single crystal TiO_2(101) surface [36].

2PPE spectra obtained following bombardment with 500 eV electrons for 2 minutes are displayed in Figure 5.3b. Three main differences are evident in comparison to spectra from the as-prepared surface. Firstly, the sample workfunction is reduced by $\sim$0.2 eV, although quantifying this change is complicated by the appearance of space-charge-induced peaks at the workfunction cut-off. Secondly, a feature appears which is centred 5.5-6.5 eV above E_F, depending on photon

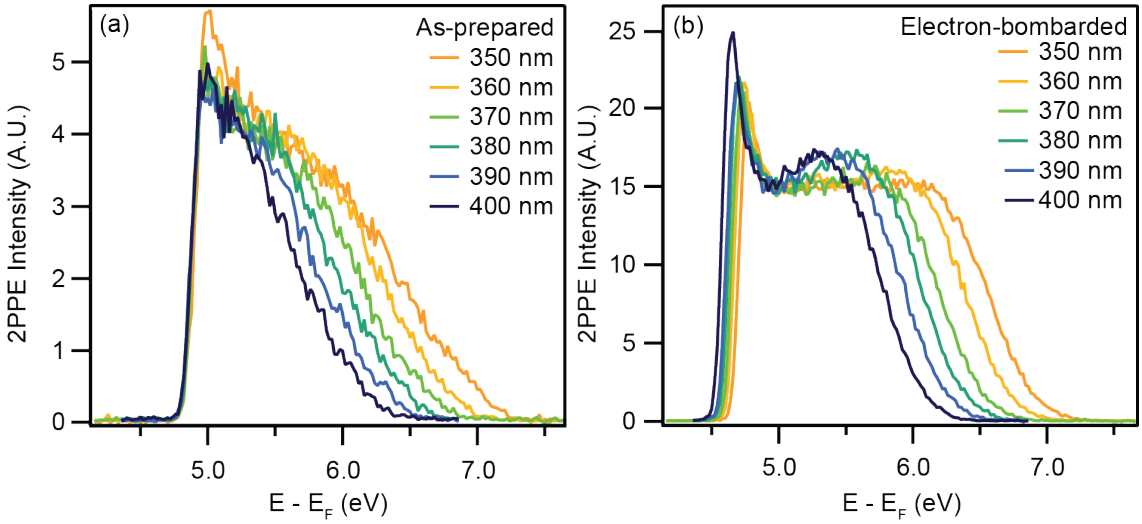

Figure 5.3: 2PPE spectra ($h\nu$ = 3.10-3.54 eV) measured from the (a) as-prepared and (b) electron-bombarded (500 eV, 2 minutes) anatase TiO_2(101) surfaces. The spectra are normalised to the intensity at ~5 eV. Electron bombardment induces a new feature ~5.5-6 eV above E_F and an approximately 0.2 eV reduction in the sample workfunction.

energy. Finally, the 2PPE intensity from the electron-bombarded surface is significantly greater than from the as-prepared surface, as demonstrated by the spectra in Figure 5.4, which have not been normalised. Laser-induced beam damage can be excluded as no change occurred in the 2PPE spectra after irradiation with a high flux of 350 nm photons (0.2 mJ cm^{-2} per pulse) for 60 minutes, compared to the flux used during measurements (0.04 mJ cm^{-2} per pulse). Upon flashing the sample to ~950 K, a 2PPE spectrum was obtained which closely resembles that of the as-prepared surface. This suggests that the effects of electron bombardment on the surface are healed by the heating process.

UPS He-I spectra measured from the as-prepared and electron-bombarded surfaces, normalised to the photoelectron background, are shown in Figure 5.5a. Electron irradiation of the surface induced increases in the photoemission signal relative to the as-prepared surface, centred at energies around 9.4 eV, 4.5 eV and 0.7 eV below E_F. The He-I spectra were fit in the region 3.4 eV below to 0.4 eV above E_F, as described in Chapter 4. The BGS peak appears (0.75 $\pm$ 0.05) eV below E_F, in agreement with previous studies [5, 37]. Following electron bombardment, the area of the BGS peak increased by a factor of 1.50. Accordingly, the changes observed in both 2PPE and UPS spectra are attributed to reduction of the sample via electron irradiation.

Normalised UPS He-II spectra, measured from the same surfaces, are shown in

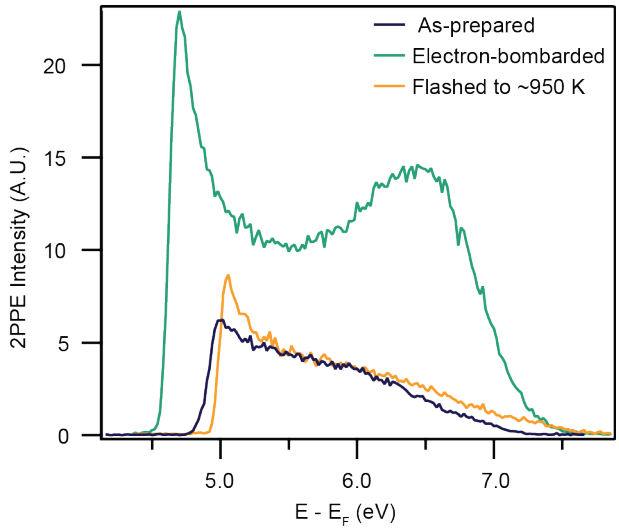

Figure 5.4: 2PPE spectra ($h\nu$ = 3.54 eV) measured from the as-prepared, electron-bombarded (500 eV, 2 minutes) and flashed anatase TiO_2(101) surfaces. The increase of the feature ~6.5 eV above E_F following electron bombardment suggests that the sample is more reduced relative to the as-prepared surface. Subsequent flashing of the sample to ~950 K recovers a spectrum similar to that measured from the as-prepared surface, suggesting that the original surface defect concentration has been recovered.

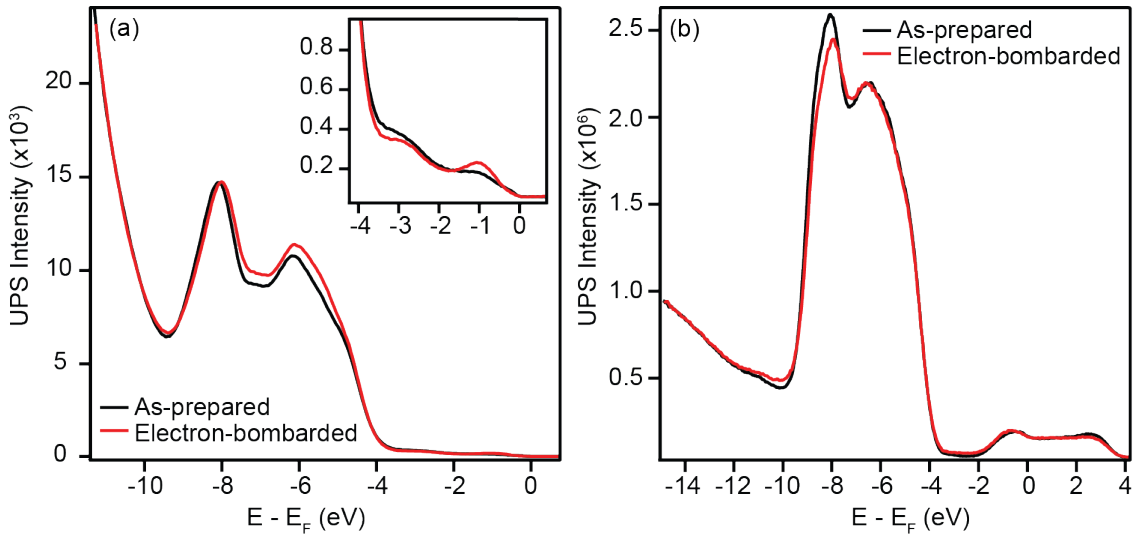

Figure 5.5: UPS spectra measured from the as-prepared (black) and electron-bombarded (red, 500 eV, 2 minutes). (a) He-I ($h\nu$ = 21.2 eV) spectra evidence irradiation-induced modifications in the valence band region and an increase of the BGS peak (see inset). (b) He-II ($h\nu$ = 40.8 eV) spectra also display modifications to the valence band region following electron bombardment.

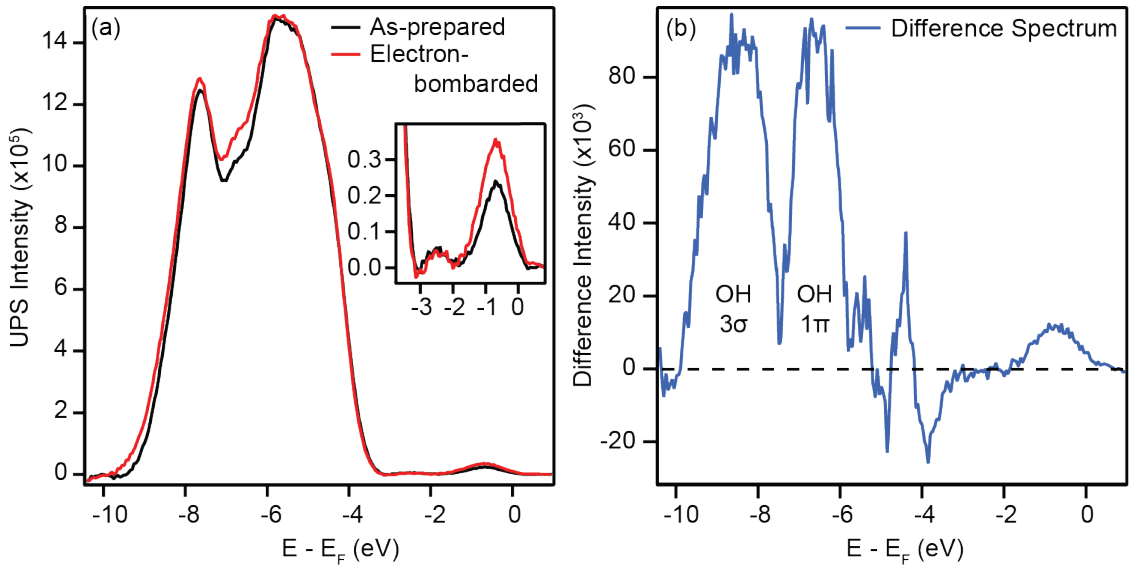

Figure 5.6: (a) UPS He-I ($h\nu$ = 21.2 eV) spectra measured from the as-prepared (black) and electron-bombarded (red, 500 eV, 5 mins) anatase TiO_2(101) surfaces, following background subtraction. (b) The difference spectrum reveals three main peaks associated with the molecular orbitals of OH and an increase in the BGS intensity following electron bombardment.

Figure 5.5b. The spectra reveal new features centred approximately 10.5 eV and 7.2 eV below E_F following electron bombardment. The photoemission signal in the region of -2 eV to 4 eV arises primarily from photoemission from valence band levels, stimulated by the He-II β emission line ($h\nu$ = 48.4 eV), and is therefore not considered. A correction of 0.05 eV was made to both the He-I and He-II spectra of the electron-bombarded surface to correct for band bending away from E_F, induced by the reduction of the surface. Irradiation-induced modifications to the sample's valence band may also influence the background of inelastically scattered electrons. These scattered electrons will make a significantly greater contribution to He-I than He-II spectra. Direct comparisons between He-I and He-II spectra in Figure 5.5 are therefore avoided.

In an attempt to increase the magnitude of the BGS enhancement and modifications in the valence band region, the as-prepared surface was bombarded with 500 eV electrons for a longer time of 5 minutes. The resulting He-I spectra are shown in Figure 5.6a, following normalisation and the subtraction of a fifth order polynomial, intended to remove intensity contributed by the background of scattered photoelectrons. Polarons localised at step edges create states in the band gap, whose energy distribution closely resembles the background present in photoemission measurements [5]. Hence, contributions from these states may be removed during the subtraction of a polynomial background from the UPS spec-

tra in Figure 5.6a. Considering, however, that electron bombardment typically results in point defects rather than step edges, it is unlikely that this process will significantly alter the density of excess electrons trapped at step edges.

Similar to the spectra in Figure 5.5a, electron bombardment of the as-prepared surface increased the BGS peak area by a factor of 1.53. Hence, the BGS peak enhancement did not show a significant dependence on irradiation time. Enhancement of the BGS suggests that it is possible to trap excess electrons at the anatase TiO_2(101) surface at concentrations above the thermally equilibrated level via electron bombardment at room temperature. Furthermore, 2PPE spectra indicate that the equilibrium concentration of excess electrons may be recovered by heating the surface to $\sim$950 K.

The effect of electron bombardment on the He-I spectra maybe be seen more clearly via the difference spectrum in Figure 5.6b. The difference spectrum exhibits two main peaks centred 8.45 eV and 6.50 eV below E_F. Additionally, a minor peak is present 4.4 eV below E_F, which may arise from a change in the gradient of the valence band maximum or slight misalignment of the spectra, to which difference spectra are highly sensitive. The feature $\sim$0.75 eV below E_F is attributed to enhancement of the BGS peak, as previously discussed.

It is known that electron bombardment of TiO_2 results in surface O_b-vacs [15, 16]. The creation of these defects further reduces the surface, which is expected to increase the BGS peak intensity and induce band bending away from E_F. Both these modifications were observed in the UPS spectra, however, as O_b-vacs are mobile at temperatures above $\sim$200 K this effect should not persist long enough to be measured [15]. Additionally, two new features are seen in UPS He-I difference spectra. O_b-vac creation is known to modify the appearance of the valence band in photoemission studies. A feature centred 6.7 eV below E_F in resonant photoemission, similar to that at -6.50 eV in Figure 5.6b, was assigned to hybridisation between the Ti 3d t_{2g} or 4sp orbitals and the O 2p orbitals of the sample [10]. However, the intensity of this feature is attenuated by reduction of the surface, in antithesis to behaviour exhibited by the feature at -6.50 eV in Figure 5.6b. Hence, it is proposed that other contributions may exist in this energy range and that the findings detailed above are not consistent solely with the creation of O_b-vacs.

We propose that the peaks centred 8.45 eV and 6.50 eV below E_F are associated with the 3σ and 1π molecular orbitals of OH, respectively. This OH may be created via dissociative adsorption of gas-phase water molecules in the resid-

ual vacuum at irradiation-induced surface O_b-vacs. Theoretical works predict that this mechanism results in two bridging OH per surface O_b-vac [19, 35]. Concordantly, the position of the OH 3σ molecular orbital peak in Figure 5.6b is in good agreement with DFT calculations [38].

Photoemission studies of hydroxylated rutile TiO_2(110) surfaces evidence peaks 10.8-10.2 eV and 8.0-7.6 eV below E_F, which have been associated with the OH 3σ and 1π molecular orbitals, respectively [30, 31]. The $\sim$2 eV separation between the OH molecular orbital peaks observed for hydroxylated rutile TiO_2(110) agrees particularly well with the peaks shown in Figure 5.6 [31]. It is important to note that the peak centred around 11 eV below E_F in Figure 5.5, which was tentatively assigned to OH adsorbed at step edges, will not contribute intensity to the difference spectrum in Figure 5.6b as this feature is already present in spectra measured from the as-prepared surface.

In comparison to the rutile TiO_2(110) surface, we find that the molecular orbitals of OH on the anatase TiO_2(101) surface are shifted $\sim$1.5 eV towards E_F. The increased proximity of OH 1π levels to the maximum of the sample's valence band may contribute to the increased catalytic activity of anatase over rutile TiO_2, since this increases its ability to trap holes [26]. The OH 1π molecular orbital hybridises with the surface electronic structure upon chemisorption causing significant redistribution of these levels [26, 38].

In addition to the appearance of two new features 8.45 eV and 6.50 eV below E_F, enhancement of the BGS peak area may also be explained via the creation of OH at the surface. Since excess electrons at the anatase TiO_2(101) surface are only capable of localising as polarons at defects, dissociative adsorption of water at surface O_b-vacs may pin these excess electrons to the surface and prevent defect migration into the sub-surface or bulk at room temperature. Recently, DFT calculations have suggested that the nature of polarons at the surfaces of rutile TiO_2 and other metal oxides is independent of their donor defect [39]. Maintaining this assertion, it is likely that polarons at the anatase TiO_2(101) surface are localised in the vicinity of OH, as has been shown for surface O_b-vacs [6]. Accordingly, OH creation may increase the potential for redox reactions to occur by trapping additional excess electrons at the surface, compared to the as-prepared surface. Heating of the hydroxylated surface to 950 K is expected to cause desorption of OH. Indeed, 2PPE spectra measured after heating the sample to this high temperature closely resemble those obtained from the thermally equilibrated, as-prepared surface.

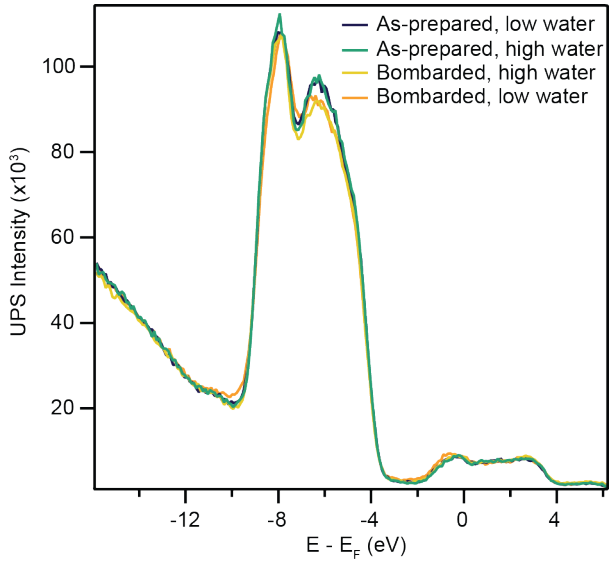

Figure 5.7: UPS spectra ($h\nu$ = 40.8 eV) obtained from the as-prepared and electron-bombarded (550 eV, 3.5 minutes) anatase TiO_2(101) surfaces at high (6.6 $\times$ 10^{-8} mbar) and low ($<$2 $\times$ 10^{-10} mbar) water pressures. Only irradiation at low water pressure resulted in changes to the UPS spectra. The absence of modifications at high water pressure may result from contamination of the water by oxygen, which heals the surface O_b-vacs created by electron bombardment.

Electron Bombardment with Increased Water Exposure

Finally, the as-prepared surface was bombarded by 550 eV electrons for 3.5 minutes, with and without simultaneous exposure to (6.6 $\times$ 10^{-8}) mbar H_2O ($\sim$10.5 L) at room temperature. Mass spectroscopy measurements obtained during exposure of the surface to water revealed that molecular oxygen was also present at a partial pressure of $\leq$(3 $\times$ 10^{-9}) mbar ($\sim$0.5 L). The residual pressure of water without deliberate dosing was estimated to be less than (2 $\times$ 10^{-10}) mbar. He-II spectra measured from the as-prepared and electron-bombarded surfaces with and without water exposure are shown in Figure 5.7. As for previous He-II spectra of the as-prepared surface, the feature $\sim$11 eV below E_F present with and without water exposure is attributed primarily to OH creation at step edges.

The spectrum obtained from the surface electron bombarded at low water pressures exhibits a shoulder about 10 eV below E_F, which is not present in the other spectra. The similarity of the spectrum measured following electron bombardment at greater water pressures to that from the as-prepared surface surface suggests that this process did not significantly alter the surface. In addition, the BGS peak area in the He-I spectrum was not altered by electron bombardment during exposure to 10.5 L of water. Hence, it appears that at greater partial pressure of water

the majority of defects created via electron irradiation are healed, recovering the as-prepared surface. The adsorption of neutral water is not expected to influence the reduction or oxidation level of the surface. Consequently, the most probable explanation for the impotency of electron bombardment at higher water partial pressures is the healing of O_b-vacs and displacement of OH groups by the molecular oxygen, present at a level of $\sim$5 % in mass spectroscopy measurements, as has been observed in studies of the rutile TiO_2(110) surface [40].

5.4 Summary & Conclusion

Photoemission spectroscopy has been used to study the electronic structure of electron-bombarded and water-covered anatase TiO_2(101) surfaces. Water adsorption on the defect-poor anatase TiO_2(101) surface was shown to be predominantly molecular at low temperatures, in agreement with many experimental and theoretical studies [8, 19–22, 33–35]. However, the possibility of a mixed monolayer, consisting of molecular water and OH, is not excluded at higher temperatures. The binding energies of peaks associated with the molecular orbitals of water serve as a useful comparison for theoretical studies, particularly that of the $1b_2$ molecular orbital which does not hybridise with the sample's valence band upon chemisorption. This result also adds credence to the interpretation that modifications to UPS spectra following electron bombardment at room temperature are associated with the molecular orbitals of OH.

The work presented in this chapter verifies the prediction arising from theoretical studies that water adsorbs dissociatively at O_b-vacs at the anatase TiO_2(101) surface [19], which has previously been hindered by the tendency of O_b-vacs to migrate to the sub-surface region at temperatures above $\sim$200 K [15]. Hydroxylation results in the appearance of peaks associated with the 3σ and 1π OH molecular orbitals, which are centred 8.45 eV and 6.50 eV below E_F, respectively. The increased proximity of these peaks to the valence band maximum relative to measurements at the hydroxylated rutile TiO_2(110) surface hints at a possible factor in the increased catalytic activity of anatase over rutile TiO_2, due to an increased propensity towards hole trapping. Photocatalytic TiO_2 surfaces are known to be extensively hydroxylated [41]. This work suggests that the increased concentration of excess electrons at the hydroxylated relative to the as-prepared surface may confer catalytic benefits.

Further work on this topic may attempt to explore the catalytic function of anatase TiO_2. Photodissociation of adsorbed molecules such as alcohols or acids may be studied by time- and energy-resolved 2PPE to determine the energetics and dynamics of this process. Furthermore, comparisons with studies of the minority (001) surface, which is proposed to be more catalytically active [20, 42, 43], may provide insight into the true nature of the catalytic interface.

References

[1] D. T. Payne, Y. Zhang, C. L. Pang, H. H. Fielding, and G. Thornton, "Creating Excess Electrons at the Anatase TiO_2(101) Surface," *Topics in Catalysis*, vol. 2, no. 101, 2016.

[2] U. Diebold, "The surface science of titanium dioxide," *Surface Science Reports*, vol. 48, no. 5-8, pp. 53–229, 2003.

[3] H. Cheng and A. Selloni, "Energetics and diffusion of intrinsic surface and subsurface defects on anatase TiO_2(101)," *The Journal of Chemical Physics*, vol. 131, no. 5, p. 054703, 2009.

[4] I. Austin and N. Mott, "Polarons in crystalline and non-crystalline materials," *Advances in Physics*, vol. 18, no. 71, pp. 41–102, 1969.

[5] M. Setvin, X. Hao, B. Daniel, J. Pavelec, Z. Novotny, G. S. Parkinson, M. Schmid, G. Kresse, C. Franchini, and U. Diebold, "Charge Trapping at the Step Edges of TiO_2 Anatase (101)," *Angewandte Chemie International Edition*, vol. 53, no. 18, pp. 4714–4716, 2014.

[6] M. Setvin, C. Franchini, X. Hao, M. Schmid, A. Janotti, M. Kaltak, C. G. Van de Walle, G. Kresse, and U. Diebold, "Direct View at Excess Electrons in TiO_2 Rutile and Anatase," *Physical Review Letters*, vol. 113, no. 8, p. 086402, 2014.

[7] M. A. Henderson, "A surface science perspective on TiO_2 photocatalysis," *Surface Science Reports*, vol. 66, no. 6-7, pp. 185–297, 2011.

[8] Y. He, O. Dulub, H. Cheng, A. Selloni, and U. Diebold, "Evidence for the Predominance of Subsurface Defects on Reduced Anatase TiO_2(110)," *Physical Review Letters*, vol. 102, no. 10, p. 106105, 2009.

[9] L. Kavan, M. Grätzel, S. E. Gilbert, C. Klemenz, and H. J. Scheel, "Electrochemical and Photoelectrochemical Investigation of Single-Crystal Anatase,"

Journal of the American Chemical Society, vol. 118, no. 28, pp. 6716–6723, 1996.

[10] A. G. Thomas, W. R. Flavell, A. K. Mallick, A. R. Kumarasinghe, D. Tsoutsou, N. Khan, C. Chatwin, S. Rayner, G. C. Smith, R. L. Stockbauer, S. Warren, T. K. Johal, S. Patel, D. Holland, A. Taleb, and F. Wiame, "Comparison of the electronic structure of anatase and rutile TiO_2 single-crystal surfaces using resonant photoemission and x-ray absorption spectroscopy," *Physical Review B*, vol. 75, no. 3, p. 035105, 2007.

[11] R. Sanjines, H. Tang, H. Berger, F. Gozzo, G. Margaritondo, and F. Levy, "Electronic structure of anatase TiO_2 oxide," *Journal of Applied Physics*, vol. 75, no. 6, p. 2945, 1994.

[12] A. C. Papageorgiou, N. S. Beglitis, C. L. Pang, G. Teobaldi, G. Cabailh, Q. Chen, A. J. Fisher, W. A. Hofer, and G. Thornton, "Electron traps and their effect on the surface chemistry of TiO_2(110)," *Proceedings of the National Academy of Sciences of the United States of America*, vol. 107, no. 6, pp. 2391–2396, 2010.

[13] C. Di Valentin, G. Pacchioni, and A. Selloni, "Reduced and n-Type Doped TiO_2: Nature of Ti^{3+} Species," *The Journal of Physical Chemistry C*, vol. 113, no. 48, pp. 20543–20552, 2009.

[14] M. Chiesa, M. C. Paganini, S. Livraghi, and E. Giamello, "Charge trapping in TiO_2 polymorphs as seen by Electron Paramagnetic Resonance spectroscopy," *Physical Chemistry Chemical Physics*, vol. 15, no. 24, p. 9435, 2013.

[15] P. Scheiber, M. Fidler, O. Dulub, M. Schmid, U. Diebold, W. Hou, U. Aschauer, and A. Selloni, "(Sub)Surface Mobility of Oxygen Vacancies at the TiO_2 Anatase (101) Surface," *Physical Review Letters*, vol. 109, no. 13, p. 136103, 2012.

[16] M. Setvin, M. Buchholz, W. Hou, C. Zhang, B. Stöger, J. Hulva, T. Simschitz, X. Shi, J. Pavelec, G. S. Parkinson, M. Xu, Y. Wang, M. Schmid, C. Wöll, A. Selloni, and U. Diebold, "A Multitechnique Study of CO Adsorption on the TiO_2 Anatase (101) Surface," *The Journal of Physical Chemistry C*, vol. 119, no. 36, pp. 21044–21052, 2015.

[17] M. Setvin, U. Aschauer, P. Scheiber, Y. Li, W. Hou, M. Schmid, A. Selloni, and U. Diebold, "Reaction of O_2 with Subsurface Oxygen Vacancies on TiO_2 Anatase (101)," *Science*, vol. 341, no. 6149, pp. 988–991, 2013.

[18] C. L. Pang, R. Lindsay, and G. Thornton, "Structure of Clean and Adsorbate-Covered Single-Crystal Rutile TiO_2 Surfaces," *Chemical Reviews*, vol. 113, no. 6, pp. 3887–3948, 2013.

[19] A. Tilocca and A. Selloni, "Structure and Reactivity of Water Layers on Defect-Free and Defective Anatase TiO_2(101) Surfaces," *The Journal of Physical Chemistry B*, vol. 108, no. 15, pp. 4743–4751, 2004.

[20] A. Vittadini, A. Selloni, F. P. Rotzinger, and M. Grätzel, "Structure and Energetics of Water Adsorbed at TiO_2 Anatase (101) and (001) Surfaces," *Physical Review Letters*, vol. 81, no. 14, pp. 2954–2957, 1998.

[21] G. S. Herman, Z. Dohnálek, N. Ruzycki, and U. Diebold, "Experimental Investigation of the Interaction of Water and Methanol with Anatase-TiO_2(101)," *The Journal of Physical Chemistry B*, vol. 107, no. 12, pp. 2788–2795, 2003.

[22] U. Aschauer, Y. He, H. Cheng, S.-C. Li, U. Diebold, and A. Selloni, "Influence of Subsurface Defects on the Surface Reactivity of TiO_2: Water on Anatase (101)," *The Journal of Physical Chemistry C*, vol. 114, no. 2, pp. 1278–1284, 2010.

[23] A. Tilocca and A. Selloni, "Vertical and Lateral Order in Adsorbed Water Layers on Anatase TiO_2(101)," *Langmuir*, vol. 20, no. 19, pp. 8379–8384, 2004.

[24] L. E. Walle, A. Borg, E. M. J. Johansson, S. Plogmaker, H. Rensmo, P. Uvdal, and A. Sandell, "Mixed Dissociative and Molecular Water Adsorption on Anatase TiO_2(101)," *The Journal of Physical Chemistry C*, vol. 115, no. 19, pp. 9545–9550, 2011.

[25] C. E. Patrick and F. Giustino, "Structure of a Water Monolayer on the Anatase TiO_2(101) Surface," *Physical Review Applied*, vol. 2, no. 1, p. 014001, 2014.

[26] H. Sun, D. J. Mowbray, A. Migani, J. Zhao, H. Petek, and A. Rubio, "Comparing Quasiparticle H_2O Level Alignment on Anatase and Rutile TiO_2," *ACS Catalysis*, vol. 5, no. 7, pp. 4242–4254, 2015.

[27] M. B. Hugenschmidt, L. Gamble, and C. T. Campbell, "The interaction of H_2O with a TiO_2(110) surface," *Surface Science*, vol. 302, no. 3, pp. 329–340, 1994.

[28] K. Onda, B. Li, and H. Petek, "Two-photon photoemission spectroscopy of TiO_2(110) surfaces modified by defects modified by O_2 or H_2O adsorbates," *Physical Review B*, vol. 70, no. 4, p. 045415, 2004.

[29] D. T. Payne, Y. Zhang, C. L. Pang, H. H. Fielding, and G. Thornton, "Coverage-dependent two-photon photoexcitation at the H_2O/TiO_2 interface," *Surface Science*, vol. 652, pp. 189–194, 2016.

[30] R. L. Kurtz, R. Stock-Bauer, T. E. Madey, E. Román, and J. De Segovia, "Synchrotron radiation studies of H_2O adsorption on TiO_2(110)," *Surface Science*, vol. 218, no. 1, pp. 178–200, 1989.

[31] I. M. Brookes, C. A. Muryn, and G. Thornton, "Imaging Water Dissociation on TiO_2(110)," *Physical Review Letters*, vol. 87, no. 26, p. 266103, 2001.

[32] M. Henderson, "The interaction of water with solid surfaces: fundamental aspects revisited," *Surface Science Reports*, vol. 46, no. 1-8, pp. 1–308, 2002.

[33] M. J. Jackman, A. G. Thomas, and C. Muryn, "Photoelectron Spectroscopy Study of Stoichiometric and Reduced Anatase TiO_2(101) Surfaces: The Effect of Subsurface Defects on Water Adsorption at Near-Ambient Pressures," *The Journal of Physical Chemistry C*, vol. 119, no. 24, pp. 13682–13690, 2015.

[34] J. Fan, J. Z. Zhao, H. Xu, and S. Y. Tong, "Comment on "Interplay between Water and TiO_2 Anatase (101) Surface with Subsurface Oxygen Vacancy"," *Physical Review Letters*, vol. 115, no. 14, p. 149601, 2015.

[35] A. Tilocca and A. Selloni, "Reaction pathway and free energy barrier for defect-induced water dissociation on the (101) surface of TiO_2-anatase," *The Journal of Chemical Physics*, vol. 119, no. 14, p. 7445, 2003.

[36] A. R. Kumarasinghe, W. R. Flavell, A. G. Thomas, A. K. Mallick, D. Tsoutsou, C. Chatwin, S. Rayner, P. Kirkham, S. Warren, S. Patel, P. Christian, P. O'Brien, M. Gratzel, and R. Hengerer, "Electronic properties of the interface between p-CuI and anatase-phase n-TiO_2 single crystal and nanoparticulate surfaces: A photoemission study," *The Journal of Chemical Physics*, vol. 127, no. 11, p. 114703, 2007.

[37] M. Jackman, P. Deák, and K. Syres, "Observation of vacancy-related polaron states at the surface of anatase and rutile TiO_2 by high-resolution photoelectron spectroscopy," *http://arxiv.org/abs/1406.3385*, 2014.

[38] Z. Zhao, Z. Li, and Z. Zou, "Water Adsorption and Decomposition on N/V-Doped Anatase TiO_2(101) Surfaces," *The Journal of Physical Chemistry C*, vol. 117, no. 12, pp. 6172–6184, 2013.

[39] P. G. Moses, A. Janotti, C. Franchini, G. Kresse, and C. G. Van de Walle, "Donor defects and small polarons on the TiO_2(110) surface," *Journal of Applied Physics*, vol. 119, no. 18, p. 181503, 2016.

[40] S. Wendt, P. T. Sprunger, E. Lira, G. K. H. Madsen, Z. Li, J. O. Hansen, J. Matthiesen, A. Blekinge-Rasmussen, E. Laegsgaard, B. Hammer, and F. Besenbacher, "The Role of Interstitial Sites in the Ti3d Defect State in the Band Gap of Titania," *Science*, vol. 320, no. 5884, pp. 1755–1759, 2008.

[41] K. I. Hadjiivanov and D. G. Klissurski, "Surface chemistry of titania (anatase) and titania-supported catalysts," *Chemical Society Reviews*, vol. 25, no. 1, p. 61, 1996.

[42] M. Lazzeri, A. Vittadini, and A. Selloni, "Structure and energetics of stoichiometric TiO_2 anatase surfaces," *Physical Review B*, vol. 63, no. 15, p. 155409, 2001.

[43] A. Vittadini, M. Casarin, and A. Selloni, "Chemistry of and on TiO_2-anatase surfaces by DFT calculations: a partial review," *Theoretical Chemistry Accounts*, vol. 117, no. 5, pp. 663–671, 2007.

Chapter 6

Ultra-fast Dynamics of Charge Trapping and Recombination in Rutile TiO_2

Abstract

The trapping and recombination of excited charge carriers in titanium dioxide (TiO_2) are key processes which underpin the application of this material to heterogeneous catalysis and photochemistry. However, the ultra-fast dynamics of these fundamental processes have not yet been characterised at well-defined single crystal TiO_2 surfaces. This chapter presents femtosecond-resolved, extreme ultra-violet photoemission measurements of the reduced rutile TiO_2(110) surface following excitation by infra-red (IR, $h\nu$ = 0.95 eV) and ultra-violet (UV, $h\nu$ = 3.54 eV) photons. From IR-pumped measurements, a period of (43 $\pm$ 8) fs was obtained for the trapping of conduction band electrons as polarons. A trapping mechanism involving interaction with the longitudinal optical phonon mode is proposed due to the coincidence of the trapping time with the period of this phonon mode. Under UV irradiation, an additional spectral component is assigned to electron-hole recombination on the pico- to nanosecond timescale. Depletion of the polaronic, Ti 3d band gap states at these late times is attributed to trap-assisted recombination processes, suggesting that the population of excited electrons and holes in TiO_2 is influenced by the presence of intrinsic defects and trapped electrons.

6.1 Introduction

The application of metal oxides as electronic devices and catalysts must consider the nature of charge transfer within these materials. In transition metal oxides, such as titanium dioxide (TiO_2), the interaction between phonons and excess electrons is particularly strong and hence influences the behaviour of these charge carriers [1]. If the interaction is sufficiently strong, the excess electron may localise as an electron-phonon quasiparticle, known as a polaron since this phenomenon locally polarises the lattice of ionic crystals. Depending upon their degree of localisation, polarons may be referred to generally as large or small, although in reality a continuum of spatial distributions exists [2]. In stoichiometric anatase TiO_2 single crystals, excess electrons favour a free-carrier state and do not form small polarons [3]. The band-like transfer of excess electrons makes anatase TiO_2 well suited to use as the electrode of photoelectrochemical solar cells. Conversely, the greater localisation of polarons at rutile TiO_2 surfaces is believed to facilitate efficient charge transfer to catalysed species [4]. The trapping of charge carriers is known to influence the optical absorption [5], thermoelectric [6] and charge transport [7] properties of TiO_2. Consequently, a precise understanding of the behaviour of charge carriers is required when considering the application of TiO_2.

Reduction of rutile TiO_2 results in an n-type semiconductor with a band-gap of 3.0 eV [8]. The excess electrons resulting from this reduction are known to form polaronic states in the semiconductor's band gap, localised near Ti sites [3]. As previously described, these band gap states (BGS) are known to modify the physical properties of the material and have consequently been the focus of many experimental and theoretical studies [1–3, 9, 10]. The exact extent of polaron localisation at the rutile TiO_2(110) surface has not been agreed upon, partly owing to differences in theoretical methods (see Section 4.1). However, the experimental consensus is that excess electrons become trapped as small or intermediate-sized polarons, rather than maintaining a free-carrier-like character [2, 3]. In other words, the polaron radius is smaller than or comparable to the interatomic spacing of the crystal lattice [1].

The energy required to lift electrons from the polaronic BGS to the conduction band minimum may be viewed as a combination of the polaron binding energy and the energy required to distort the crystal lattice [1]. The techniques of infrared (IR) absorption and electron energy loss (EELS) spectroscopies are capable

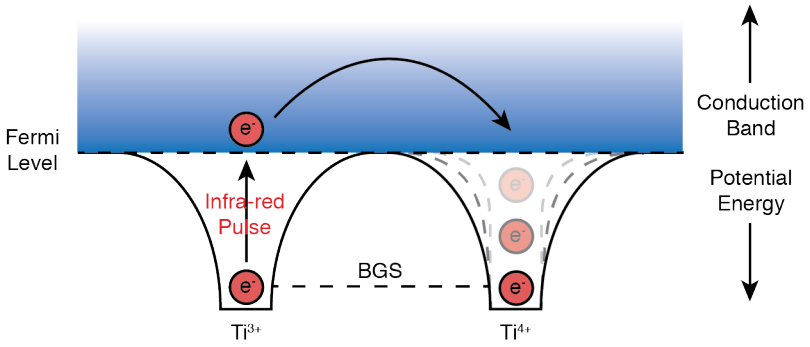

Figure 6.1: Schematic of the photon-assisted polaron hopping mechanism in rutile TiO_2. A BGS electron, localised at a Ti^{3+} ion, is freed from the polaronic trap via absorption of an infra-red photon and excited to the conduction band minimum. At a given time delay, the electron relaxes via interaction with a phonon and repopulates the BGS.

of measuring both these energy contributions and evidence features at an energy of 0.8 eV in measurements of reduced TiO_2 [9, 11–14]. A feature pertaining to the BGS is also observed in photoemission spectroscopy (PES) data at similar energies [15]. Since the binding energy of the BGS peak in PES relies solely on the lattice distortion energy, the coincidence of the energies observed in PES and IR absorption or EELS measurements indicates that the polaron binding energy at the rutile TiO_2(110) surface is small. Indeed, the binding energy of the polaron is believed to be as little as 0.1 eV [10, 16–18]. The intensity of the BGS feature correlates positively with the conductivity of TiO_2 [1], indicating that even small polarons are mobile within the crystal lattice. The most prominent mode of charge transfer at ambient temperatures is polaron hopping, which occurs via energy transfer between the electron and phonon modes. Photon-assisted polaron hopping also occurs, so long as the photon energy is sufficient to promote the electron into the conduction band. A schematic of the photon-assisted polaron hopping process in rutile TiO_2 is shown in Figure 6.1.

This chapter presents time- and energy-resolved photoemission measurements from the reduced rutile TiO_2(110) single crystal surface. Firstly, photoexcitation from the BGS to the conduction band minimum is achieved using a pump photon energy of 0.95 eV (1300 nm) and is probed by extreme ultra violet (XUV) pulses. Secondly, ultra-violet (UV) pump pulses are employed to excite both BGS and valence band electrons to conduction band levels. The temporal dependence of the depletion and accumulation signals give an insight into the properties of polarons in this metal oxide.

6.2 Experimental Procedure

Experiments were carried out at the Artemis facility of the Rutherford Appleton Laboratory (RAL) and employed the vacuum chamber and laser system described in Sections 3.1.2 & 3.2.2, respectively. A reduced rutile TiO_2(110) single crystal sample was prepared by Ar^+ sputtering (1 kV, 1μA cm^{-2}, 15 minutes) and subsequently transferred to the main chamber with a base pressure of 2 $\times$ 10^{-10} mbar, where it was annealed (1100 K, 5 minutes). The sample cleanliness and long-range surface order were verified by Auger electron spectroscopy (AES) and low-energy electron diffraction (LEED), respectively. A period of $\sim$30 minutes was allowed between thermal annealing and data acquisition, during which the sample surface was expected to hydroxylate according to the known adsorption behaviour of water [19].

An ultra-fast XUV pulse ($h\nu$ $\sim$30 eV, $\sim$40 nm, $\sim$30-45 fs pulse width, 10^8 photons per pulse) was employed to probe the sample's electronic structure. Time-resolved measurements employed either IR (0.95 eV, 1300 nm) or UV (3.54 eV, 350 nm) pulses to pump the system, with a variable temporal delay between the pump and XUV probe pulses. The laser spot size at the sample was approximately 0.1 mm in diameter. The power of the IR and UV pulses were 2.0 mW and 1.7 mW, respectively, corresponding to fluences of 2.4 mJ cm^{-2} and 2.1 mJ cm^{-2}. Both pump pulses were s-polarised and the plane of incidence was parallel to the surface [001] direction, with an incident angle of 45° from the surface normal.

Photoelectrons were analysed by a hemispherical electron analyser (*Phoibos 100 SPECS*) in normal emission geometry. Space charge effects from the incident laser pulse resulted in a broadening of about 0.4 eV and a shift of $\sim$120 meV towards the Fermi level (E_F). Hence, the total energy resolution of the experiment was estimated to be 0.7 eV by fitting static photoemission measurements of the polycrystalline Ta sample holder E_F. This quantity includes contributions from space charge and instrumental broadening effects. Similarly, the binding energy scale of the photoemission spectra was calibrated from photoemission measurements of the Ta sample holder. The time-resolution of the experiment was estimated to be about 15 fs, from the uncertainty in identifying a pump-probe delay of 0 fs. This was achieved by fitting the temporal evolution of the photoemission spectra (0.6 $\pm$ 0.2) eV above E_F for the IR and UV experiments separately. The pump-probe delay times referred to in this chapter are quoted relative to the results of this fitting procedure.

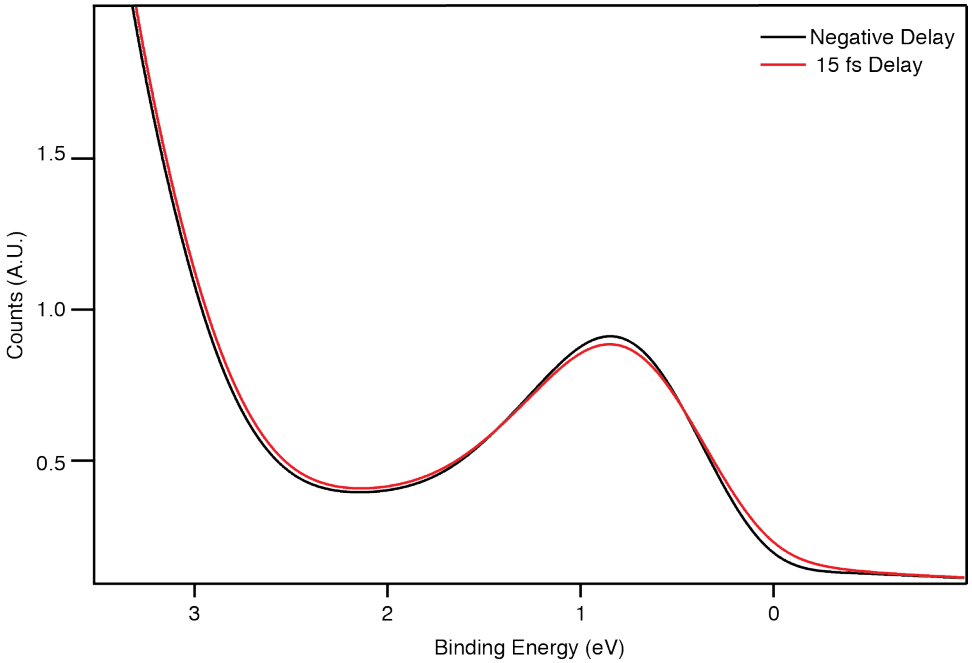

Figure 6.2: Photoemission spectra measured from the reduced rutile TiO_2(110) surface using ∼30 eV XUV photons. The spectrum measured at negative delay times (black) represents the ground state electronic structure of the surface. In comparison, the spectrum measured 15 fs after irradiation (red) by a 0.95 eV IR pulse evidences depletion of the BGS (0.8 eV) and the accumulation of electrons at E_F. Additionally, a shift of about 20 meV is attributed to a surface photovoltage effect.

6.3 Results & Discussion

6.3.1 Infra-red Pump Experiment

Energy-resolved photoemission spectra, acquired at negative (black) and 15 fs (red) pump-probe delays, are shown in Figure 6.2. At negative delay times, the spectrum represents the ground state electronic structure of the system. This spectrum was obtained from the average of three individual spectra, measured between -135 fs and -85 fs pump-probe delay. A broad peak, centred at 0.8 eV, in the negative delay spectrum is assigned to the BGS and the onset of the valence band is evident at ∼3 eV. By comparison, the spectrum measured at 15 fs delay demonstrates depletion of the BGS peak maximum and accumulation of electrons around E_F. These changes are attributed to the pumping of electrons from the BGS to the conduction band by the IR pump pulse. An additional difference between these spectra is that the onset of the valence band is shifted by ∼22 meV to lower energy in the 15 fs delay spectrum. This shift results in a feature with

positive intensity above ~2.5 eV (dashed box) in the difference spectra displayed in Figure 6.3a, which were obtained by subtracting the negative delay spectrum from spectra measured at various pump-probe delay times.

The boxed feature in Figure 6.3a persists to long positive delay times (at least about 2 ps), but is not expected to occur from pumping of the system with IR photons. This is because accumulation of electrons in the valence band region is not possible since these states are below E_F. Instead, the shift of the spectra at positive delay times may be explained by the surface photovoltage (SPV) effect [20], which has previously been observed in pump-probe measurements of semiconductor surfaces [21], including TiO_2 [22]. The SPV effect originates from a change in the electronic field at the surface and is associated with the creation of free charge carriers. These free charge carriers may arise from the creation of electron-hole pairs through band-to-band transitions or via the release of trapped carriers through trap-to-band transitions [20, 23]. Band-to-band transitions dominate if the incident photon energy is above the bandgap of the material [20, 23]. In this case, minority charge carriers created via super-bandgap photoexcitation migrate to the sample surface and reduce the intrinsic band-bending [24]. This results in a shift of the surface electronic structure.

The IR photon energy employed in these measurements is much less than the bandgap of TiO_2 and hence band-to-band transitions are unlikely to occur. Instead, the observed SPV shift is attributed to trap-to-band transitions associated with the liberation of excess electrons from the polaronic BGS. In reduced TiO_2, the band structure is bent downwards by the presence of excess electrons. Hence, the SPV effect results in a shift of the spectra towards E_F. SPV shifts persisting to nanosecond timescales have previously been observed at the rutile TiO_2(110) surface [22, 25].

To compensate for the SPV effect, a shift to higher binding energies is applied to the spectra and their respective difference spectra recalculated. The magnitude of these shifts are shown in Figure 6.4. The difference spectra calculated following SPV correction are shown in Figure 6.3b. The correction procedure successfully removes the positive feature at $\geq$2.5 eV, producing spectra which are flat in this energy range. Additionally, the long-lived feature at E_F in Figure 6.3a is removed, which is also believed to arise from the SPV effect. Following correction for the SPV effect, the depletion and accumulation signals correlate temporally, permitting the true dynamics of polaron trapping to be determined.

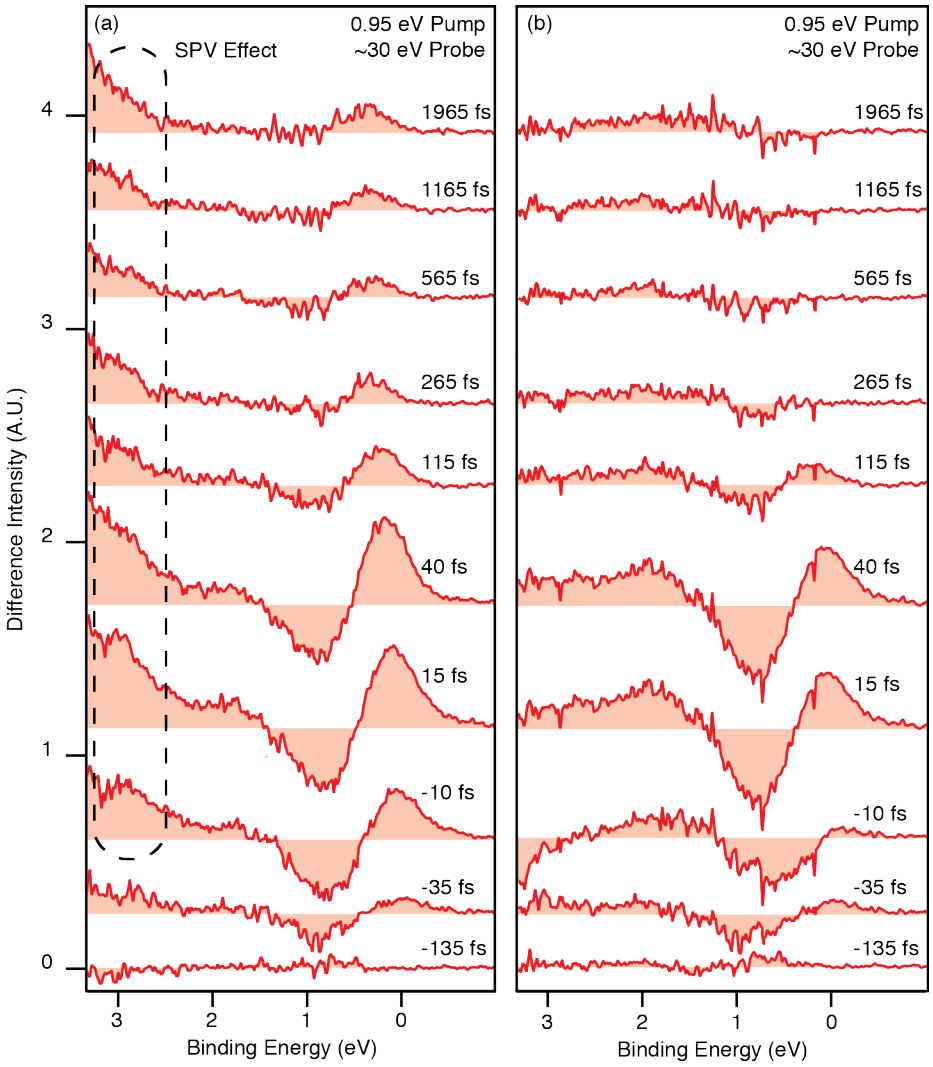

Figure 6.3: Difference spectra obtained by subtracting the negative delay spectrum in Figure 6.2 (black) from spectra measured at various delay times. (a) Difference spectra prior to correcting for the SPV effect exhibit a feature above about 2.5 eV (dashed-box) which is attributed to a shift of the spectra to lower energies. (b) Subsequent to the SPV correction, the feature at high energies is removed and the dynamics of the BGS and E_F regions correlate temporally.

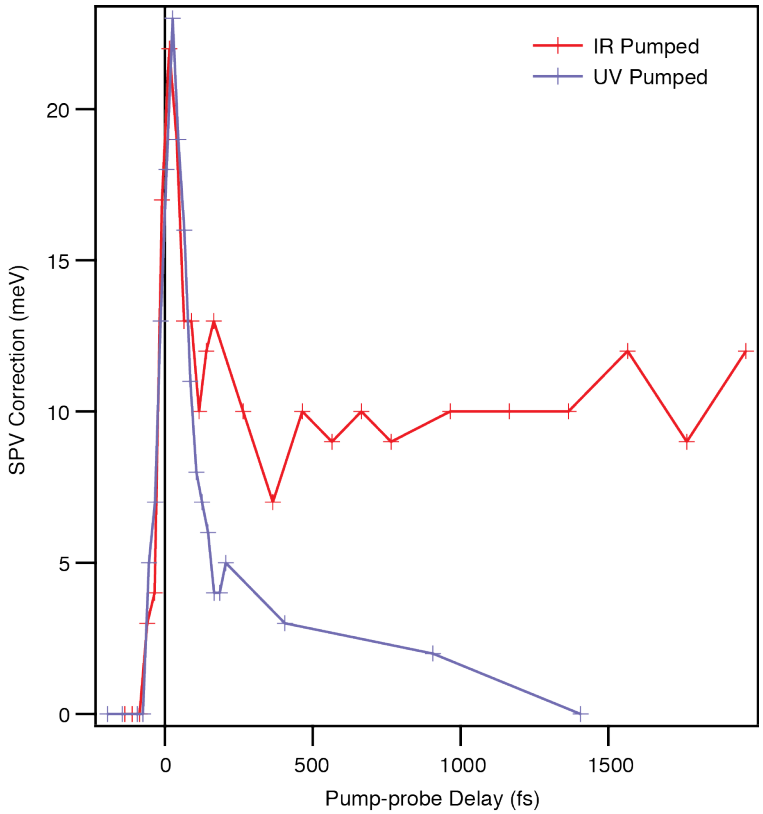

Figure 6.4: Magnitude of the energy shift away from E_F applied to each spectrum in order to correct for the influence of the surface photovoltage effect. Shifts applied to the IR- (0.95 eV) and UV-pumped (3.54 eV) spectra are shown in red and blue, respectively.

In order to accurately determine the dynamics of the BGS and at E_F, the duration of the laser pulse cross-correlation must be obtained. This was achieved by fitting the temporal evolution of the hot electrons, centred 0.6 eV above E_F. The width of the integration window was 0.4 eV. In this spectral region, the excited state lifetime is expected to be sufficiently small but the time-dependency of the signal is non-zero. The resulting spectrum, shown in Figure 6.5 (red crosses), evidences a peak at small delay times and negligible intensity at greater delays. The spectrum was fit by a convolution of Gaussian and exponential decay lineshapes, which represent the laser pulse duration and excited state lifetime, respectively. *Ab initio* calculations predict that the time taken for an excited electron to relax to the conduction band minimum from states 0.6 eV above E_F is $\sim$10 fs [26]. Hence, a value of 10 fs was used for the decay constant of the exponential lineshape in the fitting procedure. The resulting fit, shown in Figure 6.5 (dark-blue curve), gives a width of (21 $\pm$ 5) fs for the Gaussian component, where the Gaussian width is defined as one standard deviation from the mean.The uncertainty in identifying the zero pump-probe delay time was $\pm$7 fs. The uncertainty in these parameters was given by their variation when the exponential decay parameter was varied between 5 fs and 20 fs, which were taken as upper and lower limits for the excited state lifetime on the basis of *ab initio* calculations [26].

Subsequently, the dynamics of the BGS and E_F regions may be analysed. Photoexcitation from the BGS to the conduction band is approximated to a simple two-level system, since the energy resolution of the measurement (0.7 eV) is larger than the width of the integration window (0.4 eV). Invoking the principle of charge conservation permits the depletion and accumulation signals to be described by a single lineshape and hence decreases uncertainty associated with the fit parameters. The time-dependence of the BGS (green, 0.8 eV) and E_F (dark-blue, 0.0 eV) regions are shown in Figure 6.6. The inset displays these two spectra as positive signals for ease of comparison. The difference of about 20% in the intensity of these signals is attributed to their sensitivity to the magnitude of the SPV correction and integration window, but does not significantly affect the lifetime extracted by the fitting procedure. Additionally, the BGS signal appears noisier than that from E_F, which is attributed to the greater intensity of background electrons in this energy region.

Using the laser cross-correlation extracted from the fitting of the hot electron signal in Figure 6.5, a lifetime of (43 $\pm$ 8) fs is obtained for electron trapping from the conduction band minimum. The uncertainty associated with this result arises partly from the confidence of the fitting procedure and the uncertainty in identify-

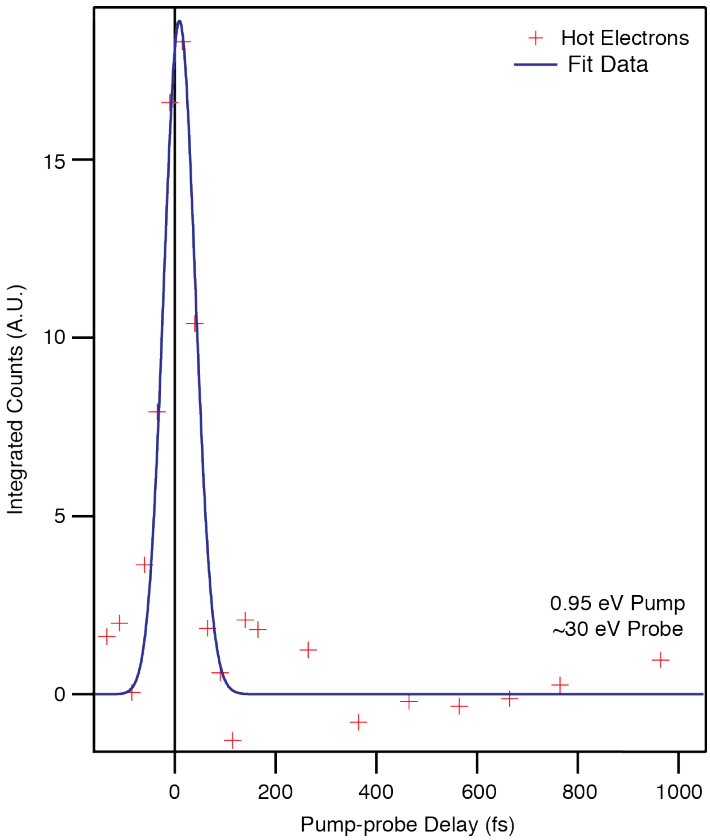

Figure 6.5: Temporal evolution of the integrated hot electron signal, centred 0.6 eV above E_F. The width of the integration window was 0.4 eV. The spectrum (red crosses) exhibits a peak approximately centred at the 0 pump-probe delay position. The data is fit by the convolution of a Gaussian and exponential decay lineshapes (dark-blue curve), representing the cross-correlation of the laser pules and the lifetime of the excited states, respectively. A value of (21 $\pm$ 5) fs was obtained for the Gaussian width, which is defined as one standard deviation from the mean. The uncertainty in identifying the zero pump-probe delay time was $\pm$7 fs.

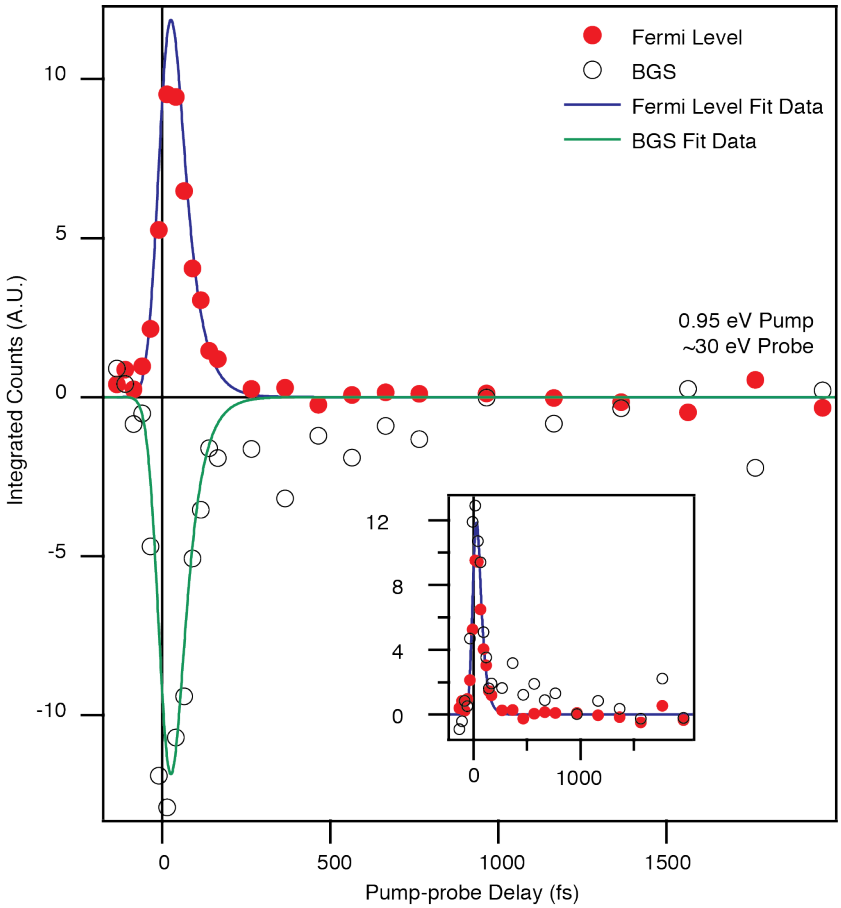

Figure 6.6: Temporal evolution of the integrated BGS (black rings) and E_F (red circles) signal intensity, centred at 0.8 eV and 0.0 eV, respectively. The width of the integration window was 0.4 eV. These spectra were fit simultaneously in order to reduce uncertainty in the extracted lifetime by assuming conservation of charge between the two energy regions. The inset displays both spectra as positive signals for ease of comparison. The value of (43 $\pm$ 8) fs obtained for the decay of electrons from E_F to the BGS coincides with the period of the LO phonon mode, which is expected to dominate polaron formation at ambient temperatures [2].

ing the zero pump-probe delay time. In TiO_2, the longitudinal optical (LO) phonon mode is expected to dominate polaron formation at ambient temperatures [2]. For the rutile phase, the energy of the LO phonon mode has been determined experimentally to be between 98.7 meV and 100.6 meV [2, 27–29], which corresponds to a period of $\sim$42 fs. The period agrees well with the (43 $\pm$ 8) fs obtained for the decay of electrons at E_F into the polaronic BGS. Hence, it is likely that excited electrons at the conduction band minimum of rutile TiO_2 become trapped as polarons within a timescale of about 40 fs via interaction with the LO phonon mode.

6.3.2 Ultra-violet Pump Experiment

In the second experiment, UV photons with an energy of 3.5 eV are employed as the pump laser pulse. As the pump photon energy is above the band gap of rutile TiO_2, photoexcitation from the valence band to the conduction band is expected to result in accumulation of electrons at E_F. Additionally, the pump photon energy matches the resonance between the BGS and the unoccupied Ti 3d conduction band levels, as described in Chapter 4. This process may also result in electron accumulation at E_F if the electrons residing in the unoccupied state decay to the conduction band minimum. Figure 6.7 displays photoemission spectra of the BGS and valence band maximum, acquired at negative (black) and 5 fs (red) pump-probe delays. The negative delay signal was calculated from the average of four individual measurements at pump-probe delays between -195 fs and -75 fs. In comparison to the negative delay spectrum, depletion of the BGS intensity and accumulation of electrons at E_F is evident in the 5 fs delay spectrum. However, the expected depletion of the valence band is obscured by the SPV effect. Since the UV photon energy is greater than the material's bandgap, the SPV-induced shift likely arises primarily from the creation of minority charge carriers via band-to-band transitions [20, 23].

Correcting for the SPV-induced shift of the spectra is more complicated for UV than IR pump energies, given that the valence band may not be used as a reference since these levels are also pumped by the higher photon energy. Due to the high intensity of the valence band, the gradient of the photoemission spectra at the valence band maximum is high and therefore relatively more sensitive to shifts in energy than changes in spectral intensity. Hence, this region of the spectra was chosen to assess the magnitude of the SPV effect. Due to instrumental

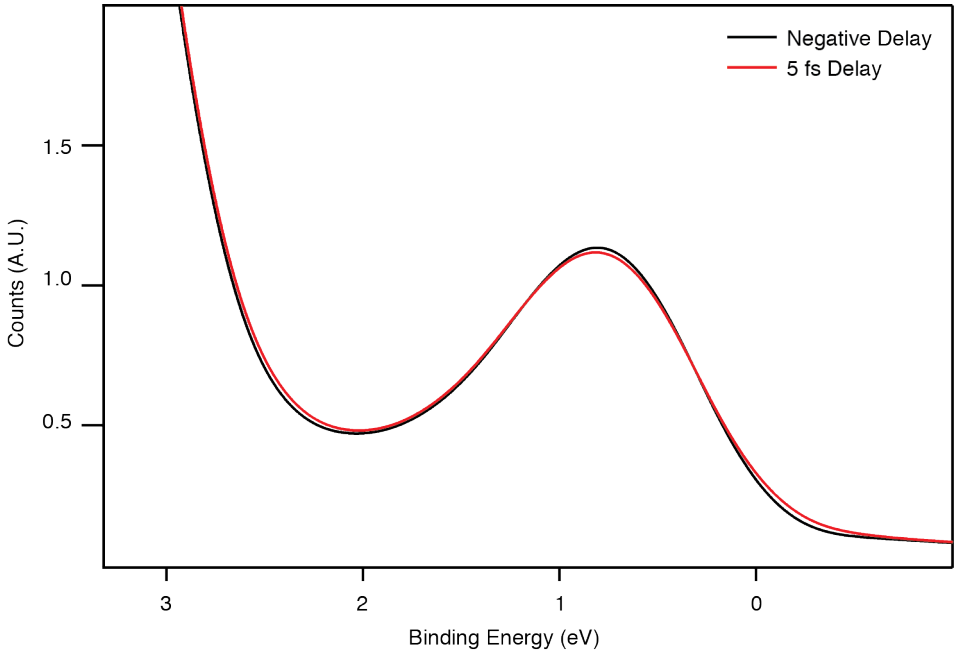

Figure 6.7: Photoemission spectra measured from the reduced rutile TiO_2(110) surface using ∼30 eV XUV photons. The spectrum measured at negative delay times (black) represents the ground state electronic structure of the surface. In comparison, the spectrum measured 5 fs after irradiation (red) by a 3.54 eV UV pulse evidences depletion of the BGS (0.8 eV) and the accumulation of electrons at E_F. Additionally, a -13 meV shift of spectra is attributed to the SPV effect.

broadening, the valence band maximum extends below 3 eV, into the band gap region and so the spectra were aligned such that the difference intensity between 2.5 eV and 3 eV was roughly constant.

Difference spectra, obtained by subtracting the negative delay spectrum from spectra measured at various pump-probe delays, before and after the SPV correction, are shown in Figure 6.8a & b, respectively. Before correcting for the SPV effect, the difference spectra display a long-lived feature with positive intensity at around 3 eV, similar to that seen in Figure 6.3a. This feature is believed to arise from the SPV-induced shifting of the spectra. However, following SPV correction the feature is replaced by negative intensity at small delay times and near-negligible intensity at later delays. The negative intensity around 3 eV at short delay times is believed to arise from depletion of the valence band levels following irradiation by UV photons. Additionally, features associated with depletion of the BGS and the accumulation of electrons at E_F are evident, as expected. The SPV correction applied to each spectrum is detailed in Figure 6.4.

In order to accurately determine the dynamics of the spectra shown in Figure 6.8b, the laser pulse cross-correlation was first determined from the temporal

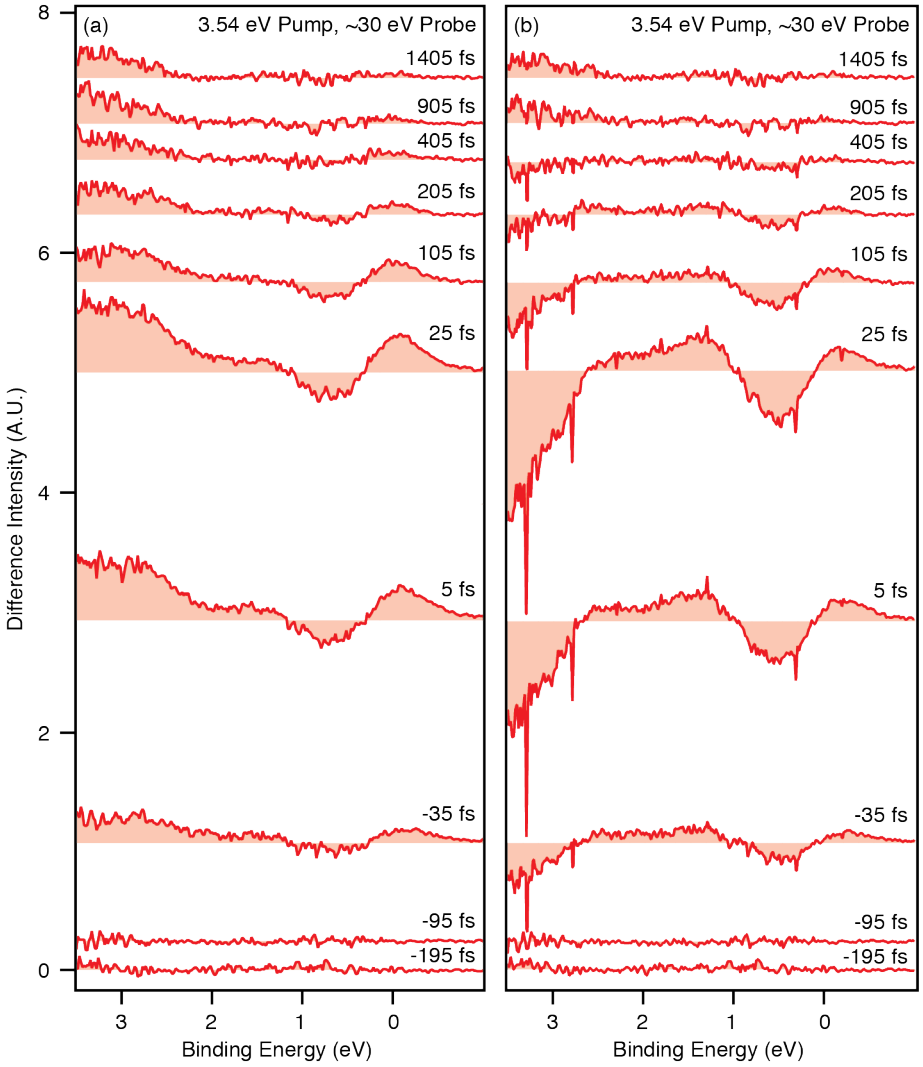

Figure 6.8: Difference spectra obtained by subtracting the negative delay spectrum in Figure 6.2 (black) from spectra measured at various delay times. (a) Difference spectra prior to correction exhibit a positive feature above about 2.5 eV, which is attributed to the SPV effect. This shift masks the depletion of the valence band region, which is expected when the surface is pumped by photon energies above the band gap. (b) Subsequent to the SPV correction, the feature at high energies is removed and the valence band depletion may been seen more clearly. However, the intensity of this signal is dependent on the SPV correction and hence the dynamics of this region could not be analysed quantitatively.

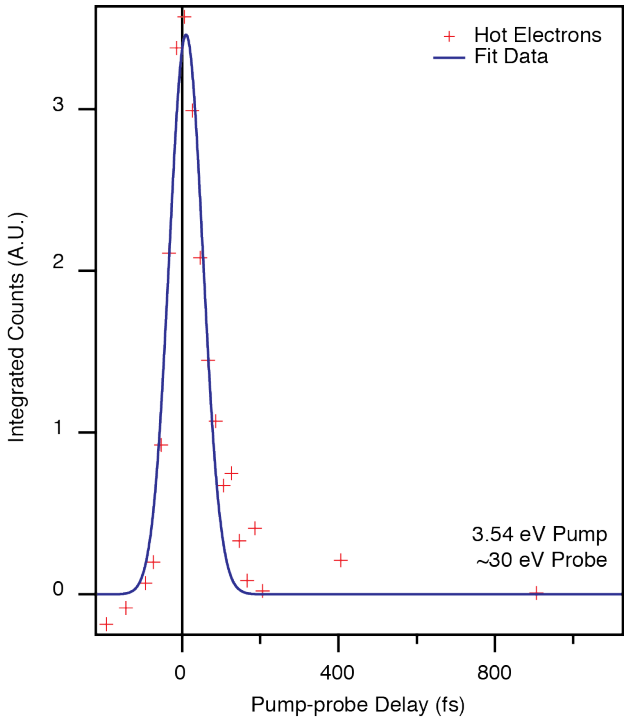

Figure 6.9: Temporal evolution of the hot electron signal, integrated from a region centred 0.6 eV above E_F, with a width of 0.4 eV. The data (red crosses) is fit by a convolution of a Gaussian and exponential decay lineshapes (dark-blue curve). A value of 10 fs was used for the exponential decay constant, which represents the lifetime of the excited states, on the basis of *ab initio* calculations [26]. A Gaussian width of (30 $\pm$ 4) fs was extracted, with an uncertainty of $\pm$9 fs in identifying the zero pump-probe delay time.

evolution of the integrated spectral intensity centred 0.6 eV above E_F. This data is shown in Figure 6.9. The electron energy loss time for these conduction band levels is predicted to be about 10 fs by *ab initio* calculations [26]. Using this value for the exponential decay constant gave a width of (30 $\pm$ 4) fs for the Gaussian representing the cross-correlation of the UV and XUV pulses. The uncertainty in identifying the zero pump-probe delay time was $\pm$9 fs. These parameters were then used to analyse the dynamics of other spectral regions. Since it was not possible to simultaneously monitor the population of all states accessible by UV excitation from the valence band and band gap states, the principal of charge conservation may not be applied to this analysis. Instead, the temporal evolution of the various spectral regions will be treated separately. The difference signal at the valence band maximum (around 3 eV) was found to be highly sensitive to the SPV correction procedure, due to the high gradient of this spectral region, and therefore its dynamics could not be quantitatively determined within the uncertainty of this experiment.

Figure 6.10 presents the temporal evolution of the BGS and E_F regions, centred at 0.8 eV and 0 eV, respectively. The width of the integration window was 0.4 eV. The signal representing depletion of the BGS is over twice as intense as the accumulation signal at E_F at 0 fs pump-probe delay. This is unexpected, as the intensity of electrons at E_F results from photoexcitation from the valence band and the relaxation of electrons photoexcited from the BGS to states in the conduction band with higher energies. In contrast, the BGS depletion signal arises solely from photoexcitation to the conduction band. Since the density of states of the valence band is much greater than that of the BGS, the accumulation signal is expected to be the more intense. That the opposite trend is observed in Figure 6.10 suggests that the difference signal here too is influenced by the SPV correction procedure. However, since the BGS and E_F regions are less intense than the valence band minimum the dynamics of these energy regions may still be determined.

The time-resolved spectra in Figure 6.10 display an intense peak at small delay times, similar to that seen in Figure 6.6, in addition to a non-negligible component which persists to longer delays. Subsequently, an additional exponential decay component is added to the fitting procedure described in Section 6.3.1. A major difference between the IR- and UV-pumped experiments is the creation of electron-hole pairs via inter-band photoexcitation. A recent transient IR absorption study of nanostructured TiO_2 films has demonstrated electron-hole lifetimes of the order of 10 ps [30] and recombination times ranging from a few picoseconds

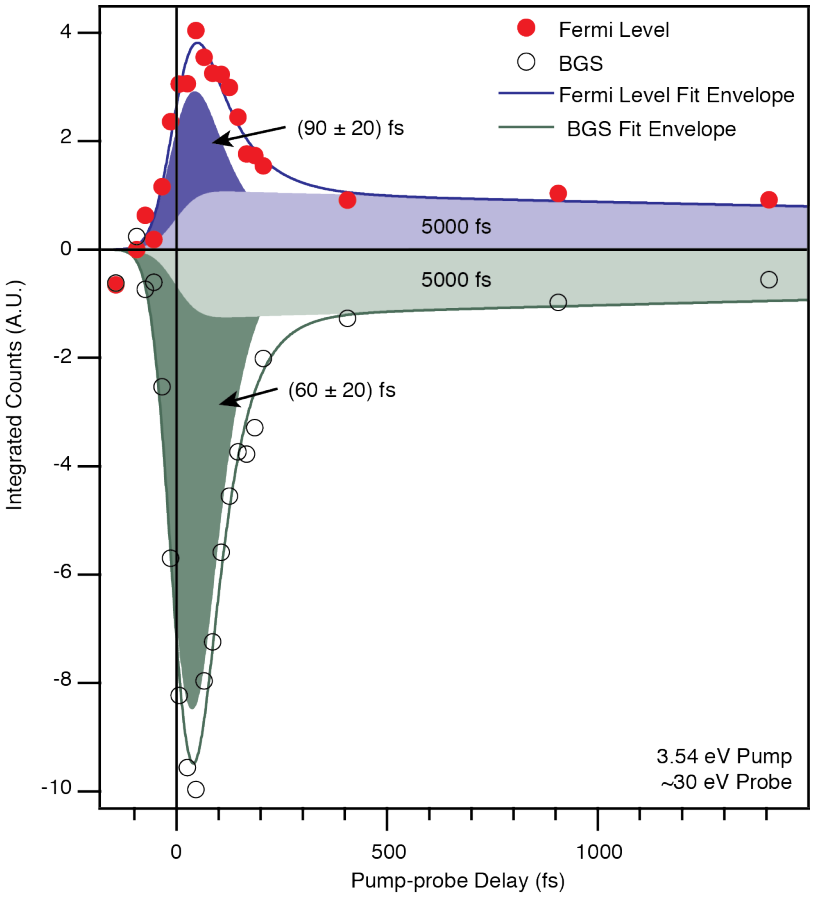

Figure 6.10: Temporal evolution of the BGS (black rings) and E_F (red circles) regions. Both spectra display an intense peak at small delay times, in addition to a longer-lived component. This slow decay component is attributed to electron-hole recombination and assigned a lifetime of 5 ps in order to best fit both spectra. The values of (60 $\pm$ 20) fs and (90 $\pm$ 20) fs obtained for the fast decay components of the BGS and E_F dynamics, respectively, are similar to the electron trapping time extracted in Section 6.3.1.

to nanoseconds have been observed in other studies [26, 31].

The lifetime of the new, slow decay component was varied between 0.5 ps and 10 ps to assess its influence on the fitting results obtained for the faster decay component. It was observed that altering this parameter had only a small effect on the value obtained for the fast decay component, as between 0.5 ps and 10 ps the lineshapes are almost constant with time, compared to the fast decay component, and hence the fitting procedure is in fact more sensitive to the initial amplitude. A lifetime of 5 ps was chosen for the slow decay component to best fit both the BGS and E_F spectra. Entering this parameter along with the zero delay and laser cross-correlation times determined from the temporal evolution of the hot electrons $\sim$0.6 eV above E_F into the fitting of the faster decay component gave values of (60 $\pm$ 20) fs and (90 $\pm$ 20) fs for the BGS and E_F regions, respectively. The errors quoted for these parameters arise primarily from the uncertainty associated with fitting two exponential decay components, in addition to uncertainty in the fixed fitting parameters.

The times obtained for the fast decay component of the UV-pumped spectra are similar to those extracted from the IR pumped measurements. In particular, the dynamics of the BGS region in these two experiments are within error of each other. In the UV-pumped experiment, spectral intensity at E_F arises both from electrons excited directly from the valence to the conduction band and from the relaxation of BGS electrons following photoexcitation to higher energy conduction band levels. The lifetime of the conduction band state accessible from the BGS via resonant photoexcitation using $\sim$3.5 eV photons is too fast to be resolved by $<$20 fs pulses [32], though an upper limit of 14 fs was obtained in Chapter 4 from the hydroxylated surface. Relaxation of electrons in the conduction band continuum is expected to occur rapidly, on a timescale of a few tens of femtoseconds [26, 33, 34], due to strong electron-phonon coupling in TiO_2 [2]. Hence, the longer decay time at E_F obtained in the UV-pumped measurements likely contains an additional contribution from this relaxation process.

We now address the origin of the slow decay component in Figure 6.10. As shown in Section 6.3.1, electron trapping and repopulation of the BGS occurs on a $\sim$40 fs timescale following IR irradiation. However, depletion of the BGS clearly persists to much longer times in Figure 6.10. The recombination of electrons within 0.01 eV of the conduction band minimum with valence holes is believed to occur on a picosecond timescale [26, 33] and has been shown to persist into the nanosecond regime in some studies [31]. Electron-hole recombination on

this timescale may explain the long-lived accumulation signal at E_F. However, recovery of the BGS depletion was shown to be much faster in the IR-pumped experiment and the correlation between the population of these two regions at late times may not be expected.

A possible origin of the coupling between the electron-hole recombination and the depletion of the BGS at late delay times is trap-assisted recombination [24]. In trap-assisted recombination processes, an electron (hole) in the conduction (valence) band recombines with a hole (electron) trapped at states in the material's bandgap. The involvement of trap states in recombination processes in semiconductors is well established [35] and single-carrier trapping has been invoked to explain photoluminescence spectra of TiO_2 [36, 37]. In an n-type semiconductor such as reduced TiO_2, the trap states referred to in this work as BGS are filled by excess electrons. Recombination of photogenerated holes with BGS electrons explains the depletion of this feature at longer pump-probe delays and correlates this quantity with the density of electron-hole pairs. This dependency explains the similar dynamics obtained for the BGS and E_F in this work.

6.4 Summary & Conclusion

This chapter presents energy- and time-resolved photoemission studies of the reduced rutile TiO_2(110) surface following irradiation with IR or UV photons. In the IR-pumped experiment, a time of $\sim$40 fs is obtained for the trapping of electrons at the conduction band minimum as small polarons. The coincidence of this trapping time with the period of the LO phonon mode supports the interpretation that interaction of electrons with this phonon mode dominates polaron formation at ambient temperatures. This finding is important for a complete understanding of the dynamics of excited charge carriers at the rutile TiO_2(110) surface, which has implications for the application of this material to catalysis. In addition, the results of this experiment may serve as a useful comparison to other metal oxides, such as strontium titanate ($SrTiO_3$) [38] and reduced anatase TiO_2 [3], in which polaron formation also occurs.

In addition to the $\sim$40 fs trapping time obtained from the IR experiment, UV excitation of the rutile TiO_2(110) surface revealed a much slower decay component, which was assigned to electron-hole recombination. Measurements of

electron-hole recombination in TiO_2, which range from picosecond to nanosecond timescales, support this assignment [26, 31, 33]. The delayed recovery of the BGS intensity was attributed to a trap-assisted recombination process, in which a valence band hole recombines with an electron trapped in the BGS. Indeed, electron-hole recombination times have been shown to depend on the defect concentration, suggesting the involvement of BGS electrons [30]. The trap-assisted recombination phenomenon explains the correlation between the population of electrons at the conduction band minimum and the depletion of the BGS at delay times longer than $\sim$300 fs. These findings provide insight into the influence of trapped electrons on the population of excited electrons and holes at the surface, which is important in photocatalytic processes.

Further work on this topic may include similar measurements at anatase TiO_2 or $SrTiO_3$ surfaces. Since phonons and excess electrons interact less in these materials than that at the rutile TiO_2(110) surface, large polarons are believed to form [3, 38]. The decreased polaron localisation at these surfaces may be expected to influence the dynamics of electron trapping. Additionally, highly localised, small polarons have been observed at the reduced anatase TiO_2(101) surface [3], which may reveal fundamental differences between the behaviour of small and large polarons in the same material. Since the period of the LO phonon mode in anatase is similar to that of rutile TiO_2 [39], similar trapping times may be expected for small polaron formation. Finally, time-resolved studies of charge transfer from dye molecules to rutile TiO_2 may be undertaken in order to better understand the dynamics of dye-sensitised solar cells.

References

[1] I. Austin and N. Mott, "Polarons in crystalline and non-crystalline materials," *Advances in Physics*, vol. 18, no. 71, pp. 41–102, 1969.

[2] E. Hendry, F. Wang, J. Shan, T. F. Heinz, and M. Bonn, "Electron transport in TiO_2 probed by THz time-domain spectroscopy," *Physical Review B*, vol. 69, no. 8, p. 081101, 2004.

[3] M. Setvin, C. Franchini, X. Hao, M. Schmid, A. Janotti, M. Kaltak, C. G. Van de Walle, G. Kresse, and U. Diebold, "Direct View at Excess Electrons in TiO_2 Rutile and Anatase," *Physical Review Letters*, vol. 113, no. 8, p. 086402, 2014.

[4] M. A. Henderson, "A surface science perspective on TiO_2 photocatalysis," *Surface Science Reports*, vol. 66, no. 6-7, pp. 185–297, 2011.

[5] D. C. Cronemeyer, "Infrared Absorption of Reduced Rutile TiO_2 Single Crystals," *Physical Review*, vol. 113, no. 5, pp. 1222–1226, 1959.

[6] J. Tang, W. Wang, G.-L. Zhao, and Q. Li, "Colossal positive Seebeck coefficient and low thermal conductivity in reduced TiO_2," *Journal of Physics: Condensed Matter*, vol. 21, no. 20, p. 205703, 2009.

[7] E. Yagi, R. R. Hasiguti, and M. Aono, "Electronic conduction above 4 K of slightly reduced oxygen-deficient rutile TiO_{2-x}," *Physical Review B*, vol. 54, no. 11, pp. 7945–7956, 1996.

[8] L. Kavan, M. Grätzel, S. E. Gilbert, C. Klemenz, and H. J. Scheel, "Electrochemical and Photoelectrochemical Investigation of Single-Crystal Anatase," *Journal of the American Chemical Society*, vol. 118, no. 28, pp. 6716–6723, 1996.

[9] V. N. Bogomolov, Y. A. Firsov, E. K. Kudinov, and D. N. Mirlin, "On the Experimental Observation of Small Polarons in Rutile (TiO_2)," *physica status solidi (b)*, vol. 35, no. 2, pp. 555–558, 1969.

[10] N. A. Deskins and M. Dupuis, "Electron transport via polaron hopping in bulk TiO_2: A density functional theory characterization," *Physical Review B*, vol. 75, no. 19, p. 195212, 2007.

[11] D. C. Cronemeyer, "Electrical and Optical Properties of Rutile Single Crystals," *Physical Review*, vol. 87, no. 5, pp. 876–886, 1952.

[12] V. M. Khomenko, K. Langer, H. Rager, and A. Fett, "Electronic absorption by Ti^{3+} ions and electron delocalization in synthetic blue rutile," *Physics and Chemistry of Minerals*, vol. 25, no. 5, pp. 338–346, 1998.

[13] S. Eriksen and R. Egdell, "Electronic excitations at oxygen deficient TiO_2(110) surfaces: A study by EELS," *Surface Science*, vol. 180, no. 1, pp. 263–278, 1987.

[14] M. A. Henderson, W. S. Epling, C. H. F. Peden, and C. L. Perkins, "Insights into Photoexcited Electron Scavenging Processes on TiO_2 Obtained from Studies of the Reaction of O_2 with OH Groups Adsorbed at Electronic Defects on TiO_2(110)," *The Journal of Physical Chemistry B*, vol. 107, no. 2, pp. 534–545, 2003.

[15] U. Diebold, "The surface science of titanium dioxide," *Surface Science Reports*, vol. 48, no. 5-8, pp. 53–229, 2003.

[16] G. Mattioli, P. Alippi, F. Filippone, R. Caminiti, and A. Amore Bonapasta, "Deep versus Shallow Behavior of Intrinsic Defects in Rutile and Anatase TiO_2 Polymorphs," *The Journal of Physical Chemistry C*, vol. 114, no. 49, pp. 21694–21704, 2010.

[17] A. Janotti, C. Franchini, J. B. Varley, G. Kresse, and C. G. Van de Walle, "Dual behavior of excess electrons in rutile TiO_2," *physica status solidi (RRL) - Rapid Research Letters*, vol. 7, no. 3, pp. 199–203, 2013.

[18] V. E. Henrich, G. Dresselhaus, and H. J. Zeiger, "Observation of Two-Dimensional Phases Associated with Defect States on the Surface of TiO_2," *Physical Review Letters*, vol. 36, no. 22, pp. 1335–1339, 1976.

[19] M. A. Henderson, "An HREELS and TPD study of water on TiO_2(110): the extent of molecular versus dissociative adsorption," *Surface Science*, vol. 355, no. 1-3, pp. 151–166, 1996.

[20] L. Kronik and Y. Shapira, “Surface photovoltage phenomena: theory, experiment, and applications,” *Surface Science Reports*, vol. 37, no. 1-5, pp. 1–206, 1999.

[21] S. Neppl and O. Gessner, “Time-resolved X-ray photoelectron spectroscopy techniques for the study of interfacial charge dynamics,” *Journal of Electron Spectroscopy and Related Phenomena*, vol. 200, pp. 64–77, 2015.

[22] K. Ozawa, M. Emori, S. Yamamoto, R. Yukawa, S. Yamamoto, R. Hobara, K. Fujikawa, H. Sakama, and I. Matsuda, “Electron-Hole Recombination Time at TiO_2 Single-Crystal Surfaces: Influence of Surface Band Bending,” *The Journal of Physical Chemistry Letters*, vol. 5, no. 11, pp. 1953–1957, 2014.

[23] J. Liqiang, S. Xiaojun, S. Jing, and C. Weimin, “Review of surface photovoltage spectra of nano-sized semiconductor and its applications in heterogeneous photocatalysis,” *Solar Energy Materials*, vol. 79, no. 2, pp. 133–151, 2003.

[24] Z. Zhang and J. T. Yates Jr., “Band bending in semiconductors: chemical and physical consequences at surfaces and interfaces,” *Chemical Reviews*, vol. 112, p. 5520, 2012.

[25] K. Ozawa, S. Yamamoto, R. Yukawa, R. Liu, M. Emori, K. Inoue, T. Higuchi, H. Sakama, K. Mase, and I. Matsuda, “What determines the lifetime of photoexcited carriers on TiO_2 surfaces?,” *The Journal of Physical Chemistry C - in press*, 2016.

[26] V. P. Zhukov and E. V. Chulkov, “Ab initio approach to the excited electron dynamics in rutile and anatase TiO_2,” *Journal of Physics: Condensed Matter*, vol. 22, no. 43, p. 435802, 2010.

[27] S. Schoche, T. Hofmann, R. Korlacki, T. E. Tiwald, and M. Schubert, “Infrared dielectric anisotropy and phonon modes of rutile TiO_2,” *Journal of Applied Physics*, vol. 113, no. 16, p. 164102, 2013.

[28] D. Eagles, “Polar modes of lattice vibration and polaron coupling constants in rutile (TiO_2),” *Journal of Physics and Chemistry of Solids*, vol. 25, no. 11, pp. 1243–1251, 1964.

[29] J. G. Traylor, H. G. Smith, R. M. Nicklow, and M. K. Wilkinson, “Lattice Dynamics of Rutile,” *Physical Review B*, vol. 3, no. 10, pp. 3457–3472, 1971.

[30] M. Sachs, E. Pastor, A. Kafizas, and J. R. Durrant, "Evaluation of Surface State Mediated Charge Recombination in Anatase and Rutile TiO_2," *The Journal of Physical Chemistry Letters*, vol. 7, no. 19, pp. 3742–3746, 2016.

[31] Y. Yamada and Y. Kanemitsu, "Determination of electron and hole lifetimes of rutile and anatase TiO_2 single crystals," *Applied Physics Letters*, vol. 101, no. 13, p. 133907, 2012.

[32] A. Argondizzo, X. Cui, C. Wang, H. Sun, H. Shang, J. Zhao, and H. Petek, "Ultrafast multiphoton pump-probe photoemission excitation pathways in rutile TiO_2(110)," *Physical Review B*, vol. 91, no. 15, p. 155429, 2015.

[33] A. Kazempour, "Quasiparticle lifetimes in rutile and anatase TiO_2: GW approximation," *Physica Scripta*, vol. 90, no. 2, p. 025804, 2015.

[34] E. M. Bothschafter, A. Paarmann, E. S. Zijlstra, N. Karpowicz, M. E. Garcia, R. Kienberger, and R. Ernstorfer, "Ultrafast Evolution of the Excited-State Potential Energy Surface of TiO_2 Single Crystals Induced by Carrier Cooling," *Physical Review Letters*, vol. 110, no. 6, p. 067402, 2013.

[35] P. T. Landsberg, C. Rhys-Roberts, and P. Lal, "Auger recombination and impact ionization involving traps in semiconductors," *Proceedings of the Physical Society*, vol. 84, no. 6, pp. 915–931, 1964.

[36] Y. Yamada and Y. Kanemitsu, "Blue photoluminescence of highly photoexcited rutile TiO_2: Nearly degenerate conduction-band effects," *Physical Review B*, vol. 82, no. 11, p. 113103, 2010.

[37] Y. Yamada and Y. Kanemitsu, "Photoluminescence spectrum and dynamics in highly photoexcited rutile TiO_2," *physica status solidi (c)*, vol. 8, no. 1, pp. 104–107, 2011.

[38] J. L. M. van Mechelen, D. van der Marel, C. Grimaldi, A. B. Kuzmenko, N. P. Armitage, N. Reyren, H. Hagemann, and I. I. Mazin, "Electron-Phonon Interaction and Charge Carrier Mass Enhancement in $SrTiO_3$," *Physical Review Letters*, vol. 100, no. 22, p. 226403, 2008.

[39] R. J. Gonzalez, R. Zallen, and H. Berger, "Infrared reflectivity and lattice fundamentals in anatase TiO_2," *Physical Review B*, vol. 55, no. 11, pp. 7014–7017, 1997.

Chapter 7

Conclusions & Future Work

In this thesis, photoemission studies of reduced titanium dioxide (TiO_2) surfaces are presented that investigate the influence of intrinsic defects and adsorbates on the ground and excited state electronic structure of this semiconductor. The insights gained into the chemistry and physics of TiO_2 may confer benefits to the many industrial applications of this material, in addition to providing insight into the phenomena governing the properties of less-commonly studied metal oxides.

Two-photon photoemission (2PPE) spectroscopy of the reduced rutile TiO_2(110) surface revealed a resonant photoexcitation process between Ti 3d states in the material's band gap and conduction band levels $\sim$2.7 eV above the Fermi level (E_F). Though present at surfaces containing only bridging oxygen vacancies (O_b-vacs), the intensity of the resonant signal is greatly increased by the dissociative adsorption of water, which results in a hydroxylated surface. Since photocatalytic surfaces are known to be extensively hydroxylated, these findings suggest the presence of a photoexcitation pathway in addition to band gap excitation.

The influence of water coverage on the Ti 3d resonance was characterised via temperature-dependent 2PPE and ultra-violet photoemission spectroscopy (UPS). UPS spectra confirmed the presence of molecular water at the surface and was also employed to monitor the intensity of the band gap states (BGS) signal. A maximum was observed in the 2PPE signal under a monolayer coverage of water, in which coverage regime the BGS signal was constant. This finding suggests that the observed enhancement of the resonance originates from modifications in the unoccupied density of states. Hence, the enhancement was attributed to partial dissociation of the water monolayer, which increases the coverage of hy-

droxyls (OH_b) and in turn increases the 2PPE signal. Since water is present in the majority of industrial environments in which TiO_2 is employed, this work informs the fundamental understanding of the water-metal oxide interface.

The excess electrons arising from the creation of reducing defects, such as O_b-vacs and OH_b, are known to localise as polarons at the rutile TiO_2(110) surface and influence many properties of this material. Here, pump-probe experiments were conducted to interrogate the dynamics of this trapping process at a well-defined, single crystal surface. Under infra-red (IR) irradiation, an electron trapping time of about 40 fs was obtained from the temporal evolution of the BGS and E_F spectral regions. The timescale of the trapping process is similar to the period of the longitudinal optical phonon mode, which is believed to dominate polaron formation in TiO_2 at room temperature. These measurements provide insight into the fundamental dynamics of polaron formation in TiO_2 and other transition metal oxides.

An additional spectral component was identified following ultra-violet (UV) irradiation, which was assigned to electron-hole recombination since the dynamics of this feature matches the picosecond timescales observed in transient absorption spectra. The unexpectedly slow recovery of the BGS population was attributed to trap-assisted recombination of electrons and hole. Hence, the dynamics of conduction band electrons and the BGS depletion are linked via this process. This study illuminates the ultra-fast dynamics of excited electrons and holes in TiO_2 and provides insight into the ways in which their populations are influenced by trapped electrons. This knowledge may be relevant to some catalytic processes, in which charge transfer to adsorbed molecules must proceed within the electron-hole recombination time.

The chemistry and physics of the stoichiometrically identical, anatase polymorph of TiO_2 differs significantly from that of the more commonly studied rutile phase. In part, these differences arise due to the propensity for highly reactive O_b-vacs to migrate to the sub-surface or bulk region at temperatures above 200 K. Consequently, the availability of excess electrons, which are believed to facilitate redox reactions at the surface, is also thermally dependent due to their strict localisation at O_b-vacs. UPS spectra confirmed predominantly associative adsorption of water at the anatase TiO_2(101) surface, which is attributed to the scarcity of surface O_b-vacs. However, the possibility of a mixed water-hydroxyl monolayer remains.

Electron bombardment was shown to increase the reduction state of the anatase

TiO_2(101) surface, evidenced by a 50% increase of the BGS peak in UPS, through the creation of O_b-vacs. However, these defects typically migrate to the subsurface region at room temperature, restoring the initial surface defect concentration. This observation, in addition to modifications in the valence band spectral region, led to the suggestion that dissociative adsorption of water in the gas phase at irradiation-induced surface O_b-vacs results in a hydroxylated surface. The ability to fix excess charge at the surface above the thermally-equlibriated level is potentially beneficial for the efficiency of redox reactions at the surface.

Further research in this area may include investigation into the Ti 3d resonance observed in 2PPE measurements of the rutile TiO_2(110) surface. Continuously varying the polarisation angle of the laser may provide details regarding direct and indirect excitation mechanisms at the surface, as has been achieved for metal surfaces. Additionally, changes in the intensity of the Ti 3d resonance have been monitored via 2PPE to indirectly study the photodissociation of alcohols, which leads to a greater coverage of hydroxyls. This method may be applied to studies of other molecules for which OH_b is a dissociation product. It may also be of interest to monitor the dissociation rate as a function of the sample's reduction state, in addition to the photon energy and flux.

Further pump-probe measurements could follow the injection of charge from adsorbed dye molecules, for example, photosensitisers containing the N3 ruthenium complex, providing insight into the dynamics of the charge transfer process. Similar studies may also be conducted at anatase TiO_2 surfaces, where the differing degree of excess electron localisation may influence the dynamics of polaron formation. Additionally, the next generation of free-electron lasers may provide sufficient flux to permit time-resolved studies of valence band and core levels dynamics at femtosecond timescales, extending the scope of these investigations. Finally, the focus of this work could be extended to include other semiconductor surfaces, such as strontium titanate or ceria.